

**An EGSnrc investigation of correction factors
for ion chamber dosimetry**

by

Lesley A. Buckley

A thesis submitted to the
Faculty of Graduate Studies and Research
in partial fulfillment of the requirements
for the degree of

Doctor of Philosophy

Department of Physics
Carleton University
Ottawa-Carleton Institute of Physics
Ottawa, Canada
September 20, 2005

Copyright © 2005 Lesley A. Buckley

The undersigned recommend to
the Faculty of Graduate Studies and Research
acceptance of the thesis

“An EGSnrc investigation of correction factors
for ion chamber dosimetry”

submitted by Lesley A. Buckley
in partial fulfillment of the requirements
for the degree of Doctor of Philosophy

Chair, Department of Physics

Thesis Supervisor

Carleton University

September 20, 2005

Abstract

Radiation dosimetry is used to quantify the dose delivered during radiation therapy by using ionization chambers with several correction factors. Knowledge of these factors is needed at well below the 1% level in order to maintain the overall uncertainty on the reference dosimetry near 1-2%. The small magnitude of the corrections renders measurements very difficult. Monte Carlo calculations are widely used for this purpose, however they require very low statistical uncertainties.

A new user-code, CSnrc, for the EGSnrc Monte Carlo system is described. CSnrc uses a correlated sampling variance reduction technique to reduce the uncertainty for dose ratio calculations. Compared to an existing EGSnrc user-code from which it was developed, CSnrc shows gains in efficiency of up to a factor of 64 and achieves much lower statistical uncertainties on correction factors than previously published.

CSnrc is used to compute the central electrode correction factor, P_{cel} , in a broader range of beams than previously used and at the depths relevant to modern protocols. For photon beams, the CSnrc values compare well with the values used in dosimetry protocols whereas for electron beams, CSnrc shows up to a 0.2% correction for a graphite electrode, a correction currently ignored by dosimetry protocols. The difference from currently used values is slightly less for an aluminum electrode.

CSnrc is also used to compute the wall correction factor, P_{wall} . For cylindrical chambers in photon beams, the CSnrc calculations are compared to the currently used Almond-Svensson formalism and differ from this formalism by as much as 0.8%. The CSnrc values are used to explain some previously published experiments showing problems with P_{wall} . For electron beams, where dosimetry protocols assume a P_{wall}

of unity, CSnrc calculations show a correction as large as 0.6%.

For parallel-plate chambers, there is little information available regarding P_{wall} in photon beams. CSnrc shows corrections of over 2% for some chambers. In electron beams, P_{wall} has been assumed to be unity, despite previously published evidence suggesting otherwise. CSnrc shows that for some chambers at lower energies, P_{wall} is nearly 1.02.

Acknowledgements

It is with mixed feelings that I near the end of my Ph.D. research. I have formed many friendships over the years and have been blessed to be able to work with so many wonderful people. You have all in some way contributed to this thesis and I am grateful for your part in this work.

First and foremost, I would like to thank my supervisor, Dave Rogers, for his kindness, his patience and for giving me an opportunity to work with him on this project. It has been a great pleasure to learn from someone whom I admire and respect as much as I do Dave.

I would also like to thank all of my colleagues and friends at the National Research Council of Canada for making my time spent there so enjoyable. I cannot think of a better place to work and you will all be missed. I will continue to treasure the friendships developed there and will not soon forget the many characters that made up such a wonderful group. In particular, I would like to thank Malcolm McEwen for his friendship, his car rides on the snowy days and for his very insightful and much appreciated advice regarding my work. I would also like to thank Iwan Kawrakow with whom I feel grateful to have had a chance to work and both Blake Walters and Ernesto Mainegra-Hing for their patience and help over the years.

I have also had the good fortune to work closely with several people at Carleton University, and would like to thank my colleagues and friends there for their help and valuable discussions.

I am also indebted to my former colleagues at the University of Wisconsin. Though my work there was not directly related to this thesis, my time spent there formed a broad base of my knowledge in Medical Physics and encouraged me to pursue

a Ph.D. in this field. In particular, I would like to thank my former supervisor, Larry DeWerd for his unwavering and continued support.

Finally, I would like to thank my family, without whom this thesis would never have been possible. To my husband Sean, thank you for your patience and understanding while this was in progress. I could not have done this without you. To my mom, you have always supported me in all of my decisions and for that I am forever grateful. Thank you for always taking an interest and helping me through these many years while I was a student. You drove me to my first day of school and have been there for me ever since. This is for you.

This work has been supported in part by the Natural Sciences and Engineering Research Council of Canada and by the Government of Ontario.

Statement of Originality

This thesis describes the author's research during the course of the Ph.D. program at Carleton University. This work was conducted at both Carleton University and at the National Research Council of Canada. Many of the results herein have been presented as abstracts at national and international conferences and the main results of this thesis have been summarized in a set of four papers published in, or submitted to, the journal *Medical Physics*, which is the official journal of both the Canadian Organisation of Medical Physicists (COMP) and of the American Association of Physicists in Medicine (AAPM). The following list details the four papers and describes where the results are found within this thesis, as well as the author's contributions to each paper:

- L. A. Buckley and I. Kawrakow and D. W. O. Rogers. An EGSnrc investigation of cavity theory for ion chambers measuring air kerma. *Medical Physics* (30), 2003, 1211-1218.
 - Parts of this paper are used in Chapter 4 when discussing the systematic uncertainty in the calculations. Specifically, the sections dealing with the electron cross-sections are taken from this paper. The discussion of the α parameter in Chapter 6 is also taken from this paper.
 - The author performed all of the calculations for this paper and drafted and performed edits on the manuscript. An abstract detailing some of the results was presented at the 2002 AAPM annual meeting in Montreal.

- L. A. Buckley and I. Kawrakow and D. W. O. Rogers. CSnrc: Correlated sampling Monte Carlo calculations using EGSnrc. *Medical Physics* (31), 2004, 3425-3435.
 - The results of this paper appear in Chapter 3 discussing the correlated sampling code and in parts of Chapter 5 describing the central electrode correction factor.
 - The author developed the correlated sampling user-code for the EGSnrc Monte Carlo system and performed all of the calculations, drafted and edited this paper. An abstract detailing the results from this paper was presented at the 2004 COMP annual meeting in Winnipeg.

- L. A. Buckley and D. W. O. Rogers. Wall correction factors, P_{wall} , for thimble ionization chambers. Submitted to *Medical Physics*, July 2005.

- The results of this paper constitute the majority of Chapter 6.
- The author performed all of the calculations and drafted and made edits to the manuscript. The results from this paper were presented in two abstracts: at the 2005 COMP annual meeting in Hamilton and at the 2005 AAPM annual meeting in Seattle.

• L. A. Buckley and D. W. O. Rogers. Wall correction factors, P_{wall} , for parallel-plate ionization chambers. Submitted to Medical Physics, September 2005.

- The results from this paper are presented in Chapter 7 of this thesis.
- The author performed all of the calculations and drafted and made edits to the manuscript. The results from this paper were presented in two abstracts: at the 2005 COMP annual meeting in Hamilton and at the 2005 AAPM annual meeting in Seattle.

Contents

1	Introduction	1
1.1	General introduction	1
1.2	An overview of dosimetry protocols	5
1.3	The EGSnrc Monte Carlo system	7
1.3.1	Introduction to EGSnrc	7
1.3.2	User-codes	9
1.3.3	Energy cutoffs and material data sets	10
1.3.4	Random number generators	11
1.3.5	Variance reduction techniques	11
1.3.6	Parallel computing	12
1.3.7	Input spectra	13
1.3.8	Input geometries	16
1.4	Outline of the thesis	16
2	TG-51 Formalism	20

2.1	Absorbed dose to water calibration coefficient	20
2.2	Cavity theory	22
2.2.1	P_{stem}	24
2.2.2	P_{cel}	24
2.2.3	P_{wall}	25
2.2.4	P_{repl}	26
2.3	Beam quality specifiers	28
2.3.1	Photon beam quality specifiers	28
2.3.2	Electron beam quality specifiers	29
2.4	k_Q values	30
2.4.1	Photon beams	30
2.4.2	Electron beams	30
2.5	Relation between $N_{D,w}$ and N_K	31
2.6	Summary	32
3	Correlated sampling method	34
3.1	Background	34
3.2	Statistics	36
3.2.1	History by history statistics	36
3.2.2	Ratios of correlated quantities	37
3.3	CSnrc implementation in EGSnrc	39

3.3.1	Correlated sampling algorithm	39
3.3.2	Considerations in the user-code	42
3.4	Benchmarking CSnrc	45
3.4.1	Comparison to CAVRZnrc	45
3.4.2	Verification of statistical uncertainties	49
3.4.3	Efficiency gains	53
3.4.4	Comparison to EGS4	57
4	Systematic uncertainties	61
4.1	Photon cross sections	62
4.1.1	Variations in photon cross-sections	62
4.1.2	Variation between databases	65
4.2	Electron cross-sections	68
4.2.1	Mean excitation energy	69
4.2.2	Electron density effect	72
4.2.3	Cutoff energy, Δ	73
4.3	Summary	77
5	P_{cel} in high-energy photon and electron beams	78
5.1	P_{cel} in photon beams	81
5.1.1	Effect of electrode size	83

5.2	P_{cel} in electron beams	85
5.2.1	Effect of electrode size	88
6	P_{wall} for cylindrical ion chambers: the Almond-Svensson formalism	90
6.1	P_{wall} and K_{comp} values in photon beams	92
6.1.1	Corrections for build-up caps in ^{60}Co beams	92
6.1.2	Discrepancies in k_Q values for cylindrical chambers	93
6.1.3	Comparison of different waterproofing sleeves	97
6.2	P_{wall} values in photon beams	100
6.2.1	P_{wall} for several commonly used ion chambers	100
6.2.2	Comparison to Almond-Svensson formalism	104
6.3	P_{wall} values in electron beams	111
6.4	Summary	118
7	P_{wall} for parallel-plate ion chambers	120
7.1	Evidence for a non-unity wall correction	121
7.2	P_{wall} values in electron beams	124
7.2.1	P_{wall} for several commonly used ion chambers	124
7.2.2	P_{wall} as a function of depth of measurement	128
7.2.3	Comparison to perturbation correction calculations	131
7.3	P_{wall} values in photon beams	134

7.4	Summary	136
8	The replacement correction, P_{repl}	138
9	Conclusions	142

List of Tables

1.1	Description of selected EGSnrc user-codes.	10
1.2	Details of the input photon spectra	14
1.3	Details of the input electron spectra	15
1.4	Details of the thimble chamber geometries	17
1.5	Details of the parallel-plate chamber geometries	18
3.1	Summary of the correlated sampling macros.	44
3.2	Description of the test geometries used to benchmark the CSnrc code.	48
4.1	Effect of the mean excitation energy of graphite on calculated ratios of chamber response	70
4.2	Effect of the low energy cutoff energy on calculations of the restricted stopping power ratios	74
5.1	Central electrode correction factor for an NE2571 chamber in photon beams.	82

6.1	Comparison of K_{comp} formalism to measured and CSnrc-calculated results.	94
6.2	Ratios of k_Q values comparing CSnrc calculations to experiment and to the TG-51 formalism.	96

List of Figures

2.1	Schematic of correction factors for Spencer-Attix cavity theory applied to an ionization chamber.	24
3.1	Schematic of the correlated sampling algorithm.	40
3.2	Flowchart showing the correlated sampling implementation in EGSnrc.	46
3.3	Comparison between dose ratios calculated using CSnrc and CAVRZnrc.	50
3.4	χ^2 per degree of freedom for dose ratio uncertainties.	52
3.5	The gain in efficiency due to photon splitting as a function of the splitting number	55
3.6	Efficiency gain from correlated sampling as a function of the correlation coefficient.	58
3.7	Effect of central electrode on cavity dose for an NE2561 chamber in high-energy electron beams.	60
4.1	Effect of uncertainties in the photon cross-sections on P_{wall}	64

4.2	Effect of uncertainties in the photon cross-sections on the dose to the cavity	65
4.3	Effect of radiative cross-section database on ratios of mass energy absorption coefficients	67
4.4	Effect of the mean excitation energy on ion chamber response	71
4.5	Comparison of EGSnrc-calculated restricted stopping-power ratios to values used in TG-51	76
5.1	Schematic showing the three geometries used in the P_{cel} calculations	80
5.2	P_{cel} as a function of beam quality in high-energy photon beams	84
5.3	P_{cel} as a function of electrode diameter in photon beams.	86
5.4	P_{cel} as a function of beam quality in high-energy electron beams	88
5.5	P_{cel} as a function of electrode diameter in a 6 MeV beam	89
6.1	Schematic showing the geometries used to calculate P_{wall}	91
6.2	Effect of a PMMA waterproofing sleeve on chamber response	98
6.3	Effect of a nylon waterproofing sleeve on chamber response	99
6.4	P_{wall} as a function of beam quality in high-energy photon beams for commonly used chambers.	101
6.5	The sleeve effect for thimble chambers in high-energy photon beams.	103
6.6	The effect of cavity size on P_{wall} in high-energy photon beams	105
6.7	P_{wall} for an NE2571 chamber compared to the Almond-Svensson formalism	106

6.8	Ratios of P_{wall} values calculated using CSnrc to those from the Almond-Svensson formalism	107
6.9	α values used in the Almond-Svensson formalism	109
6.10	P_{wall} values with and without waterproofing sleeve for the NE2571 chamber in electron beams	112
6.11	Linear fits to calculated P_{wall} values for cylindrical chambers in high-energy electron beams	113
6.12	The sleeve effect for thimble chambers in high-energy electron beams	114
6.13	P_{wall} as a function of depth of measurement for an NE2571 chamber in electron beams	116
6.14	P_{wall} as a function of wall material density	118
7.1	P_{wall} for an NACP chamber in high-energy electron beams	126
7.2	P_{wall} as a function of R_{50} for parallel-plate chambers in high-energy electron beams	127
7.3	P_{wall} as a function of depth for an NACP chamber in electron beams	129
7.4	Comparison of standard cavity theory to cavity theory with P_{wall} correction	130
7.5	Overall perturbation correction for an NACP chamber in electron beams	133
7.6	P_{wall} values for the NACP and Markus chambers in photon beams . .	135
7.7	P_{wall} values for parallel-plate chambers in photon beams	136

8.1	P_{repl} for the NACP chamber inferred from the corrected Spencer-Attix cavity theory	140
-----	--	-----

Chapter 1

Introduction

1.1 General introduction

Radiation dosimetry is an integral part of the radiation therapy process. The ultimate goal of radiation dosimetry is to determine the dose delivered to the tumour and to the normal tissues in a patient undergoing radiotherapy. There are several steps involved in radiation dosimetry: beginning with measurements performed at a national standards laboratory followed by reference dosimetry performed at a radiation therapy clinic and treatment planning to predict the dose to the patient and finally, an estimation of the dose delivered to the tumour.

A standards laboratory maintains a primary standard of absorbed dose to water, normally using either water or graphite calorimetry or Fricke dosimetry.¹⁻⁵ Calorimetry involves direct measurement of the energy deposited per unit volume, or dose, by the radiation output from the machine. Calorimetry is difficult to perform precisely and is therefore, under normal circumstances, impractical to use in a clinic,

or even on a daily basis within a standards laboratory.

The instrument most commonly used for radiation dosimetry measurements is the ionization chamber. This instrument contains a small air-filled cavity, bounded by walls made from a low atomic number material in order to most closely mimick the properties of water or tissue. The ion chamber contains two electrodes across which a voltage is applied. When the chamber is placed in a radiation field, air molecules are ionized by the radiation and the ions are collected by the collecting electrode within the chamber. The chamber is connected to an electrometer in order to measure the ionization that has occurred within the air cavity. The ionization that is collected is measured in coulombs (C).

At the national standards laboratories, calorimetry is used in order to allow a calibration to convert from the ionization current measured by the ion chamber to an absorbed dose, in units of gray (Gy). The measured energy per unit mass by the calorimeter ($1 \text{ J/kg} = 1 \text{ Gy}$) is compared to the measured ionization current in the chamber for the same radiation field. This is used to determine the calibration coefficient, in absorbed dose per unit charge, for the ionization chamber. Such a chamber is then used as a reference standard against which clinical ion chambers are calibrated. The standards laboratory provides a calibration coefficient, in units of Gy/C (or Gy/reading), for each chamber sent for calibration by a radiotherapy clinic. The calibrated ion chamber is then used by the clinic when quantifying the output from the clinical therapy machines.

Within a radiotherapy clinic, reference dosimetry consists of two steps. The first is to measure the output from the therapy machine using a calibrated ionization chamber. This consists of determining the absorbed dose per monitor unit output from the machine. Typically this is measured in Gy/MU, where MU is the number of

monitor units recorded by a monitor chamber while the beam is turned on. This step in the reference dosimetry is performed under a specific set of reference conditions described by a dosimetry protocol.⁶⁻⁹ The absorbed dose to water delivered by the machine must be quantified for every clinical beam. The second step in clinical dosimetry is to assess the dose delivered to a patient. This is based upon the machine calibration, the patient data and the treatment plan specifications.

The success of any radiation treatment depends on the accuracy of the dose delivery. This is affected by every step of the treatment delivery process, including the reference dosimetry, the treatment planning, the patient setup and the beam delivery itself. Although there are no clear recommendations on what level of accuracy is required, the goal of radiotherapy is to achieve an accuracy of $\pm 5\%$ in the dose delivered to the tumour.¹⁰ This value is based upon the effects of uncertainty in the dose delivery on the treatment outcome: in terms of both tumour control probability and normal tissue complications. While different tumours sites respond differently to radiation, for all tumours it is essential not to miss targeted regions while sparing the surrounding normal tissues, some of which may be critically impacted by high doses of radiation. Some studies suggest the need for even stricter demands on the accuracy of the dose delivery,¹¹ however the value of $\pm 5\%$ remains the nominal goal of clinical radiation therapy.^{9,10}

The largest contribution to the overall uncertainty in the dose delivery comes from uncertainties in the patient setup, including day-to-day variability in the patient position, machine output, organ motion and changes in the tumour size or surrounding normal tissue. While the day-to-day variability can be well monitored using external markers for positioning, controlling the effects of organ motion and changes in the tumour shape require sophisticated treatment delivery methods. Recent trends in

research have been directed towards real-time imaging during the treatment delivery which allows the treatment to reflect changes in the tumour position during the course of a treatment fraction. Recent research also allows for the possibility of adaptive radiotherapy which adjusts to the changes in the tumour geometry from fraction to fraction. Despite advances in the area of adaptive radiotherapy and real-time imaging, uncertainty in the patient setup remains the largest contributor to the overall uncertainty in the dose delivery.

The accuracy of treatment planning step of the radiotherapy process depends largely on the optimization rules and dose calculation algorithms used in the treatment planning software. Recent planning software uses Monte Carlo simulations to calculate the dose to points of interest.¹²⁻¹⁴ This avoids some of the approximations used in dose calculation algorithms by directly simulating radiation transport within the patient geometry. However, approximate dose calculation algorithms, particularly for dealing with tissue inhomogeneities, remain a source of uncertainty in some treatment plans. The optimization of a treatment plan depends on the type of treatment delivery being used and may be based upon biological models of tumour control and normal tissue complications. These models are dependent on the availability of reliable data that apply to an in-vivo situation for the specific type of tumour being considered.

The goal of limiting the overall uncertainty in the dose delivered to less than 5% requires that the uncertainty from the clinical reference dosimetry be small compared to the uncertainties from the other steps in the treatment delivery. The reference dosimetry is more easily controlled than the patient setup and biological parameters, therefore it is reasonable to try to minimize the uncertainty from this step as much as possible. A goal of 1-2% uncertainty in the reference dosimetry is normally

sought, although an uncertainty closer to 1% is preferable. Uncertainties in the clinical reference dosimetry arise primarily from the parameters within the dosimetry protocols themselves. Ionization chamber measurements can be made to a precision of much better than 0.5%, therefore with careful setup, this should not contribute significantly to the overall uncertainty. The underlying theory of the dosimetry protocols, along with the associated approximations and corrections, are the main source of uncertainty in the reference dosimetry. Satisfying a goal of 1-2% uncertainty in the reference dosimetry therefore requires that the individual parameters used in the protocol be well-determined at levels significantly below the 1% uncertainty level.

1.2 An overview of dosimetry protocols

The development of a protocol for clinical reference dosimetry is overseen by national organizations for medical physicists. Many countries adopt the protocol developed by the International Atomic Energy Agency (IAEA) or a similar protocol designed to simplify the implementation of reference dosimetry for a clinical physicist. In North America, the dosimetry protocols are developed by the American Association of Physicists in Medicine (AAPM). Currently, the IAEA uses report TRS-398⁹ and both the Canadian Organisation of Medical Physicists (COMP) and the AAPM use Task Group report TG-51⁷ for absorbed dose determination in high-energy photon and electron beams.

Current dosimetry protocols have evolved significantly from and vastly improve upon previous generations of protocols. The first series of protocols used by the AAPM were very simple in their application.^{15,16} A calibration laboratory provided an exposure calibration coefficient in a ⁶⁰Co beam and the user had to look up a

conversion factor for other nominal photon or electron energies. No consideration was given to the type of chamber used or a more rigorous determination of the beam quality. These simplifications led to errors in the beam calibration of up to 5%.⁷

More recent protocols improve upon the earlier versions but are significantly more complex in their implementation. Both the AAPM's TG-21⁶ and the IAEA's TRS-277⁸ are based upon standards of air kerma. In these formalisms, an air-kerma calibration is used to determine a cavity-gas calibration coefficient for the chamber, in units of dose per unit ionization. The conversion from air kerma to dose to the medium involves a number of correction factors. The physical quantities involved, and the many steps required in these air-kerma-based protocols are such that there is considerable uncertainty associated with the beam calibration. As a result, these protocols yield a higher uncertainty for the clinical reference dosimetry than desired.

Current dosimetry protocols (see for example ref.^{7,9}) are based upon absorbed dose to water standards which have an uncertainty of about 0.5% in ⁶⁰Co beams.^{17,18} Absorbed dose to water standards are much more robust than air-kerma standards and offer several improvements over the reference dosimetry based upon air-kerma standards.

One such improvement achieved by absorbed dose to water standards over the air-kerma based systems is the more robust primary standards that are achievable. Standards for absorbed dose to water in photon beams may be obtained by a number of methods. A common approach is to use water calorimetry to determine the absorbed dose to water directly for a given beam.^{17,19,20} It is also common to use a graphite calorimeter to determine the absorbed dose to graphite and then infer the absorbed dose to water for the same beam.² Another approach is to measure the total absorption in a Fricke solution of an electron beam of known energy. The

1.2. AN OVERVIEW OF DOSIMETRY PROTOCOLS

absorbed dose to water is then determined by using the Fricke solution in a small vial at a point in a water phantom, assuming that the calibration of the Fricke solution is independent of beam quality.^{21,22} It is also possible to calibrate the Fricke solution directly in the beam quality of interest.

Comparison of the absorbed dose standards in different national laboratories show agreement between the various methods to within 1%.^{23,24} Since each of these methods has different types of systematic uncertainties, the system of absorbed dose to water standards avoids systematic errors that can affect all of the standards. In contrast, almost all of the primary standards for air-kerma use the same technique and therefore comparisons cannot reveal uncertainties in the technique itself. A further advantage of absorbed dose standards over air kerma standards is that the absorbed dose measurements are not restricted to ^{60}Co beams and can be determined directly in accelerator beams and for radiation types other than x-rays.

Clinically, the advantage of absorbed dose to water protocols is that they are easier to implement, thereby reducing the potential for errors. Furthermore, the calibration coefficients are in terms of absorbed dose, the quantity of interest in clinical reference dosimetry, and therefore these protocols are conceptually simpler to understand.

1.3 The EGSnrc Monte Carlo system

1.3.1 Introduction to EGSnrc

Monte Carlo calculations are an integral part of many current studies in radiotherapy. Particularly in radiation dosimetry, where experiments are very difficult to perform

with an adequate degree of precision, and where many of the correction factors cannot be measured directly via experiments, many of the quantities of interest are determined using Monte Carlo simulations.

The EGSnrc Monte Carlo code (Electron-Gamma Shower)^{25,26} is a package of codes used for the simulation of electron and photon transport through an arbitrary geometry. It is the most recent in the family of EGS Monte Carlo codes and is improved substantially from its predecessor, the EGS4 version.²⁷ Among other changes, EGSnrc uses an improved multiple-scattering theory which includes relativistic spin effects in the cross section, a more accurate boundary crossing algorithm and improved sampling algorithms for a variety of energy and angular distributions. For a more detailed description of the features of the EGSnrc system, the reader is referred to the EGSnrc manual.²⁶ The newest version of EGSnrc is a multi-platform version of the EGSnrc code, keeping the physics of EGSnrc intact.²⁸

In general, Monte Carlo simulation of particle transport requires a great deal of information regarding the interaction properties of the particle and the media through which it travels. A particle history is begun by creating the particle with position and energy coordinates according to a specified source distribution. The particle travels a certain distance before undergoing an interaction; determined by the probability of interaction dictated by the total interaction cross-section. The type of interaction and the resulting particles are determined by the interaction cross-sections at that point. Any secondary particles created must also be transported and a particle history ends when all particles have either deposited their energy within the medium or have left the geometry.

Transport of electrons presents some difficulties since an electron may undergo hundreds of thousands of interactions as it slows down in a medium. The computa-

tion time required for event-by-event transport of this slowing down process would be impractical. This problem is dealt with in EGSnrc by using the condensed history technique described by Berger.²⁹ In this method, a large number of individual interactions are condensed into a single step. The overall effect of this step is sampled from the relevant multiple scattering distributions. The condensed history technique is a reasonable approximation, since in most cases a single interaction causes little change in the energy and direction of an electron. For greater detail, the reader is referred to the work by Kawrakow and Bielajew.³⁰

In addition to the EGSnrc code system, there are other Monte Carlo systems based upon the condensed history technique.³¹⁻³⁵ However in many instances, the EGSnrc code is a more efficient code for the types of calculations being considered here. Furthermore, EGSnrc is the only code shown to perform particle transport to within 0.1% accuracy with respect to analytical solutions to transport situations.^{36,37} However, as with all Monte Carlo codes, the overall accuracy is limited by the accuracy of the underlying cross-sections, as will be discussed in Chapter 4.

1.3.2 User-codes

The EGSnrc system includes a group of user-codes³⁸ developed for specific types of calculations. One such user-code, CAVRZnrc is used to calculate the dose to a cavity within a cylindrically symmetric (RZ) geometry. It is used primarily for ion chamber calculations, however it can be adapted to any situation where the desired quantity is the dose to a certain region or regions. Table 1.1 describes the EGSnrc user-codes previously developed and used in the present study. The EGSnrc system is structured such that the user may develop their own user-codes to interface with the particle

transport system, as will be described in a subsequent chapter.

Table 1.1: Description of the EGSnrc user-codes used in the present study.³⁸ This list only includes those codes not developed as part of the current work.

User-code	Description
CAVRZnrc	Used to compute the total dose to a region (or regions) designated as the cavity in a cylindrically symmetric geometry and to calculate some correction factors.
SPRRZnrc	Computes the stopping power ratio between the medium specified in the input file and air for each region within the geometry.
DOSRZnrc	Computes the dose to individual regions within a cylindrically symmetric geometry. In the present study, it is used to generate depth dose information for a variety of input spectra.
FLURZnrc	Computes the fluence spectrum for designated regions within the geometry. It also outputs the mean energy of particles in a given region.
g	Computes the mass energy absorption and mass energy transfer coefficients for the medium of interest.

1.3.3 Energy cutoffs and material data sets

As with all Monte Carlo codes, in EGSnrc there are a variety of transport parameters that must be defined for each simulation. Among these are the charged particle and photon cutoff energies, *ECUT* and *PCUT*, respectively. A cutoff energy is necessary since the Monte Carlo simulation must stop transport at a finite energy. Transport of a particle ceases if the particle's energy falls below the cutoff energy. For charged particles, the cutoff energy is the total energy of the particle: kinetic plus mass energy.

Transport is also controlled by the information in the PEGS4 material data set. PEGS4 is a stand-alone program that is used to create material data files containing much of the cross-section information for the materials of interest in the calculations.²⁷

When a material data set is created using PEGS4, lower energy bounds AE and AP (for electrons and photons respectively) are defined. These parameters represent the lowest energy for which the material data are generated. Therefore, AE and AP determine the cutoff energy at which secondary particles (electrons and photons respectively) are created and below which transport will stop, irrespective of the values of $ECUT$ and $PCUT$. Among other properties, at the time of creation of a data set, PEGS4 defines the density of the material and whether or not ICRU (or any other) density effect corrections will be applied. In the present calculations, unless otherwise stated, $AE = ECUT = 521$ keV and $AP = PCUT = 10$ keV.

1.3.4 Random number generators

The generation of random numbers is integral to Monte Carlo calculations since they are used every time an interaction distribution is sampled. EGSnrc works with either of two random number generators: `RANLUX` and `RANMAR`. The details of each of these generators are described elsewhere.³⁹⁻⁴² The important properties of these random numbers for the Monte Carlo simulations described here are that they can produce the same random number sequence on different machines and that they can be initialized to guarantee independent random number sequences when doing parallel runs.

1.3.5 Variance reduction techniques

A full Monte Carlo simulation can be prohibitively time-consuming, especially when tens of millions of particle histories must be considered in order to achieve the desired precision. For this reason, most Monte Carlo codes employ variance reduction techniques in order to improve the efficiency of the calculations. A true variance re-

duction technique improves the efficiency of a calculation while providing an unbiased estimate of the quantity of interest. Monte Carlo codes also use other techniques to save computation time, such as range rejection and high cutoff energies, but these techniques only approximate the transport and are biased. The variance reduction techniques available with the EGSnrc system are described in detail in the EGSnrc users manual.²⁶ Variance reduction techniques of particular interest to the present work will be described in Chapter 3. In particular, a correlated sampling variance reduction technique, implemented in EGSnrc for this work, will be described. If implemented properly, correlated sampling is a true variance reduction technique.

1.3.6 Parallel computing

The EGSnrc system is designed such that a single simulation can be executed simultaneously on multiple computers in order to reduce the elapsed time from start to finish of the simulation. When using parallel-processing in EGSnrc, when a job is submitted to ten computers, each computer is initially assigned a small fraction of the total number of histories. As these histories are completed, the parallel-processing subroutine coordinates how many histories have been completed and how many remain. As each CPU finishes a group of histories, it will be assigned further histories to execute until the required total number has been reached. When all histories have been completed, the individual output files from the different CPUs are combined to give a final output file. The advantage of this approach is that it makes efficient use of computers having different computational power. Nearly all calculations performed in this study are performed using parallel processing on ten computers. For the correction factor calculations described in Chapters 5 through 7, a typical simulation, running on ten computers, took between 20-40 hours for photon beams and between

2-10 hours for electron beams.

1.3.7 Input spectra

CSnrc uses the standard input sources available with many of the EGSnrc user-codes. One additional source was created, modified from an existing source to allow particles to be incident onto a flat surface, as required for the rectangular geometry in CSnrc. All calculations described herein use a parallel beam with a field size of 10x10 cm², unless otherwise specified. Two beam orientations are used: along the z-axis for parallel-plate chambers, and along the y-axis for thimble chambers.

The standard EGSnrc user-codes permit different types of incident beams. The user specifies either photons, electrons or positrons and then has the option of using a monoenergetic beam, an input spectrum from a file or phase-space data generated during a complete accelerator simulation using BEAMnrc.^{43,44} The incident spectra used in the present work are taken from previously published spectra. The ⁶⁰Co spectrum is taken from the work of Mora et. al.⁴⁵ Two different sets of photon beam spectra are used,^{46,47} and range in nominal energies from 4 MV to 25 MV. All of the electron spectra used in the present work are taken from Ding and Rogers.⁴⁸ The details of the input spectra for photon and electron beams are given in Tables 1.2 and 1.3 respectively. The beam quality specifiers are taken directly from a recent work by Kalach and Rogers⁴⁹ for the photon beams and from Ding and Rogers⁴⁸ for the electron beams. The Kalach and Rogers values were computed using EGSnrc and therefore do not need to be repeated. The values of R_{50} from Ding and Rogers were computed using EGS4 and could potentially differ from EGSnrc values of R_{50} , especially at the lower energies. Using DOSRZnrc, these values are verified for selected

input spectra and for nominal beam energies below 9 MeV, the change in R_{50} is at most 0.2 mm, corresponding to a change in the reference depth, d_{ref} of no more than 0.1 mm. As will be demonstrated in Chapter 6, the correction factors show much greater sensitivity to depth at the lower electron energies, therefore a sub-0.1 mm change in d_{ref} at the low energies is not expected to affect the final results and the R_{50} values from Ding and Rogers are sufficient.

Table 1.2: Details of the input photon spectra used in the current calculations. The spectra are taken from the work of Mora et. al.,⁴⁵ Sheikh-Bagheri and Rogers⁴⁷ and Mohan et. al.⁴⁶ The nominal accelerating potential specified by the manufacturer is given by $E_{nominal}$. Also shown are the two beam quality specifiers $\%dd(10)_x$ and TPR_{10}^{20} . With the exception of the cobalt beam, all values of $\%dd(10)_x$ and TPR_{10}^{20} are taken from Kalach and Rogers.⁴⁹ The ^{60}Co values were determined using the EGSnrc system for the present work.

Description	$E_{nominal}$ (MV)	$\%dd(10)_x$	TPR_{10}^{20}
Eldorado 6 ^{60}Co ⁴⁵	-	58.3	0.571
	4 MV	62.7	0.616
	6 MV	66.5	0.658
Varian Clinac ⁴⁷	10 MV	73.8	0.728
	15 MV	77.7	0.750
	18 MV	81.3	0.774
Elekta SL25 ⁴⁷	25 MV	82.7	0.786
	4 MV	63.4	0.622
	6 MV	67.1	0.666
Varian Clinac ⁴⁶	10 MV	73.3	0.727
	15 MV	78.8	0.762
	24 MV	86.3	0.801

Table 1.3: Details of the electron beam input spectra. All spectra were taken from the work of Ding and Rogers.⁴⁸ The nominal beam energy specified by the manufacturer is given by $E_{nominal}$. Also shown are the beam quality specifier R_{50} ⁴⁸ and the reference depth, d_{ref} , for each beam.

Description	$E_{nominal}$ (MeV)	R_{50} (cm) ^a	d_{ref} (cm)
Varian Clinac	6	2.63	1.48
	9	4.00	2.30
	12	5.20	3.01
	15	6.50	3.80
	18	7.72	4.53
Therac 20	6	2.18	1.21
	9	3.42	1.95
	20	8.10	4.76
Philips SL75-20	5	2.08	1.15
Siemens KD2	21	8.30	4.88
Racetrack MM50	25	10.36	6.12

1.3.8 Input geometries

CSnrc uses the standard input subroutines common to all of the EGSnrc user-codes designed for cylindrical symmetry (RZ user-codes). These subroutines read information specified within the user's input file to generate, among other things, the simulation geometry, including dimensions and materials. For CSnrc, the input files include some additional inputs to specify the additional geometries used in the simulation. For many of the calculations discussed in subsequent chapters, specifically for the investigations of correction factors described in Chapters 5 through 7, the input geometry simulates an ionization chamber. The accuracy of an ion chamber simulation is dependent, in part, on the ability to correctly model the actual chamber geometry. The geometry details used in the current calculations are taken from the manufacturers' specifications for the ion chambers. For the simulations described in this study, the important features of the geometry include the length and diameter of the cavity, the diameter of the central electrode, where applicable, and the thickness and material of the chamber walls. Tables 1.4 and 1.5 show the details of the chamber geometries for the chambers relevant to the current study.

1.4 Outline of the thesis

Chapter 2 provides a background on the TG-51 dosimetry protocol which is the basis for much of the current work. The basic equations used in the protocol are introduced and the quantities relevant to this thesis are described in detail.

In Chapter 3, a user-code developed for the EGSnrc Monte Carlo system as part of the work for this project is described. The code uses a correlated sampling

Table 1.4: Details of the geometries for the thimble chambers studied in the present work. Chambers constructed from a non-conducting plastic such as PMMA have a graphite layer on the inside of their walls. For these chambers, both materials comprising the wall are shown, along with their thicknesses. Additional details are given for the NE2571 central electrode since these will be used in Chapter 5.

Chamber	material	Wall thickness (g/cm ²)	length (mm)	Cavity diameter (mm)	Electrode material	Waterproof
A12	C-552	0.088	25.8	6.1	C-552	Y
NE2561	graphite	0.090	9.2	7.4	Al	N
NE2571	graphite	0.061	24.0	6.4	Al ^a	N
NE2581	A-150	0.041	24.0	6.4	A-150	N
PR06C	C-552	0.053	22.0	6.4	C-552	N
PTW30001	PMMA	0.033	23.0	6.2	Al	N
	+graphite	(0.012)				
PTW30004	graphite	0.079	23.0	6.2	Al	N
IC10	C-552	0.068	6.3	6.0	C-552	Y

^a Electrode length and diameter are 20.6 mm and 1 mm respectively

Table 1.5: Details of the chamber geometries for the parallel-plate chambers used in the present calculations. The materials describe the most prominent materials used in the chamber construction. The electrode separation is 2 mm for all chambers except for the PS-033 which has a plate separation of 2.4 mm.

Chamber	Materials	Window thickness (mg/cm ²)	Electrode diameter (mm)	Guard ring width (mm)
NACP-02	Graphited rexolite electrodes and housing, graphite body, mylar foil and graphite window.	104	10	3
Roos	PMMA, graphited electrodes.	118	16	4
Markus	Graphited polyethylene foil, graphited polystyrene collector, PMMA body	0.42	5.3	0.2
PS-033	Aluminized mylar foil window, air equivalent electrode, polystyrene body	0.5	16.2	2.5

variance reduction technique and was developed in order to improve the efficiency of the ion chamber calculations performed in this study. The chapter describes the features of the code and how it is implemented in EGSnrc. The benchmarking tests are also discussed as well as the potential gains in efficiency for the applications of interest here.

Chapter 4 discusses some of the systematic uncertainties inherent to all Monte Carlo calculations. It details some of the calculations performed as part of this work in order to estimate the effect of these uncertainties on the current results.

The discussion of results as they pertain to ion chamber correction factors begins in Chapter 5 with the presentation of results for the central electrode correction factor. Chapters 6 and 7 discuss the wall correction factor for thimble chambers and parallel-plate chambers respectively. Factors influencing the values of these correc-

tion factors are investigated and where applicable, comparison of the new results to previously published values is performed.

Finally, Chapter 8 describes possible future work stemming from this study of correction factors and a summary of results and some conclusions are presented in Chapter 9.

Chapter 2

TG-51 Formalism

This chapter discusses the formalism used in the AAPM's TG-51 protocol.⁷ The basics of the formalism using an absorbed-dose calibration factor are common to all absorbed dose to water protocols, including the IAEA's TRS-398 code of practice.⁹ TG-51 and TRS-398 differ slightly in their application in the clinic, but the underlying principles are the same, with the exception of beam quality specification in photon beams. For simplicity, this chapter focusses primarily on the TG-51 protocol. Where significant differences exist between TG-51 and TRS-398, they will be described directly.

2.1 Absorbed dose to water calibration coefficient

Ionization chambers are often used for clinical dosimetry measurements. Ion chambers are widely available and are capable of making very precise measurements in the radiation fields of interest in radiotherapy. They are also easily maintained at the clinical level as they are relatively inexpensive instruments and are quite stable. There

is also a fairly well understood theory for interpreting their output.

In order to use an ion chamber to obtain absorbed dose to water, a calibration coefficient is required for the chamber. The absorbed dose calibration coefficient, $N_{D,w}^Q$, is defined by:

$$D_w^Q = MN_{D,w}^Q \quad (2.1)$$

where D_w^Q is the absorbed-dose to water, in units of gray (Gy), at the point of measurement of the ion chamber in the absence of the chamber, M is the temperature and pressure corrected electrometer reading in coulombs (C) that includes a correction for incomplete ion collection within the chamber, and $N_{D,w}^Q$ is the absorbed-dose to water calibration coefficient in units of Gy/C for the ion chamber at reference conditions in a beam of quality Q . The electrometer reading is corrected to a standard temperature and pressure of 22°C and 101 kPa respectively with a relative humidity between 20% and 80%. The coefficient $N_{D,w}$ is analogous to the air kerma calibration coefficient N_K used in earlier protocols. The relationship between $N_{D,w}$ and N_K will be discussed in Section 2.5.

Ideally, a calibration coefficient could be obtained for each beam quality of clinical interest and Eq. 2.1 could be applied directly. This is impractical since it would be very time consuming and expensive to have a chamber calibrated at every beam quality in which it is to be used. Furthermore, many standards laboratories do not have access to clinical linear accelerators and therefore cannot reproduce the beams used in the clinic. Typically, a chamber is calibrated at a standards laboratory in a ^{60}Co beam, giving a value of $N_{D,w}^{60\text{Co}}$. We may then define a factor, k_Q , by:

$$N_{D,w}^Q = k_Q N_{D,w}^{60\text{Co}}, \quad (2.2)$$

which converts the absorbed-dose calibration coefficient for a ^{60}Co beam into a cali-

2.1. ABSORBED DOSE TO WATER CALIBRATION COEFFICIENT

bration coefficient for any beam quality Q .

It is possible to measure values of k_Q for a variety of ion chambers in a number of beam qualities. However, there is no complete set of data available for all chamber types and in all beam qualities and types. It is therefore necessary to have a formalism by which k_Q can be calculated for any chamber and beam quality of interest. The TG-51 protocol provides values of k_Q for many chambers of interest in photon beams, but does not include this information for plane-parallel chambers because there is insufficient data regarding their use in photon beams. It also provides information permitting the determination of k_Q in electron beams. The values of k_Q provided in the protocol simplify the application of the protocol for the clinical user, but hide the underlying physics involved in determining k_Q . The following sections will describe the fundamentals required for the calculation of k_Q .

2.2 Cavity theory

Absorbed-dose to water dosimetry uses the Spencer-Attix cavity theory⁵⁰ to relate the absorbed dose to the gas in the ion chamber, D_{gas} , to the dose to the surrounding phantom medium, D_{med} , by the following expression:

$$D_{med} = D_{gas} \left(\frac{\bar{L}}{\rho} \right)_{gas}^{med}. \quad (2.3)$$

In this expression, $\left(\frac{\bar{L}}{\rho} \right)_{gas}^{med}$ is the ratio of the spectrum averaged restricted mass collision stopping power for the medium to that of the gas. The averaging takes place from a minimum energy, Δ , up to the maximum energy in the spectrum. The Monte Carlo calculation of the stopping power ratios will be described in Chapter 4.

Spencer-Attix cavity theory has three necessary assumptions, the first being

that the cavity does not change the electron spectrum in the medium. The second assumption is that the dose in the cavity comes from electrons that enter the cavity and not from those that are created within the cavity. The final assumption is that electrons having energy below Δ are in charged particle equilibrium. These assumptions place certain limits on the size of the cavity in order that the cavity can come close to satisfying the conditions. Furthermore, the assumptions are based upon an air cavity in a surrounding medium and do not account for physical requirements such as walls surrounding the cavity.

Real ion chambers do not satisfy the assumptions of Spencer-Attix cavity theory and therefore require corrections to Eq. 2.3:

$$D_{med} = D_{gas} \left(\frac{\bar{L}}{\rho} \right)_{gas}^{med} P_{cel} P_{stem} P_{wall} P_{repl}. \quad (2.4)$$

P_{stem} corrects for the presence of the ion chamber stem in the phantom, P_{cel} accounts for the effect of the central electrode in the cavity on the chamber response and P_{wall} corrects for the wall material being different from the phantom medium. P_{repl} accounts for changes in the electron spectrum due to the insertion of the cavity in the phantom. For chambers that are not waterproof, they require a waterproofing sleeve when used in a water phantom and there is an additional correction, P_{sleeve} , that accounts for the presence of this sleeve. Implicit in the above equation is the assumption that the correction factors are independent and therefore the order of these corrections is arbitrary. However, the order is important when doing calculations and therefore each correction must be clearly defined and must be consistent with the definitions of the other correction factors. Figure 2.1 shows a schematic representation of the correction factors as they are defined for the present work. These correction factors are applied to a real ion chamber to correct it to a small cavity satisfying the Spencer-Attix conditions described above.

2.2. CAVITY THEORY

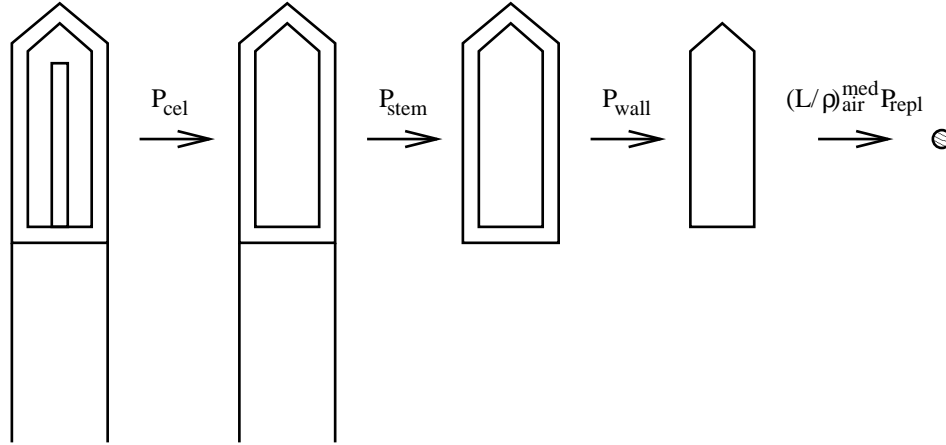


Figure 2.1: Schematic showing the correction factors necessary to apply Spencer-Attix cavity theory to a realistic ionization chamber geometry as they are defined for the current calculations. The functions of each of the correction factors are described in the text.

2.2.1 P_{stem}

The stem correction, P_{stem} , corrects for the presence of the chamber stem during the measurement. Typically, this correction is much smaller than the other chamber corrections and therefore does not contribute significantly to the overall correction. At photon energies relevant to mega-voltage radiotherapy, the stem correction is taken as less than 0.1%. The following sections deriving the beam quality conversion factor k_Q follow the conventional practice of omitting P_{stem} from the equations.

2.2.2 P_{cel}

The central electrode correction factor, P_{cel} , applies only to cylindrical chambers, which have a central electrode within the chamber cavity. P_{cel} is used to account for the change in ionization within the chamber due to the presence of the central electrode. Values are given in terms of the beam quality, the electrode material and the electrode radius. Central electrodes are commonly made of either graphite or

aluminum or of the same material as the chamber wall and have a diameter on the order of 1 mm. Values for the central electrode correction factor must be obtained using Monte Carlo simulations since the physical geometry of the chamber does not permit measurements without the electrode. A detailed examination of current values of P_{cel} for graphite and aluminum electrodes will be presented in Chapter 5.

2.2.3 P_{wall}

The wall correction factor, P_{wall} , accounts for the fact that the chamber wall is composed of a different material from the phantom medium. This difference in material causes changes in the attenuation and scatter of particles passing through the chamber wall. The correction P_{wall} applies to both cylindrical and parallel-plate chambers.

In electron beams, P_{wall} is normally assumed to be 1.00. For cylindrical chambers, this is justified partially by a theoretical model developed by Nahum⁵¹ but for all chambers is based primarily on a lack of information available regarding P_{wall} in electron beams. Values of P_{wall} for electron beams are discussed in greater detail in Chapters 6 and 7.

In photon beams, for a cylindrical ion chamber, P_{wall} is given by the Almond-Svensson formula:⁵²

$$P_{wall} = \frac{\alpha \left(\frac{\bar{L}}{\rho}\right)_{air}^{wall} \left(\frac{\overline{\mu_{en}}}{\rho}\right)_{wall}^{med} + (1 - \alpha) \left(\frac{\bar{L}}{\rho}\right)_{air}^{med}}{\left(\frac{\bar{L}}{\rho}\right)_{air}^{med}}, \quad (2.5)$$

where α is the fraction of ionization from electrons originating in the chamber wall, $1 - \alpha$ is the fraction of ionization from electrons originating in the phantom, $\left(\frac{\bar{L}}{\rho}\right)_{med2}^{med1}$ is the stopping power ratio of medium 1 to medium 2 and $\left(\frac{\overline{\mu_{en}}}{\rho}\right)_{med2}^{med1}$ is the ratio of mass-energy absorption coefficients for medium 1 to medium 2. The subscript *med*

refers to the phantom medium. In the limits $\alpha = 0$ and $\alpha = 1$, this formulation is identical to an alternative, theoretical derivation from Shiragai.^{53,54} For physical situations, the two definitions of P_{wall} give the same values, to within 0.1%.

When a waterproofing sleeve is used, the Almond-Svensson equation is extended to include the effect of the sleeve:^{55,56}

$$P_{wall} = \frac{\alpha \left(\frac{\bar{L}}{\rho}\right)_{air}^{wall} \left(\frac{\mu_{en}}{\rho}\right)_{wall}^{med} + \tau \left(\frac{\bar{L}}{\rho}\right)_{air}^{sheath} \left(\frac{\mu_{en}}{\rho}\right)_{sheath}^{med} + (1 - \alpha - \tau) \left(\frac{\bar{L}}{\rho}\right)_{air}^{med}}{\left(\frac{\bar{L}}{\rho}\right)_{air}^{med}}, \quad (2.6)$$

where τ is the fraction of ionization in the cavity due to electrons from the waterproofing sheath and $(1 - \alpha - \tau)$ is the fraction due to electrons from the phantom.

There is limited information available regarding P_{wall} for parallel-plate chambers in photon beams. Values of P_{wall} in photon beams will be discussed further in Chapters 6 and 7.

2.2.4 P_{repl}

The presence of the air cavity in the phantom medium causes changes to the electron spectrum. These changes are accounted for by the replacement correction factor, P_{repl} . The factor P_{repl} is separated into two components:

$$P_{repl} = P_{gr}P_{fl}, \quad (2.7)$$

the gradient correction, P_{gr} and the fluence correction, P_{fl} .

The gradient correction

One of the effects of the air cavity is to shift the effective point of measurement of the chamber upstream since there is less attenuation in the cavity than in the

phantom medium. For cylindrical chambers, P_{gr} depends on the dose gradient within the phantom at the location of the cavity and on the diameter of the cavity. The correction is larger for steeper gradients and for larger cavities. In the TG-51 protocol, to take the gradient effects into account when measuring depth-dose curves, it is recommended to shift the chamber upstream by $0.5r$ for electron beams and by $0.6r$ for photon beams, where r is the radius of the cavity. It should be noted that for measurements in electron beams, at a depth of d_{max} , P_{gr} is taken as unity since there is no dose gradient at this depth. For parallel-plate chambers, since the point of measurement is at the front face of the cavity, the gradient correction is already taken into account and therefore P_{gr} is taken as unity in both photon and electron beams.

The fluence correction

The fluence correction, P_{fl} , corrects for changes in the electron fluence spectrum due to the cavity, other than those associated with the gradient correction. This correction is only required in regions where full or transient charged particle equilibrium has not been established, since by the Fano theorem,⁵⁷ the electron spectrum is independent of the density of the material in regions where charged particle equilibrium exists. This is an approximation, as the Fano theorem applies for variations in density in a single medium, whereas an ion chamber has more than one material of differing density. In photon beam measurements made beyond d_{max} , it is assumed that there is no fluence correction required since at these depths, transient charged particle equilibrium exists and therefore by the Fano theorem the electron fluence is not affected by density variations within the volume of origin of the particles.⁵⁸ For an ion chamber this implies that the electron fluence within the cavity is unaffected by

the presence of the chamber within an otherwise homogenous water phantom.

In electron beams, the fluence is affected by both the in-scatter effect and the obliquity effect. The in-scatter effect increases the fluence in the cavity since electrons are not scattered out by the gas and the obliquity effect decreases the fluence because the electrons go straight ahead instead of scattering. At low energies, P_{fl} is dominated by the in-scatter effect and can be up to a 5% correction for cylindrical chambers. For this reason, at electron beam energies below 10 MeV, TG-51 recommends the use of parallel-plate chambers and requires their use for electron beam energies below 6 MeV. Well-guarded parallel-plate chambers show little fluence effect at these energies and P_{fl} is taken as unity for many of these chambers.

2.3 Beam quality specifiers

Many quantities of interest for absorbed dose to water calibrations are largely dependent on the beam quality used. Nominal beam energies are not effective beam quality specifiers since the beam quality is strongly affected by the beam flattening and other design features of a given accelerator. Furthermore, the energy of the electrons accelerated by the machine is not known very accurately.

2.3.1 Photon beam quality specifiers

The TG-51 protocol uses the percentage depth dose at 10 cm depth in the photon component of a beam, $\%dd(10)_x$, as the beam quality specifier for photon beams. This quantity is determined for a 10x10 cm² beam in the absence of electron contamination. The use of $\%dd(10)_x$ as the photon beam quality specifier was first proposed

by Kosunen and Rogers⁵⁹ as an extension to the earlier work of LaRiviere.⁶⁰ This quantity was adopted as a useful beam quality specifier since for a given value of $\%dd(10)_x$, there is little variation in the stopping power ratio for different beams.

It is worth noting that the choice of beam quality specifier for photon beams is one point of difference between TG-51 and the IAEA's TRS-398 code of practice. Instead of $\%dd(10)_x$, TRS-398 uses the tissue phantom ratio TPR_{10}^{20} . This is defined as the ratio of absorbed doses at depths of 20 and 10 cm in a water phantom, measured at a source-to-chamber distance of 100 cm and with a field size of 10x10 cm² at the plane of the chamber.

2.3.2 Electron beam quality specifiers

The currently used beam quality specifier for electron beams is R_{50} , the depth at which the dose in a broad beam is at 50% of its maximum value. Using R_{50} , Burns et. al.⁶¹ defined a reference depth for measurements in electron beams to be:

$$d_{ref} = 0.6R_{50} - 0.1 \text{ [cm]}. \quad (2.8)$$

The use of R_{50} as a beam quality specifier avoids some of the problems caused by other specifiers, such as the mean energy at the phantom surface, E_o . When calculated at d_{ref} , the stopping power ratio is well-behaved as a function of R_{50} and can be parametrized as a function of R_{50} for all clinical beams. Furthermore, measurements at d_{ref} avoid some of the problems that arise from making measurements at the depth of dose maximum, d_{max} , as was recommended by earlier protocols. The depth of dose maximum is dependent on the details of the accelerator head and may be different for two accelerators having the same R_{50} whereas the reference depth, d_{ref} as defined by Burns et. al.⁶¹ is a well-defined function of R_{50} .

2.4 k_Q values

Using the correction factors described in the preceding sections, it is now possible to present an analytical expression by which the beam quality conversion factor, k_Q , can be obtained. Combining Eqs. 2.1, 2.2 and 2.4, one arrives at an equation for k_Q :

$$k_Q = \frac{\left[\left(\frac{\bar{L}}{\rho} \right)_{air}^w P_{cel} P_{wall} P_{repl} \right]_Q}{\left[\left(\frac{\bar{L}}{\rho} \right)_{air}^w P_{cel} P_{wall} P_{repl} \right]_{^{60}\text{Co}}}. \quad (2.9)$$

The quantities in the numerator are evaluated at the beam quality of interest and the quantities in the denominator are evaluated at the reference beam quality, ^{60}Co .

2.4.1 Photon beams

In photon beams, the calculation of k_Q is a straightforward application of Eq. 2.9. The correction factors are computed as described by Rogers⁶² and the value of k_Q is dominated by the variation in the stopping power ratios.

2.4.2 Electron beams

In electron beams, the determination of k_Q is much more complex. For one thing, the quantities in the numerator and denominator are different, rather than simply being the same quantities at different beam qualities. Furthermore, the use of parallel-plate chambers introduces some changes from the thimble chamber calculations. For parallel-plate chambers, the quantities in the denominator for ^{60}Co beams, P_{cel} and P_{repl} , are unity, however P_{wall} is no longer described by the Almond-Svensson formal-

ism described above, and must be determined through Monte Carlo simulation. If a thimble chamber is used, the quantities are calculated as described in Section 2.2.3.

The quantities in the numerator also depend on the type of chamber being used. For all chambers in electron beams, P_{wall} is taken as unity and for thimble chambers, P_{cel} is given by Monte Carlo calculations. The remaining factor, P_{repl} is taken as unity for most parallel-plate chambers. For thimble chambers in electron beams, the handling of the P_{repl} correction becomes complex.

For thimble chambers, k_Q is broken into two components: $k_Q = k_{R50} P_{gr}$, where,

$$k_{R50} = \frac{\left[\left(\frac{\bar{L}}{\rho} \right)_{air}^w P_{wall} P_{fl} P_{cel} \right]_{R50}}{\left[\left(\frac{\bar{L}}{\rho} \right)_{air}^w P_{wall} P_{fl} P_{gr} P_{cel} \right]_{60Co}}, \quad (2.10)$$

and:

$$P_{gr} = \begin{cases} 1 - 0.5r_{cav}G/100 & \text{for cylindrical chambers} \\ 1 & \text{for parallel-plate chambers} \end{cases}. \quad (2.11)$$

In this expression, r_{cav} is the cavity radius in cm and G is the dose gradient at d_{ref} in units of percent change in dose per centimetre. In TG-51, P_{gr} is determined by taking the ratio of ionization measured by an ion chamber at depths of d_{ref} and $d_{ref} + 0.5r_{cav}$.

2.5 Relation between $N_{D,w}$ and N_K

In Chapter 6, current results will be compared to experimental measurements that used quantities from the air kerma based protocols. It is therefore useful to introduce here the relationship between the absorbed-dose calibration coefficient $N_{D,w}$ and the air kerma calibration coefficient N_K . The air kerma calibration coefficient is given in units of Gy/C and relates the air kerma at the position of the centre of the chamber to the meter reading. It is analagous to $N_{D,w}$ and the two quantities can be related

by the following expression, where all of the quantities in the denominator are for in-air measurements:

$$\frac{N_{D,w}}{N_K} = \frac{(1 - \bar{g}) \left(\frac{\bar{L}}{\rho}\right)_{air}^{med} P_{wall} P_{cel} P_{repl}}{\left(\frac{W}{e}\right)_{air} \left(\frac{\bar{L}}{\rho}\right)_{air}^{wall} \left(\frac{\bar{\mu}_{en}}{\rho}\right)_{wall}^{air} K_{an} K_{wall} K_{el} K_{comp}}. \quad (2.12)$$

In the above equation, \bar{g} is the fraction of an electron's energy lost via radiative processes, $\left(\frac{W}{e}\right)_{air}$ is the mean energy released in the gas per ionization, K_{an} is a correction that accounts for the $1/r^2$ decrease in the photon beam, K_{el} accounts for the effects of the central electrode and K_{wall} accounts for the attenuation and scatter in the walls of the chamber. The correction K_{comp} is used to correct for the inhomogeneous composition of the walls and is used primarily to account for the use of build-up caps that are of a different material than the chamber wall. It is analogous to the P_{wall} correction in the TG-51 formalism and is given by an equation similar to the Almond-Svensson equation for P_{wall} :

$$K_{comp} = \frac{\alpha \left(\frac{\bar{L}}{\rho}\right)_{air}^{wall} \left(\frac{\bar{\mu}_{en}}{\rho}\right)_{wall}^{air} + (1 - \alpha) \left(\frac{\bar{L}}{\rho}\right)_{air}^{cap} \left(\frac{\bar{\mu}_{en}}{\rho}\right)_{cap}^{air}}{\left(\frac{\bar{L}}{\rho}\right)_{air}^{wall} \left(\frac{\bar{\mu}_{en}}{\rho}\right)_{wall}^{air}}. \quad (2.13)$$

Here, α is the fraction of the ionization in the cavity due to electrons from the chamber wall, $(1 - \alpha)$ is the fraction due to electrons that originate in the build-up cap and the other parameters are as they are defined for Eq. 2.5. The formalism for K_{comp} will be discussed further in Chapter 6 in relation to experimental results that point to problems with this formalism.

2.6 Summary

This chapter presents an overview of the TG-51 protocol, particularly as it relates to the current study. Further detail regarding the protocol is available elsewhere.^{7,62}

The discussion of the quantities related to the protocol serves as an introduction for the reader to quantities that will be discussed and referred to in subsequent chapters. Sections 2.2.2 and 2.2.3 of the current chapter are particularly relevant, as the central electrode correction factor and the wall correction factor described therein are discussed in detail in Chapters 5 through 7.

Chapter 3

Correlated sampling method

3.1 Background

Correlated sampling is a variance reduction technique that exploits correlations between similar geometries to reduce the uncertainty on the ratio or difference of calculated quantities and reduces the total time required for the simulations. Correlated sampling may therefore be used to improve the efficiency of calculations involving correlated quantities.^{63,64} Consider, for example, a quantity that is to be calculated for two different geometries. It is straightforward to simply execute the Monte Carlo calculation twice and compare the results. If, however, the difference between the two sets of results is small, the calculations must achieve very small statistical uncertainties in order to perform a meaningful comparison. The computation time therefore becomes very large since the problem requires two separate calculations with very low statistical uncertainties. To improve upon the efficiency of this type of problem, correlated sampling uses a single execution of the Monte Carlo calculations and uses similar particle trajectories for the two geometries. This reduces the total computation time

since the entire simulation does not have to be performed twice. Furthermore, if the two geometries are similar, the two results will be correlated and they will deviate from their respective expectation values in the same direction, thereby reducing the uncertainty on the resulting difference or ratio of the two values.

A variety of correlated sampling methods have been employed for radiation dosimetry applications. Bielajew⁶⁵ employed a method whereby the initial random number seeds were stored for any history in which the primary particle, or any secondary particles, deposited dose in the cavity. This history was then repeated with the same initial seeds for each of the additional geometries. This method has the disadvantage of repeating entire histories, even when only a small fraction of the transport occurs in a region that has changed from the previous geometry. Furthermore, histories that do not result in dose deposition in the initial geometry are not repeated, but some of these histories may have deposited energy in subsequent geometries. In most cases, this has been shown to have no significant effect on the results.⁶⁴

Hedtjörn et. al.⁶⁶ applied a fixed-collision correlated sampling technique⁶⁷ to photon transport for brachytherapy applications. In this method, the correlated sampling region is treated as a perturbation to a homogeneous geometry. A set of histories is generated for the homogeneous case, and then the histories are rescored for the perturbed case, using weighting factors for the photon collisions. For realistic photon collision physics in this method, some complicated problems must be solved in order to compute the weighting factors for the heterogeneous cases, however a high degree of correlation is maintained, as the entire history is correlated between geometries.

The correlated sampling method for the EGSnrc system is based upon the

method developed for the EGS4 Monte Carlo system²⁷ by Ma and Nahum⁶⁴ for ion chamber calculations, and by Holmes et. al.⁶³ for electron beam dose calculations. In this method, histories are followed until they encounter the boundary of the region which varies between geometries, they are then split and the simulation continues independently for each geometry. Unlike the method described by Bielajew,⁶⁵ entire histories are not repeated in this approach. This correlated sampling algorithm also has the advantage of being very straightforward to implement and does not require complicated calculations of weighting factors as described above. Changes from this earlier version of the code to the EGSnrc version⁶⁸ overcome some of the disadvantages of the method used by Ma and Nahum. These changes will be described in Section 3.3.2.

3.2 Statistics

3.2.1 History by history statistics

The CSnrc code uses the history by history scoring technique described elsewhere^{69,70} and previously implemented in other EGSnrc user-codes.⁷¹ In this method, the mean dose to the cavity per unit fluence, \bar{x} , is scored by averaging the dose deposited in history i , x_i , over all N independent histories:

$$\bar{x} = \frac{1}{N} \sum_{i=1}^N x_i. \quad (3.1)$$

The uncertainty on the dose estimate, $s_{\bar{x}}$, is computed using the following:

$$s_{\bar{x}} = \sqrt{\frac{1}{N-1} \left(\frac{\sum_{i=1}^N x_i^2}{N} - \left(\frac{\sum_{i=1}^N x_i}{N} \right)^2 \right)}, \quad (3.2)$$

where x_i and N are as defined above. During the particle transport, the quantities $\sum_{i=1}^N x_i$ and $\sum_{i=1}^N x_i^2$ are scored on the fly and the cavity dose and its uncertainty are computed at the end of the simulation.

The history by history scoring technique improves upon the batch method of scoring previously used in the EGS system. The batch method had the problem that unless a large number of statistical batches was used, there was significant fluctuation in the uncertainty estimate itself. Also, the batch method of scoring required an additional dimension in the scoring arrays that is no longer needed in the history by history approach.

3.2.2 Ratios of correlated quantities

The motivation for using correlated sampling comes from the potential gain in computing efficiency. While the correlated sampling method offers some gain in computation time, the most significant improvement in efficiency comes from the reduction in the statistical uncertainty on the quantities of interest.

Monte Carlo calculations of correction factors and other dosimetric quantities of interest often require a ratio of doses to be computed. Consider a ratio of two variables, $r = y_i/x_i$. We need a statistical estimator for the ratio $r = m_1/m_2$, where the m_i are the expectations of the random variables \bar{x} and \bar{y} given in Eq. 3.1. A reasonable estimate is given by:

$$\bar{r} = \bar{y}/\bar{x}, \quad (3.3)$$

however this is usually a biased estimate. The bias, b , is a function of the covariance of \bar{x} and \bar{y} , denoted by \bar{V}_{12} , and the variance of \bar{x} :⁶⁷

$$b = 1 - \frac{\bar{V}_{12}}{m_1 m_2} - \frac{\bar{V}_1^2}{m_1^2} + O_3. \quad (3.4)$$

In this expression, \bar{V}_1 is the variance of \bar{x} and O_3 represents third order terms and higher in the variance.

It possible to have an unbiased estimate of r up to the third order moments using:⁶⁷

$$\hat{r} = \left(\frac{\bar{y}}{\bar{x}}\right) \left[1 + \frac{\bar{s}_{12}}{(\bar{x} \bar{y})} - \frac{\bar{s}_{11}}{\bar{x}^2}\right], \quad (3.5)$$

where

$$\bar{s}_{12} = \sum_{i=1}^n (x_i - \bar{x})(y_i - \bar{y})/[n(n-1)] \quad (3.6)$$

and

$$\bar{s}_{11} = \sum_{i=1}^n (x_i - \bar{x})^2/[n(n-1)]. \quad (3.7)$$

It follows from Eqs. 3.5 through 3.7 that the correction to Eq. 3.3 decreases with increasing n . For very large n , the bias in Eq. 3.3 becomes negligible. For the simulations using CSnrc, since n is always very large ($> 10,000,000$), Eq. 3.3 is used as an unbiased estimate of r , *ie.* $\hat{r} = \bar{r}$.

The variance of \hat{r} may be estimated by:

$$\hat{s}^2 = (\bar{y}/\bar{x})^2[\bar{s}_{11}/\bar{x}^2 - 2\bar{s}_{12}/(\bar{x} \bar{y}) + \bar{s}_{22}/\bar{y}^2 + \bar{t}], \quad (3.8)$$

and is unbiased up to fourth order terms.⁶⁷ The \bar{s}_{ij} and \bar{s}_{ii} are given by Eqs. 3.6 and 3.7 and \bar{t} comprises second and third order terms which are negligible for large n . In the limit of large n , the uncertainty on \hat{r} is given by the familiar expression for a ratio of correlated quantities:

$$\frac{\hat{s}_{\bar{r}}}{\bar{r}} = \sqrt{\left(\frac{s_{\bar{x}}}{\bar{x}}\right)^2 + \left(\frac{s_{\bar{y}}}{\bar{y}}\right)^2 - \frac{2\bar{V}_{xy}}{(N-1)(\bar{x} \bar{y})}}, \quad (3.9)$$

where

$$\bar{V}_{xy} = \frac{\sum_{i=1}^N x_i y_i}{N} - \frac{\sum_{i=1}^N x_i \sum_{i=1}^N y_i}{N^2}. \quad (3.10)$$

When determining efficiency gains and comparing simulations, it is often of interest to quantify the degree of correlation that exists between two variables \bar{x} and \bar{y} . The correlation coefficient is described by:

$$\rho_{xy} = \frac{\overline{V}_{xy}}{s_{\bar{x}}s_{\bar{y}}}. \quad (3.11)$$

It can be seen from Eq. 3.9, that for a greater correlation between \bar{x} and \bar{y} , the uncertainty on \hat{r} will be lower. Two quantities are said to be positively correlated if finding x above the mean increases the likelihood of finding y above the mean value. Conversely, a negative correlation implies that if x is found above the mean, the likelihood of finding y below the mean is increased. For correlated sampling as it is applied in CSnrc, the correlation between cavity doses is positive, so values of $0 \leq \rho \leq 1$ are expected.

3.3 CSnrc: Correlated sampling implementation in EGSnrc

3.3.1 Correlated sampling algorithm

The correlated sampling code developed for the EGSnrc Monte Carlo code system,^{25,26} CSnrc, is based upon an existing user-code, CAVRZnrc.³⁸ CAVRZnrc is used to compute the dose to the cavity for geometries with cylindrical symmetry. The cavity is user-defined and can occupy several geometric regions. The correlated sampling code is developed from CAVRZnrc and is therefore also used to compute the dose to the cavity. CSnrc is based upon an earlier correlated sampling code⁶⁴ developed for the EGS4 Monte Carlo system.²⁷ Although changed substantially, the EGSnrc

version of the code preserves many of the features of the earlier version.

The correlated sampling method used in EGSnrc is best illustrated by considering an example. Figure 3.1 shows a small region at some depth within a rectangular phantom for two different geometries. In a given simulation, the correlated sampling regions are defined as those regions that change material from one geometry to the next. In Fig. 3.1, if the problem of interest is to compare the dose to the small region for different materials in the region, the small region is defined as the correlated sampling (CS) region. Instead of performing the entire calculation twice, each time changing the material within the central region, CSnrc calculates the dose to the CS region for both of the cases with a single execution of the code.

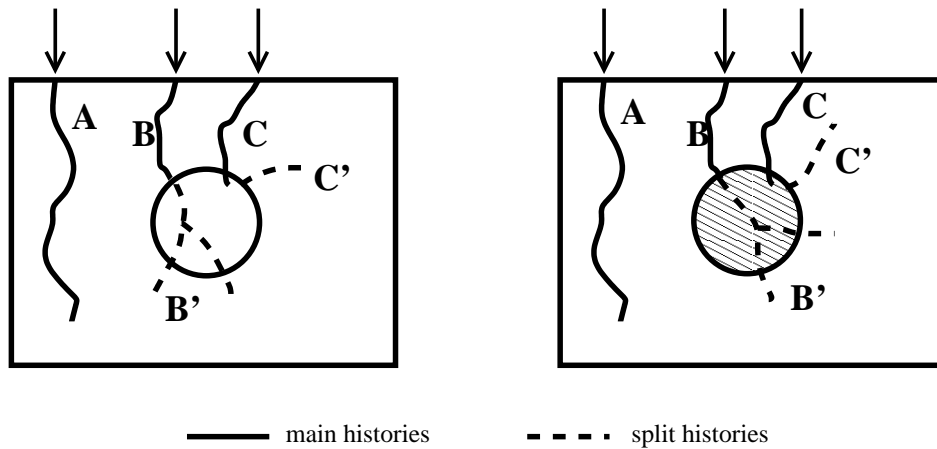


Figure 3.1: A schematic representation of the correlated sampling algorithm employed in the CSnrc code. Two distinct geometries are shown, differing in the material of the central region. The main histories are shown as solid lines and are only transported once. The split histories are transported separately for each geometry option and are represented by dashed lines.

For each history, the particle is followed as a main history until it enters the correlated sampling region, at which point it is separated into the distinct geometry options. Track A shows a particle that travels through the phantom without ever

entering the CS region. For these particles, the simulation is only performed once, potentially resulting in significant time savings. Track B is transported as a main history only until it reaches the boundary of the CS region. Following the step to the boundary, once the particle has entered the correlated sampling region, the particle data and the state of the random number generator are stored. The rest of the particle trajectory continues with any dose deposited being scored to the first geometry option. The particle and any secondary particles produced are scored to the first geometry option until the completion of their transport, regardless of whether or not they leave the CS region. When the particle and its descendants have been transported for the first geometry, the particle data are restored to the point in the main history where the split began. The particle is once again transported from that point, this time with the material in the CS region being that of the second geometry option, and the dose is scored for the second option. For more than two distinct geometries, this would continue for each geometry option, until all transport has been completed for that history and then the next history would begin as a main history.

Clearly, there will be some savings in execution time since particles that never enter the correlated sampling region are only transported once, regardless of the number of geometries being considered. Similarly, for a large phantom, the transport that takes place in the phantom, before the particle enters the correlated sampling region, is not repeated for each option. The greatest gain in computing efficiency however, comes from the reduction in the uncertainty on the ratio of scored quantities in the multiple geometries. Consider track B in Fig. 3.1: at the point where the particle enters the correlated sampling region, it has certain position and direction coordinates and a given energy. Based on these characteristics, the particle may result in energy deposition in the CS region. If the region's material is then changed, the

particle is still entering the correlated sampling region with the same parameters and will follow a similar trajectory. It is therefore very likely that it will also deposit energy in the region for the second geometry, particularly if the materials in the CS region in the two geometries have similar physical properties. The energy deposition in the CS region for the two cases is said to be positively correlated. As described in Section 3.2.2, this results in a lower uncertainty of the ratio of doses to the regions.

3.3.2 Considerations in the user-code

Within the user-code itself, the implementation of the correlated sampling algorithm requires an additional dimension for the scoring arrays used in `CAVRZnrc`. The additional dimension is used to specify the geometry for which the dose is being scored. Several flags are also introduced to distinguish between geometry options.

In existing `EGSnrc` user-codes, each particle history begins by initializing several parameters. This is followed by a call to the subroutine `SHOWER` which performs the particle transport for the initial particle and any descendants. From within `SHOWER`, the `PHOTON` and `ELECTR` subroutines are called depending on the charge of the particle. These latter two subroutines determine the type of interaction the particle will undergo and call the necessary interaction subroutines accordingly. The `PHOTON` and `ELECTR` subroutines also make calls to the scoring routine `AUSGAB`, where the temporary dose arrays are incremented each time dose is deposited in the cavity. When transport for a given particle is finished, the subroutine `SHOWER` checks whether or not there are further particles on the stack to be transported. Once the incident particle and all secondary particles produced have been transported, the simulation returns to the main routine. Further detail concerning the particle transport in `EGSnrc` is

available in the EGSnrc user manual.²⁶

In CSnrc, before the call to `SHOWER` from the main routine, a macro, `$CS-FIRST-PARTICLE`, checks if the particle is starting in a correlated sampling region. In that case, all of the particle data and the state of the random number generator are saved, before beginning transport. In such cases, the entire particle trajectory must be repeated for each geometry and the only gain in computing efficiency comes about from positive correlation between the geometries.

The implementation of correlated sampling also requires two additional macros: `$CS-TAKE-DOWN-DATA` and `$CS-END-OF-OPTION`. In the EGS4 version of the correlated sampling code, these macros were inserted into the EGS4 subroutines `PHOTON`, `ELECTR` and `SHOWER`. In addition to requiring changes to the EGS4 system itself, this method of implementation also resulted in some unnecessary repetition of segments of particle trajectories. For a particle that did not begin in a correlated sampling region, `$CS-TAKE-DOWN-DATA` stored the particle data and the state of the random number generator at the beginning of each new particle loop in `PHOTON` and `ELECTR`. For electrons, this meant that several steps often took place before the electron reached the boundary of the correlated sampling region. When the particle was restored for the next geometry option, this led to part of the trajectory being repeated within the main history. Although flags were used to ensure that no duplicate scoring occurred, this was not the most efficient algorithm with respect to computation time. The EGS4 implementation also resulted in numerous occurrences of the `$CS-TAKE-DOWN-DATA` macro, so that the particle data and random number generator information were being stored each time the new particle loop was started, and not only in the cases where the particle was entering a correlated sampling region.

To avoid unnecessary invocation of the correlated sampling macros, in CSnrc,

3.3. CSNRC IMPLEMENTATION IN EGSNRC

AUSGAB is called each time a particle steps across a region boundary. Within AUSGAB, if the particle has just entered a correlated sampling region, the `$CS-TAKE-DOWN-DATA` macro stores all relevant particle information. At this point, a loop within AUSGAB mimicks the `SHOWER` subroutine and calls `PHOTON` and `ELECTR` as necessary to complete the transport of the particle and all secondaries. Within this loop, the macro `$CS-END-OF-OPTION` checks whether or not the transport has been performed for all geometry options and controls the flags to specify the current geometry option. Table 3.1 summarizes the three principle macros used in the correlated sampling algorithm and their functions.

Table 3.1: Summary of the three principle macros inserted in the user-code for the implementation of the correlated sampling algorithm in EGSnrc.

Macro	Description
<code>\$CS-FIRST-PARTICLE</code>	Inserted in main routine before call to <code>SHOWER</code> . Takes down particle information if the particle starts in correlated sampling region.
<code>\$CS-TAKE-DOWN-DATA</code>	Located in <code>AUSGAB</code> in a block that is only reached by particles that have completed a step into a correlated sampling region. Takes down all particle information and the state of the random number generator.
<code>\$CS-END-OF-OPTION</code>	Inserted in <code>AUSGAB</code> following calls to <code>PHOTON</code> and <code>ELECTR</code> . Checks to see if one option has finished and increments flag to signal the next geometry. Exits the loop when transport for all geometry options is complete.

By calling `PHOTON` and `ELECTR` from within `AUSGAB`, the particle is forced to be treated as a “new” particle each time it crosses the boundary into a correlated sampling region. This method allows the particle data to be taken down only at the end of a step in which the particle has entered a correlated sampling region. In this way, no part of the particle trajectory is repeated outside of the correlated sampling

region, and the particle data is only stored once. Furthermore, the correlated sampling macros are located within either `AUSGAB` or the main routine of the user-code, therefore no changes to the EGSnrc system code are necessary. This implementation is possible with the new EGSnrcMP version of the Monte Carlo code,²⁸ since local variables are not allocated statically as they were in EGS4 and in previous versions of the EGSnrc code. This permits recursive invocation of the transport routines `PHOTON` and `ELECTR`. Figure 3.2 shows schematically the correlated sampling implementation in the CSnrc user-code.

3.4 Benchmarking the correlated sampling code

3.4.1 Comparison to CAVRZnrc

The first step in benchmarking the CSnrc code is to ensure that the cavity dose for a given geometry option and the ratio of cavity doses for different geometries are being computed correctly. The accuracy of the cavity doses and the ratios of cavity doses may be confirmed through comparison with doses computed using the EGSnrc user-code CAVRZnrc. CAVRZnrc is an existing user-code³⁸ and has been used extensively for ion-chamber calculations and has been shown to correctly reproduce experiments.^{37,72,73} It is also necessary to ensure that the use of correlated sampling does not preclude the use of existing variance reduction techniques available in the EGSnrc system, since the gain in efficiency provided by correlated sampling should not come at the expense of other improvements in the efficiency. To this end, CSnrc includes the photon splitting technique^{38,74} employed in CAVRZnrc. Since the transport and scoring is handled differently with and without the use of photon splitting,

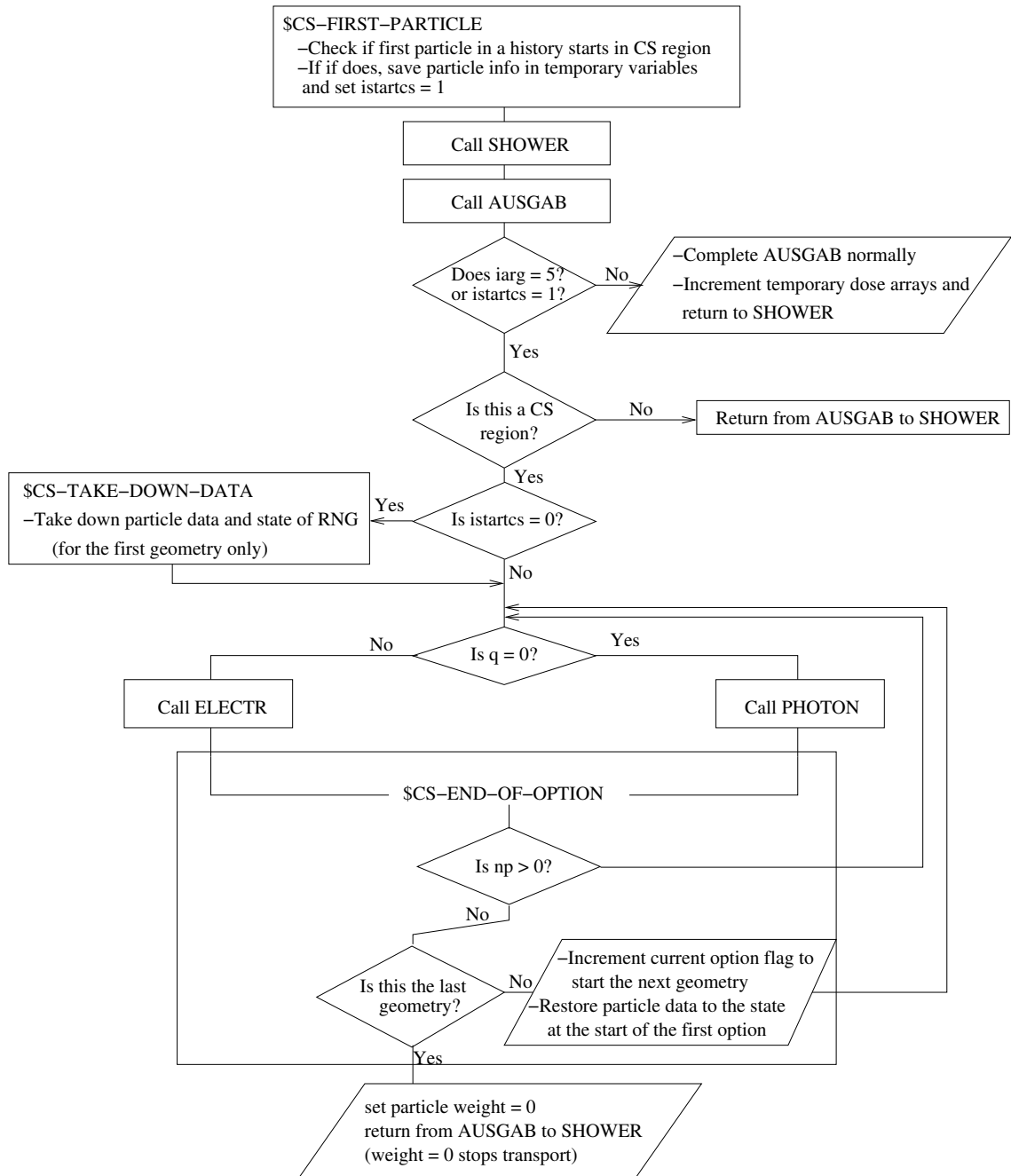


Figure 3.2: Flowchart showing the correlated sampling algorithm implemented in CSnrc. The primary subroutines involved are the **SHOWER** routine which controls particle transport and the **AUSGAB** routine which scores dose and makes recursive calls to the transport routines **ELECTR** and **PHOTON**. The placement of the three correlated sampling macros described in Table 3.1 is also shown.

the benchmarking tests must verify the accuracy of the code with and without photon splitting in use.

In the initial stages of benchmarking the CSnrc code, a series of simple test geometries was used. These consisted primarily of three cylindrical slabs stacked on top of one another with a beam incident from the top. The various geometries differed in materials, incident beam and in which slab was designated as the correlated sampling region. The use of simplistic test cases facilitated debugging during the development stages of the code.

In order to benchmark the code for realistic situations, seven test geometries were developed, ranging in complexity from relatively simple in-air ion chamber calculations, to alanine pellets in a water phantom, to a complete, in-phantom ion-chamber calculation. The test cases differed in the type of incident beam and in which region was designated as the correlated sampling region. Table 3.2 provides a brief summary of the seven realistic test cases.

The correlated sampling code was developed from the CAVRZnrc user-code and therefore, within their uncertainties, the two codes should give the same cavity doses for a given geometry. In order to compare the CSnrc results to those from CAVRZnrc, the individual cavity doses for each geometry must be accurately computed. CSnrc was executed for each of five test examples (cases A-E) and the cavity dose for each geometry option as well as the ratio of the doses for the two geometries was read from the output file. (The final two test cases, F and G, could not be compared to CAVRZnrc since it cannot handle a rectangular phantom geometry.) CAVRZnrc was then executed twice for each of the five test cases, once for each geometry option. The cavity dose output by CAVRZnrc was compared to the cavity dose from CSnrc for the corresponding geometry option. In each of the five cases, the

Table 3.2: Description of the seven test cases used to benchmark the CSnrc code. The region that changes materials is the correlated sampling region. All phantom calculations use a 10x10 cm² beam. The fractional increase in time for the additional geometry, α , and the correlation coefficient, ρ , are also shown.

Label	Description	α	ρ
A	Alanine pellets, 5 cm deep in a cylindrical water phantom, in a ⁶⁰ Co beam. Alanine is replaced by water for the 2nd geometry.	0.018	0.97
B	Thimble chamber, free in air, with an aluminum central electrode and either aluminum or graphite walls, 0.5 g/cm ² thick. A ⁶⁰ Co beam is incident from the side and the dose is scored to the air cavity.	0.98	0.19
C	Same as in B, but chamber walls are graphite and the electrode is either graphite or aluminum.	0.099	0.91
D	Same as in C, but the incident beam is a 10 MeV electron beam.	0.079	0.92
E	Thimble chamber with ⁶⁰ Co beam incident from side. A 0.05 g/cm ² wall is either graphite or aluminum and there is a graphite build-up cap to achieve full build-up.	0.69	0.26
F	Same chamber as in B, but the chamber (with no build-up cap) is placed 10 cm deep in a 30 cm cubic water phantom and the incident beam is a 10 MV photon beam. The wall material changes from graphite to water.	0.070 *	0.36
G	Cylindrical Al ₂ O ₃ pellet, 2 mm in length and having a radius of 0.564 mm. The pellet is 10 cm deep in a 30 cm cubic water phantom and the incident beam is ⁶⁰ Co.	0.0035 *	0.75

* α is calculated from CSnrc calculations with only one geometry since CAVRZnrc cannot handle this geometry.

cavity doses from the two codes agree to within 0.07%, with an average difference of 0.03%. The statistics on the cavity doses themselves range from 0.02% to 0.06%.

Since the primary use of the correlated sampling code is to compute ratios of doses for different geometries, the dose ratios computed using CSnrc were also compared to the ratios of cavity doses computed using CAVRZnrc. In this case, the dose ratio and its associated uncertainty was read directly from the CSnrc output file. In the case of CAVRZnrc, the ratio of cavity doses was computed manually from the cavity doses computed during each of the two executions of the code. In this case, the uncertainty on the dose ratio was determined as the sum of the squares of the individual dose uncertainties. The percent differences between the dose ratios from the two user-codes are shown in Fig. 3.3, with and without photon splitting as an added variance reduction technique. The comparison cannot be made for the last two test cases, F and G in Table 3.2, since CAVRZnrc does not support the use of a rectangular phantom geometry. The tests show that there is good agreement between the dose ratios calculated using CSnrc and those calculated using CAVRZnrc. Furthermore, the dose ratios show agreement both with and without photon splitting as an additional variance reduction technique. This indicates that the dose scoring and handling of transport for multiple geometries has been correctly implemented in CSnrc.

3.4.2 Verification of statistical uncertainties

In addition to verifying the agreement between CSnrc and CAVRZnrc for the dose ratios, the statistics on the dose ratios computed using CSnrc must be verified to ensure that they are being correctly determined. In order to properly compute the

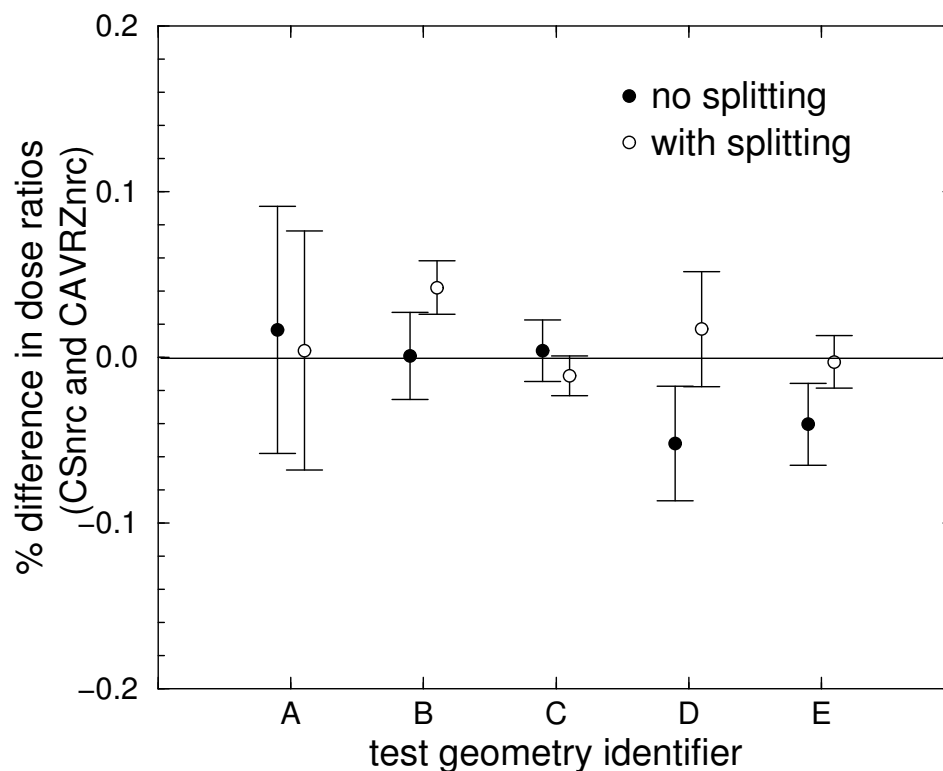


Figure 3.3: The percent difference between the dose ratios computed using CSnrc and those from CAVRZnrc. The uncertainty on the percent difference is computed using standard error propagation techniques. The results are shown for five test geometries discussed in the text and are shown with and without photon splitting as an additional variance reduction technique. The two test geometries that use a rectangular phantom are not included here as this geometry is not supported by CAVRZnrc. All calculations used $AE = 521$ keV.

uncertainty on the ratio of correlated quantities, according to Eq. 3.9 an additional scoring array must be used to sum over the product $x_i y_i$ required for the covariance calculation, shown in Eq. 3.10. The uncertainty on the dose ratio is then computed according to Eq. 3.9, where all of the other quantities required are already being scored for the uncertainty estimates on the individual cavity doses. The sum over $x_i y_i$ also permits the estimation of the correlation coefficient, (given by Eq. 3.11, page 39) at the end of the simulation.

The validity of the uncertainty estimates on the dose ratios was verified using a χ -squared statistical test. For a series of n independent simulations, the χ^2 per degree of freedom is computed using:

$$\frac{\chi^2}{df} = \frac{1}{n-1} \sum_{i=1}^n \frac{(R_i - \bar{R})^2}{s_{R_i}^2}, \quad (3.12)$$

where $R_i = \bar{x}_i / \bar{y}_i$ is the ratio computed in simulation i , s_{R_i} is the estimated uncertainty on R_i , and \bar{R} is the ratio, averaged over all n simulations, as described by Eq. 3.3:⁶⁷

$$\bar{R} = \frac{\sum_{i=1}^n \bar{x}_i}{\sum_{i=1}^n \bar{y}_i}. \quad (3.13)$$

If the uncertainty on the dose ratio is being estimated correctly, χ^2/df should be ≈ 1 . If the uncertainty has been underestimated, $\chi^2/df \gg 1$, whereas $\chi^2/df \ll 1$ indicates an overestimation of the uncertainty.

For each test case, the ratio of the doses to the cavity for two correlated geometries was computed for 20 independent runs using CSnrc. The χ^2 per degree of freedom was computed in each case and is plotted in Fig. 3.4 along with the 68% and 95% confidence limits. As expected, for all tests, $\chi^2/df \approx 1$, and the scatter of points about $\chi^2/df = 1$ shows that there is no systematic error in the calculation of the statistics on the dose ratios. The plot shows a slightly higher number of points

outside of the 68% and 95% confidence limits than expected, with 1 in 7 falling outside the 95% line and 3 in 7 falling outside the 68% line. If the five additional simple test cases are included, these fractions change to 3 in 24 and 11 in 24 respectively. All calculations were performed with a low electron energy cutoff AE of 521 keV and both with and without photon splitting. Where splitting was used, the splitting number was 130.

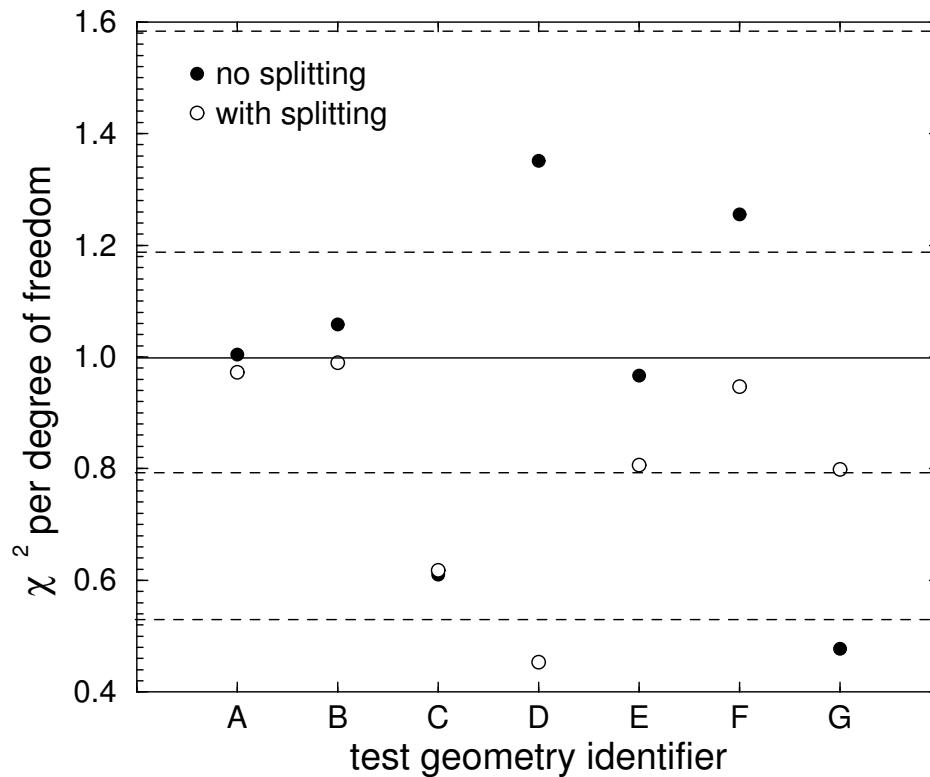


Figure 3.4: Plot showing the χ^2 per degree of freedom computed for 20 independent runs used to compute the ratio of doses for two correlated geometries in the 7 realistic test cases. The dashed lines show the 68% and 95% confidence limits for the χ^2 distribution. A $\chi^2/df \approx 1$ indicates accurate estimates of the statistics on the dose ratios. The calculations were performed with (open circles) and without (solid circles) photon splitting as an added variance reduction technique.

3.4.3 Efficiency gains

Photon splitting

It is instructive to first consider the gain in efficiency due to the use of the photon splitting technique. In photon splitting, the macro `$SELECT-PHOTON-MFP` replaces the subroutine `PHOTON` for transport. The algorithm works by splitting each photon into n_{split} photons of weight w_o/n_{split} , where n_{split} is the splitting number specified in the input file and w_o is the initial weight of the photon. The number of mean-free paths λ_i to the next interaction of the i th photon is sampled to give a uniform distribution of interaction sites. In all cases, $\lambda_{i+1} > \lambda_i$ and only transport between λ_i and λ_{i+1} is required in going from the interaction sites of photons i and $i+1$. When a split photon interacts, all resulting scattered photons are killed with a probability of $1/n_{split}$ and the original photon is re-created at the interaction site with probability $1/n_{split}$. The photon splitting algorithm is described in greater detail elsewhere.^{38,74}

The photon splitting technique employed in EGSnrc has been shown to increase the efficiency of calculations by up to a factor of 5.⁷⁴ In CAVRZnrc, the gain is less, and photon splitting improves the efficiency by up to a factor of 3.³⁸ However a systematic study of the efficiency gain due to photon splitting using EGSnrc has not been conducted. It is therefore of interest to investigate the gain from photon splitting using CSnrc for the ion-chamber calculations of interest in the study of correction factors.

The efficiency, ϵ , of a Monte Carlo calculation is inversely proportional to the total computation time T and the estimated variance s^2 of the quantity being calculated:

$$\epsilon = \frac{1}{s^2 T}. \quad (3.14)$$

The efficiency gain provided by a variance reduction technique compared to a conventional calculation is defined as the ratio of the efficiencies of the two methods.

Typically, the efficiency gain due to photon splitting is dependent on the splitting number, the geometry and the calculation parameters. Figure 3.5 shows the efficiency gain from photon splitting for three distinct situations using CSnrc. Two of the cases use CSnrc to calculate the central electrode correction factor for an NE2571 chamber at a depth of 10 cm in water for different photon energies. The calculations with an input ^{60}Co spectrum show a gain of almost a factor of 3 due to photon splitting, whereas the gain is only about half as much when using an 18 MV beam. The third case calculates the ratio of the dose to an Al_2O_3 pellet at 10 cm depth in a water phantom to the dose to water at that point in the phantom in a ^{60}Co beam. Figure 3.5 demonstrates the sharp increase in efficiency going from no splitting to the use of photon splitting in a calculation. For the cases studied here, for higher splitting numbers the efficiency gain reaches a plateau. In other cases, the gain may reach a clear maximum before decreasing with higher values of n_{split} . Since the value of n_{split} for which the gain is a maximum is very much case specific, it should be optimized for any geometry that will be used extensively.

Gain from correlated sampling

The efficiency gain achieved by the correlated sampling technique is determined relative to the efficiency of the calculation using CAVRZnrc, since this is the code from which CSnrc is developed. Since CAVRZnrc requires two independent executions in order to compute a dose ratio, the dose ratio computed in this way is for two uncorrelated cavity doses. Using the formalism of Ma and Nahum⁶⁴ (with an obvious

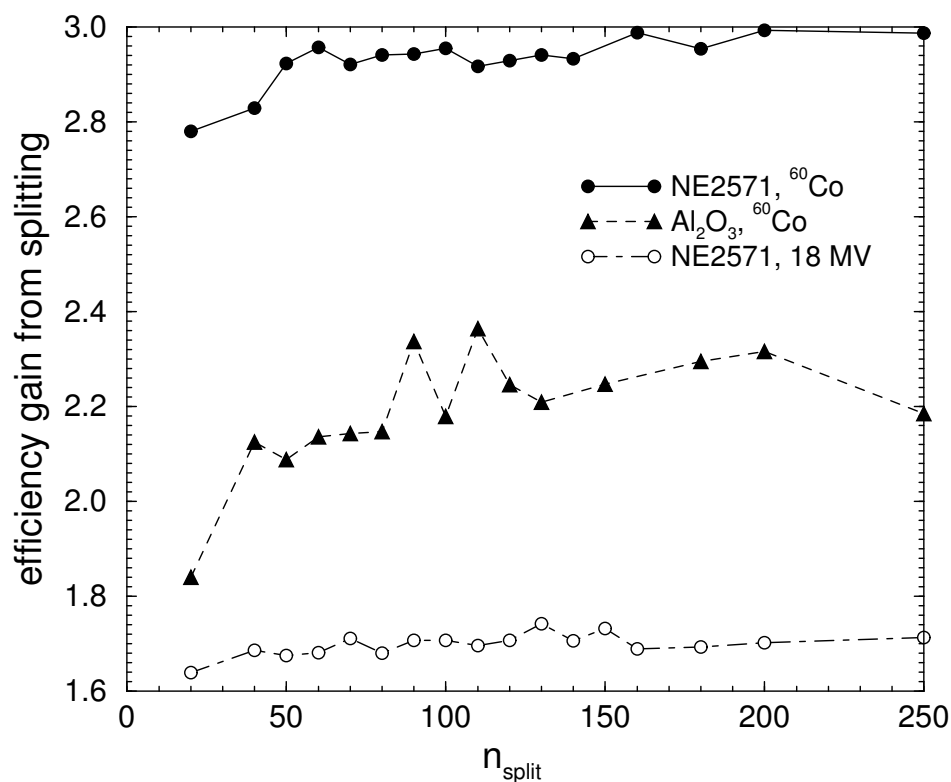


Figure 3.5: The efficiency gain due to the photon splitting variance reduction technique as a function of the splitting number. The calculations are all performed using the CSnrc code and are computing a ratio of doses. In two cases the quantity being calculated is the central electrode correction factor for an NE2571 chamber and in the third case it is the ratio of doses between an Al_2O_3 pellet and water in phantom. All calculations are at 10 cm depth in a water phantom.

correction), the efficiency gain, G , of CSnrc relative to CAVRZnrc, is given by:

$$G = \frac{k}{1 + \alpha(k - 1)} \frac{s_{uncorr}^2}{s_{corr}^2}, \quad (3.15)$$

where k is the number of geometry options begin considered in a single execution of CSnrc, α is the fractional increase in computing time for each geometry option beyond the first one, and s_{uncorr} and s_{corr} are the uncertainty estimates on the dose ratios for the uncorrelated (CAVRZnrc) and correlated (CSnrc) cases, respectively. This assumes that for the same number of histories, the computation time required for an independent run of a single geometry is the same for each of the geometry options. This assumption was investigated using CSnrc by executing CSnrc for only one geometry in a single run and comparing the execution times for two different runs. This was investigated for several of the test geometries shown in Table 3.2. For two similar geometries (varying only by the material in certain regions), the execution times agreed to within 10% and were typically in agreement at the 1-2% level.

For the test cases considered here, values of α vary from 0.004 to 0.98 and are shown in Table 3.2. As expected, for geometries in which the source is incident directly upon the correlated sampling region, α is large since the entire history is repeated and there is no savings in time. Conversely, for in-phantom calculations, where large parts of the particle trajectories are outside of the correlated sampling region and are only transported once, α is very small. In order to include the rectangular phantom geometries, which cannot currently be computed using CAVRZnrc, α is computed by comparing the computation times for a CSnrc calculation using two geometries to a CSnrc calculation with correlated sampling turned off (*ie.* only a single geometry). Compared to CAVRZnrc, CSnrc used with no correlated sampling takes slightly longer due to several conditions in the code that are used to verify whether or not correlated sampling is being used. For the geometries considered here that can be used with both

codes, CSnrc took between 3% and 10% longer than CAVRZnrc for a dose calculation in a single geometry.

The efficiency gain is expected to increase as the degree of correlation increases. For the seven realistic test cases described in Table 3.2, Fig. 3.6 shows the gain in efficiency of CSnrc over CAVRZnrc as a function of the correlation coefficient, ρ . As expected, the gain increases with increasing ρ . Each of the calculations was performed using only two geometry options (*ie.* $k = 2$). A further gain, up to a factor of 3 above the gains shown in Fig. 3.6, can be achieved when executing CSnrc with as many as ten geometry options, since, as k increases in Eq. 3.15, there is greater savings in computation time as more geometries are considered.

Figure 3.6 shows that for cases that show a reasonable degree of correlation, the efficiency gains vary between 8 and 64. Ma and Nahum⁶⁴ report typical efficiency gains of 10 to 100 for a single additional geometry using a thimble chamber geometry. Similarly, Holmes et. al.⁶³ report mean efficiency gains of 2 to 200 for electron-beam calculations. More recent calculations by Hedtjärn et. al.⁶⁶ also show efficiency gains between 10 and 100 for most cases. For some very simple slab geometries that show a high degree of correlation ($\rho = 0.996$), the gain is as high as a factor of 400 using CSnrc.

3.4.4 Comparison to EGS4

A previous investigation using the EGS4 correlated sampling code, studied the effect of the central electrode on the response in an NE2561 ionization chamber as a function of the incident electron energy.⁷⁵ The CSnrc code should reproduce this earlier study with similar efficiency gains and results since the CSnrc algorithm is developed from

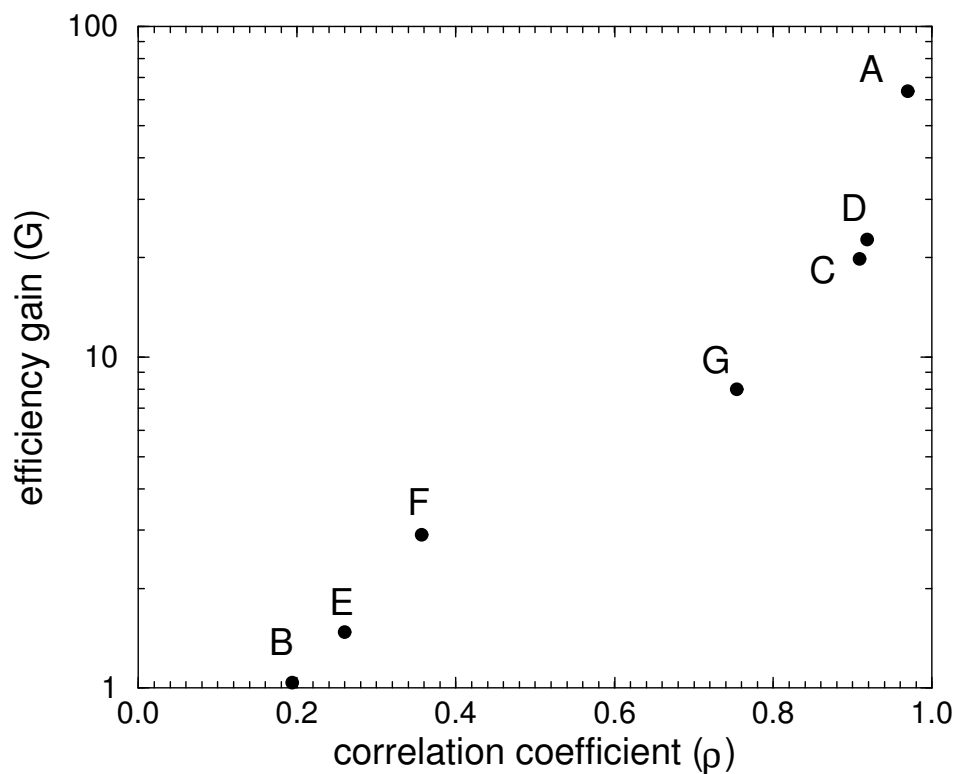


Figure 3.6: Gain in efficiency achieved by CSnrc compared to CAVRZnrc, as a function of the degree of correlation between geometry options. The efficiency is computed for the calculation of the ratio of doses to the cavity for two geometry options. The calculations are performed using photon splitting with a splitting number of 130. The labels refer to the test geometries in Table 3.2.

the algorithm used with the EGS4 code.

In accordance with the study by Ma and Nahum,⁷⁵ a modified NE2561 geometry is used and the chamber is modeled to have a wall thickness of 0.090 g/cm^2 , with a sensitive air cavity 9.0 mm in length and having a diameter of 7.4 mm . The central electrode is hollow and has an outer diameter of 1.76 mm and an inner diameter of 1.4 mm , with a length of 6.4 mm . The chamber was placed in air, with a broad, parallel beam of monoenergetic electrons incident from the side. All calculations use $AE = 521 \text{ keV}$ and a photon cutoff energy of $AP = 1 \text{ keV}$. The EGS4 calculations are also repeated using an existing version of the EGS4 code, using the same calculation parameters and with the maximum fractional energy loss for an electron step, *ESTEPE*, set to 0.04 in order to match the value used by Ma and Nahum in their study.

CSnrc was used to compute the ratio of the cavity dose with an aluminum electrode, D_{Al} , to the cavity dose with a graphite electrode, D_{gr} . Figure 3.7 shows the ratio D_{Al}/D_{gr} for the NE2561 chamber as a function of incident electron energy for monoenergetic beams. As expected, the presence of the aluminum electrode increases the ionization in the chamber, except at very low energies, where the electrons cannot penetrate the aluminum electrode. The figure shows close agreement between the CSnrc calculations and the current EGS4 calculations. The EGSnrc calculation for the two electrode materials provided a gain in efficiency of, on average, 15.1 over the same calculation using CAVRZnrc. This is comparable to an average gain of 17.0 achieved by the current EGS4 calculations compared to CAVRZ. For the CSnrc calculations, the gain varied from 12.8 at 0.8 MeV to 16.9 at 25 MeV . The correlation coefficient varied from 0.87 to 0.90 over the same energy range. Changes in the EGS4 code since the time of their work may account for some of the differences seen between

the Ma and Nahum results and the current EGS4 calculations. These changes in EGS4 altered the sampling routines for the Møller cross-sections and were shown to have noticeable impact on the results for certain applications using high-energy electron beams.⁷⁶

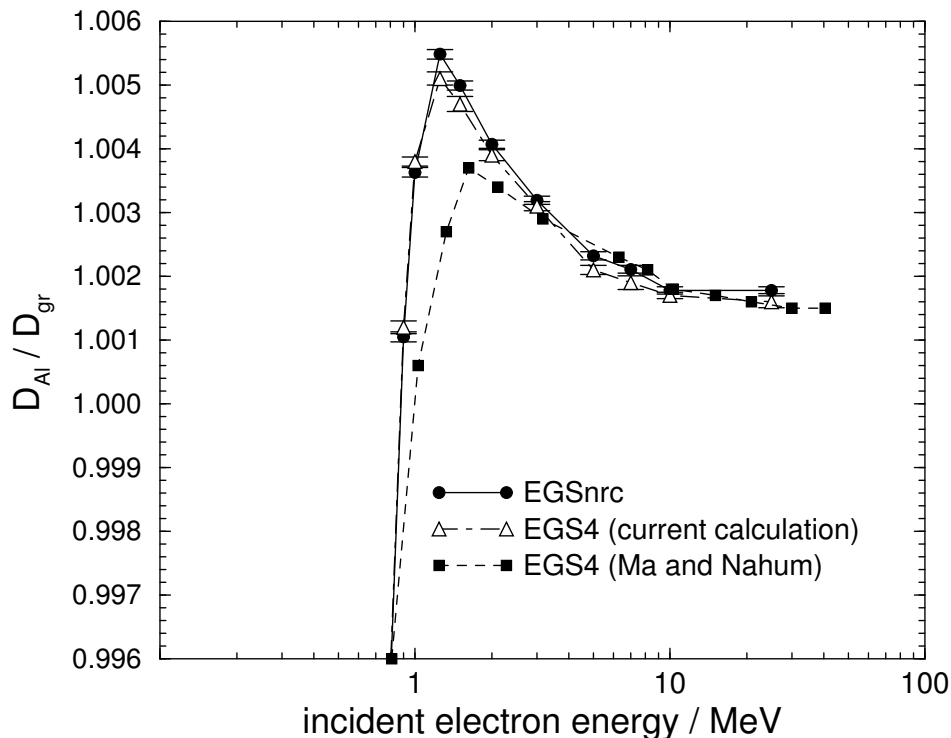


Figure 3.7: Ratio of dose to the gas for an NE2561 chamber with an aluminum central electrode versus that with a graphite electrode, D_{Al}/D_{gr} , as a function of incident electron energy. The present calculations are performed using monoenergetic electron beams with $AE = 521$ keV, $AP=1$ keV and a splitting factor of 130. The points from Ma and Nahum are digitized from Figure 5 of their paper.⁷⁵

3.5 Summary

This chapter describes a new user-code for the EGSnrc system that uses a correlated sampling variance reduction technique to improve the efficiency of ion chamber

calculations. The code was extensively benchmarked against the existing user-code CAVRZnrc and against an earlier correlated sampling code used with the EGS4 system. Tests show gains in efficiency between a factor of 8 and 64 for some realistic test cases. The application of CSnrc user-code to ion chamber calculations will be described in greater detail in Chapters 5 through 7 in relation to the calculation of ion chamber correction factors.

Chapter 4

Systematic uncertainties

Every Monte Carlo calculation has an associated statistical uncertainty. This uncertainty represents the precision with which the quantity of interest is calculated. The statistical uncertainty is a function of the number of histories being simulated, N , and decreases as $1/\sqrt{N}$. Conversely, the accuracy of a Monte Carlo calculation is determined by the transport physics and the cross section distributions used. It is possible to verify the physics by performing a calculation for a situation that satisfies the Fano theorem⁵⁷ and can be computed analytically. EGSnrc is the only Monte Carlo system shown in this way to be accurate to within 0.1%, with respect to its own cross-sections.^{36,37} The accuracy of a Monte Carlo code must be with respect to its cross-sections, since these data could be flawed, but such errors would not show up in a self-consistent check. There has been sufficient comparison with experiment that shows good agreement between Monte Carlo results and measured values, that one does not expect glaring inconsistencies in the cross-sections. Despite this, a Monte Carlo calculation is only as accurate as its cross-sections and therefore there are systematic uncertainties inherent in the simulations.

4.1 Photon cross sections

4.1.1 Variations in photon cross-sections

A potential source of inaccuracies in the Monte Carlo calculation is from the cross-section databases that are used to generate the material data. EGSnrc relies upon a stand-alone utility program, PEGS4,²⁷ to generate much of the material cross-section data for the simulations. PEGS4 uses a set of inputs in order to generate cross-section data for a given element or compound over the energy range specified by the user. The user creates a data file containing the cross-section information for all of the materials involved in a given simulation. For certain interaction cross-sections, PEGS4 determines the cross-section information by interpolation of existing data tables and for compounds, combines these to produce an overall data set for that material. If there are errors within the cross-section database used to generate the material data for EGSnrc, there will be an underlying systematic uncertainty in all of the simulations using these materials.

Studies that calculate photon cross-sections estimate the uncertainty on these values to be on the order of 1% for the materials and energies of interest in this work.^{77,78} CSnrc includes a feature that allows the user to vary the photon cross-sections for each medium in the geometry. This feature is taken from CAVRZnrc which already has this capability.⁷³ By forcing the cross-sections to vary by a known amount, it is possible to estimate the uncertainty in a given calculated quantity due to uncertainty in the cross-sections.

In order to investigate the effect of uncertainty in the photon cross-sections on calculations of the wall correction, CSnrc is used to calculate P_{wall} for an NE2581

chamber in a ^{60}Co beam. The chamber is placed at a depth of 10 cm in a water phantom and the cross-sections are varied by up to 5% in either direction from the tabulated values in the EGSnrc system. Figure 4.1 shows Monte Carlo calculated values of P_{wall} as a function of the percentage change in the cross-section data. As shown later, this chamber has one of the largest calculated values of P_{wall} . If the cross-sections for all of the media within the geometry are varied by the same amount, there is no noticeable change in the value of P_{wall} since a ratio of quantities is being calculated and therefore uniform errors in the cross-section data cancel out. However, when only the cross-section for the A-150 wall is changed, there is nearly a 0.4% change in the value of P_{wall} for a 1% change in the cross-section data. In this case, since the A-150 wall is only present in one geometry, the effect of the cross-section change shows up in the dose ratio since it is being compared to a water wall geometry, where the cross-sections are unchanged. Calculations were also performed by decreasing the cross-sections by the same magnitudes as the increases shown in Fig. 4.1 and the magnitude of the effect on P_{wall} was seen to remain the same. (*ie.* For a 1% decrease in the photon cross-section of A-150, P_{wall} increases by nearly 0.4%.)

Figure 4.2 shows the dose to the cavity for the same calculation described above as a function of the change in the cross-sections. In this case, when only the A-150 cross-sections are changed, there is less effect than when the cross-sections are varied uniformly for all of the media in the simulation. When all of the cross-sections are changed by 1%, there is a 0.7% change in the dose to the cavity. For the case where only the A-150 cross-section is altered by 1%, this effect is 0.4%. Figures 4.1 and 4.2 demonstrate that the effect of uncertainty in the photon cross-sections is dependent on the final quantity being calculated. For P_{wall} , it is estimated that the uncertainty due to the 1% uncertainty in the cross-sections is up to 0.4%. By a similar method,

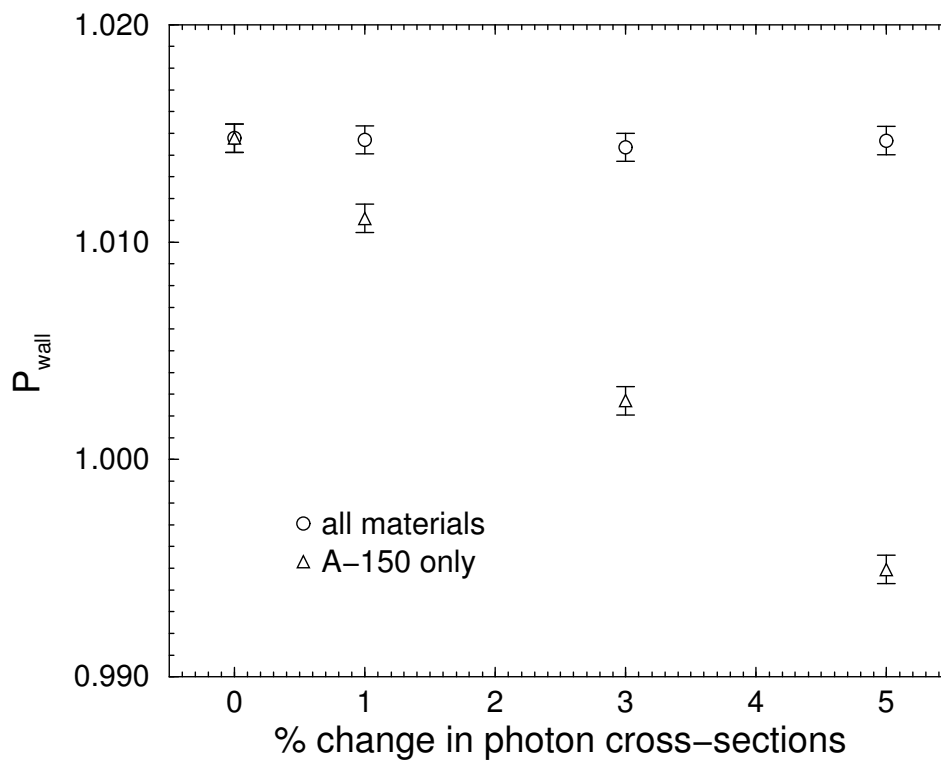


Figure 4.1: P_{wall} as a function of the percentage change in photon cross-sections for an NE2581 chamber in a ^{60}Co beam. The cross-sections were varied manually using a feature in the CSnrc code. Two situations are shown: one in which the cross-section data were varied by the same amount for all materials in the simulation and a second one in which only the cross-sections for the A-150 wall material were varied.

Mainegra et. al. found that the uncertainty on calculated P_{wall} values for parallel-plate chambers was 0.14% for a 1% uncertainty in the graphite cross-section.⁷³

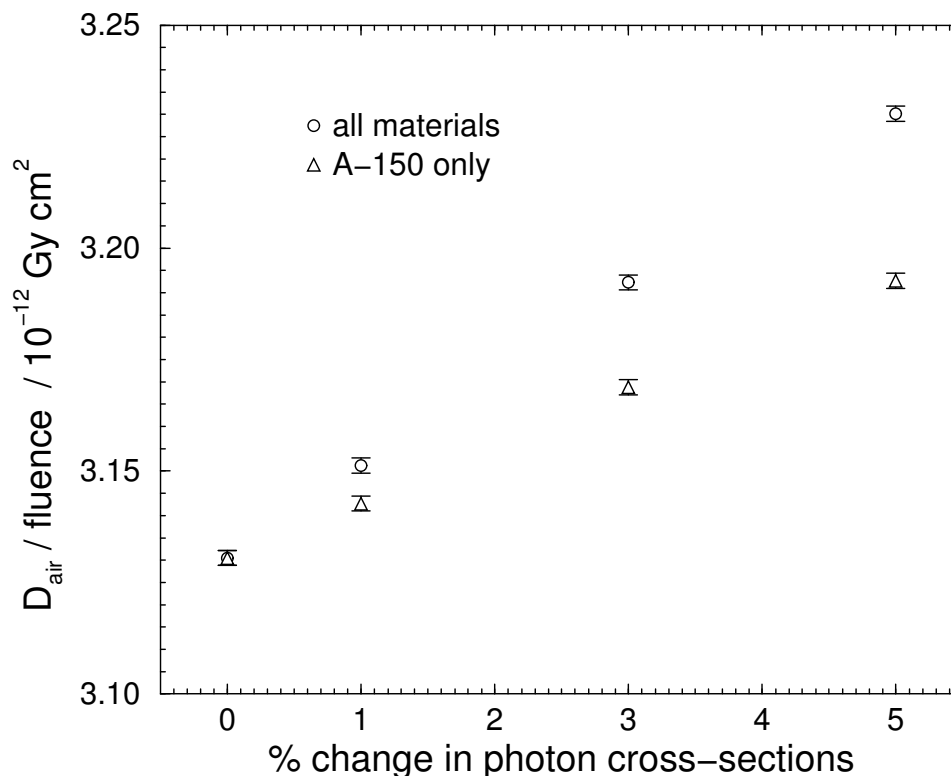


Figure 4.2: Dose to the cavity in an NE2581 chamber as a function of the percentage change in photon cross-sections in a ^{60}Co beam. The cross-sections were varied manually using a feature in the CSnrc code. Two situations are shown: one in which the cross-sections are varied for all of the materials in the simulation and one in which only the A-150 cross-section is varied.

4.1.2 Variation between databases

Another issue worth investigating is the effect of using one cross-section database over another. The default photon cross-section database used in EGSnrc is data from Storm and Israel.⁷⁹ More recent photon cross-sections from the National Institute of Standards and Technology (NIST) XCOM database⁸⁰ improve upon the Storm and

Israel data, particularly for low energies, where the photoelectric effect is of greater importance. The XCOM cross-section data have recently been implemented into EGSnrc.³⁷ For the energies of interest here (> 1 MeV), there is little difference expected between the results using the two databases, since the differences lie primarily in the photoelectric effect cross-sections and are significant at lower energies. Seuntjens et. al.³⁷ showed that at lower energies there were significant differences in both chamber response and mass energy absorption coefficients, dependent on the specific materials being used. Despite the similarities between the cross-section databases for the energies used here, for completeness, it is worthwhile to investigate the effect of using the XCOM database instead of the default EGSnrc cross-sections.

Figure 4.3 shows mass energy absorption ratios for three chamber wall materials relative to water. These are used when computing P_{wall} from the Almond-Svensson formula (Eq. 2.5). The mass energy absorption coefficients are computed using the EGSnrc user-code g, and are averaged over the photon energy spectrum at the point of interest. The input spectra are computed using the user-code FLURZnrc to determine the photon energy spectrum on the central axis at 10 cm depth in water for each of the incident photon beams. The incident photon beam spectra are taken from previously published spectra^{45,47} described in Table 1.2. Figure 4.3 compares the mass energy absorption ratios computed using the FLURZnrc and g user-codes with the Storm and Israel cross-sections to the ratios calculated using the XCOM database. As expected, for the materials and energies considered here, there is no significant difference between calculations using the two sets of material data. Changes in the cross-sections can also change the calculated beam quality specifier $\%dd(10)_x$, however given the good agreement between the calculations using the two databases, one does not expect noticeable changes in $\%dd(10)_x$ in this case. The values of $\%dd(10)_x$

used in Fig. 4.3 are taken from Kalach and Rogers.⁴⁹ Figure 4.3 also shows the mass energy absorption ratios used in the TG-51 protocol which are taken from the calculations of Cunningham done for TRS-277 using the techniques described elsewhere.⁸¹ These show good agreement with the EGSnrc values except for at a few points, where they differ from the EGSnrc values by up to 0.3%. This agreement will be important in the discussion of P_{wall} for thimble chambers in Chapter 6.

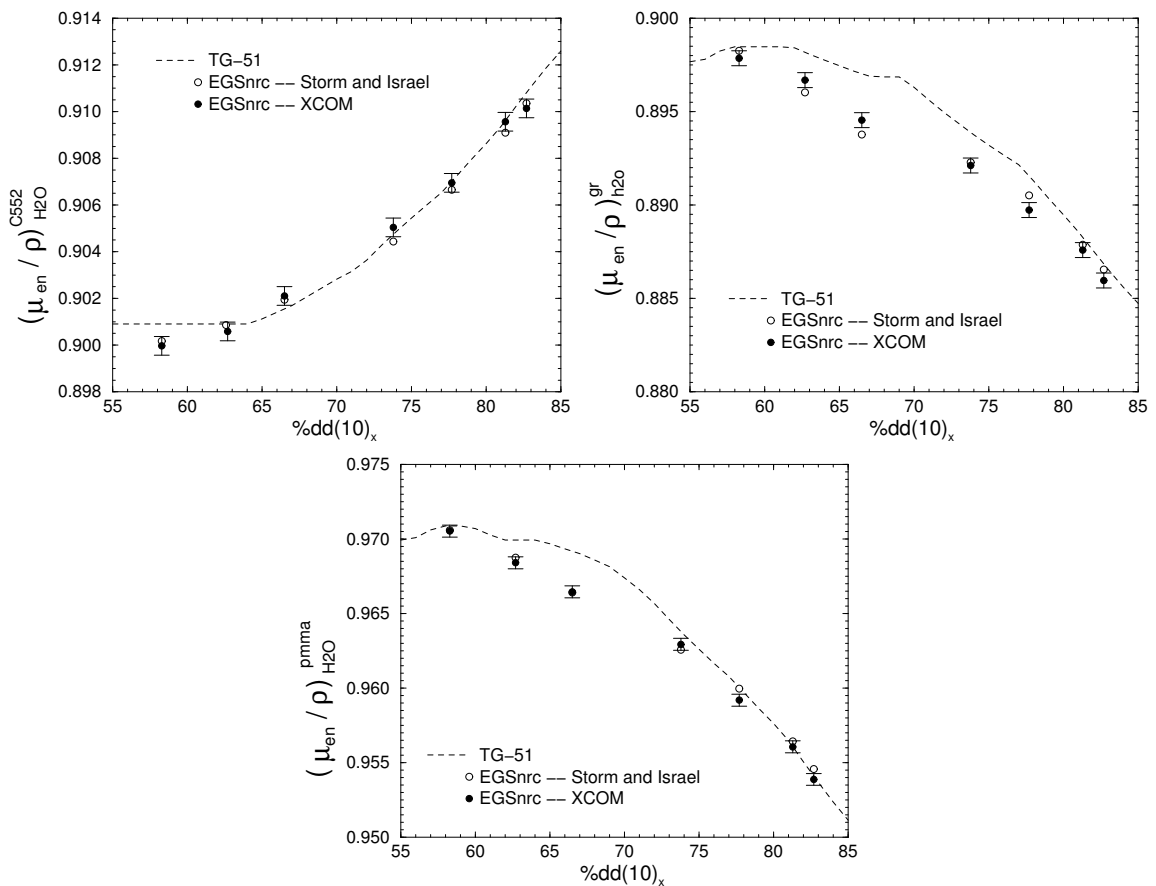


Figure 4.3: Ratios of mass-energy absorption coefficients for three chamber wall materials relative to water. The EGSnrc calculations are performed using photon spectra at 10 cm depth in a 10×10 cm² field as calculated with FLURZnrc and the user-code g with both the XCOM⁸⁰ and Storm and Israel⁷⁹ cross-section databases and a cutoff energy $AE = 521$ keV. These are compared to the values from Cunningham⁸¹ used by the TG-51 protocol. The statistical uncertainty on two sets of EGSnrc calculations is of the same magnitude, but for clarity, only one set of error bars is shown.

Given the close agreement between the mass-energy absorption coefficients using the XCOM and the Storm and Israel databases for the materials and energies of interest to this work, there is no uncertainty expected in any of the calculations relating to the use of one databases instead of the other. Most of the subsequent calculations in this work are performed using the XCOM database, with the exception of the central electrode correction factors discussed in Chapter 5, which were calculated prior to the widespread implementation of the XCOM database in EGSnrc and are calculated using the Storm and Israel values.

4.2 Electron cross-sections

In addition to uncertainties arising from the photon cross-sections as discussed in the preceding section, there are also systematic uncertainties associated with the electron cross-sections used in the simulations. These uncertainties impact the accuracy of the restricted stopping-powers ratios used in the calculations. Accurate knowledge of the stopping-power ratios is important in the calculation of the dosimetry correction factors investigated in the current study and will be of particular importance in the discussion of P_{wall} values for thimble chambers in Chapter 6. In that chapter, EGSnrc calculations of P_{wall} will be compared to the standard formalism, which makes use of the Spencer-Attix restricted, mass-collision stopping power ratios, $(\bar{L}/\rho)_{med2}^{med1}$. In a Monte Carlo simulation, errors in the stopping powers for a given material would impact the electron transport within that medium.

4.2.1 Mean excitation energy

The stopping-powers and stopping-power ratios are dependent on the mean excitation energies for each material, I , which are weighted, geometric averages of the excitation energies of each medium. The weighting factor depends on both the physical state and the electronic structure of the material. For many materials, it is necessary to determine the mean excitation energy from experimental data. Very often, this is done by inferring I from stopping-power or range measurements, since it cannot in general be computed as accurately from atomic theory. For graphite, a commonly used material in ionization chambers, there is evidence that the value of the mean excitation energy requires further investigation. The ICRU Report 37⁸² uses a value of $I = (78 \pm 7)$ eV for graphite, based on experimental data for proton stopping powers at high energies. More recent experiments⁸³ yield much lower uncertainty on I and suggest a value of $I = (86.9 \pm 1.2)$ eV for graphite.

Changing the value of I implies a change in the calculated stopping-power ratios, and calculations using EGSnrc show the effect on calculated dose ratios. Table 4.1 shows the ratio of doses for a graphite-walled chamber to an aluminum-walled chamber for the two values of I for graphite discussed above in a ^{60}Co beam. The chamber in this case was modeled after the experimental set-up of Nahum et. al.⁸⁴ The experimental dose ratio reported by Nahum et. al. is shown for comparison and is seen to fall between the two ratios calculated using EGSnrc with different I values. For the two EGSnrc calculations, the difference in the dose ratios, due to the change in I -value, is 1.2% or 1.3% depending on the density effect correction (discussed below).

Further to this comparison, the cavity dose was computed for an aluminum chamber having varying thicknesses of a graphite dag layer on the inner wall and

Table 4.1: Comparison of dose ratios of the chamber response in a ^{60}Co beam for a chamber with an aluminum wall to that with a graphite wall, $D_{air}^{Al}/D_{air}^{gr}$. The values are from the experimental data of Nahum et. al.⁸⁴ and CAVRZnrc calculations. The experimental data has been corrected for impurities in the aluminum and the CAVRZnrc values were computed using a density correction and a mean excitation energy for graphite as indicated.

Source of dose ratio	$D_{air}^{Al}/D_{air}^{gr}$
Nahum et. al.	1.094 ± 0.003
CAVRZnrc ($I = 78$ eV, $\rho = 1.7$ g/cm ³)	1.1024 ± 0.0004
CAVRZnrc ($I = 86.8$ eV, $\rho = 1.7$ g/cm ³)	1.0890 ± 0.0004
CAVRZnrc ($I = 78$ eV, $\rho = 2.265$ g/cm ³)	1.1017 ± 0.0004
CAVRZnrc ($I = 86.8$ eV, $\rho = 2.265$ g/cm ³)	1.0870 ± 0.0004

was compared to the dose to a pure graphite walled chamber in a ^{60}Co beam. The thickness and composition of the dag layer was varied according to the experimental procedure of Nahum et. al.⁸⁴ Figure 4.4 shows the effect of changing the value of I on the comparison to the measured data from Nahum et. al. Figure 4.4 shows that if the chamber responses are computed for $I = 86.8$ eV, the ratios of chamber responses are shifted from the previous values computed using $I = 78$ eV. As in the case of the pure aluminum wall, the experimental dose ratios for the thin dag layers lie between the two curves calculated for the different I values. This suggests that the discrepancy between the Monte Carlo and the experiment may be accounted for, at least in part, by lack of knowledge of the correct stopping powers.

Changes in the value of I for graphite will affect the calculation of correction factors described in subsequent chapters. While these effects were not explicitly investigated for the central electrode and wall correction factors, Mainegra et. al. estimated that a 4.5% change in the I value for graphite would result in a 0.24%

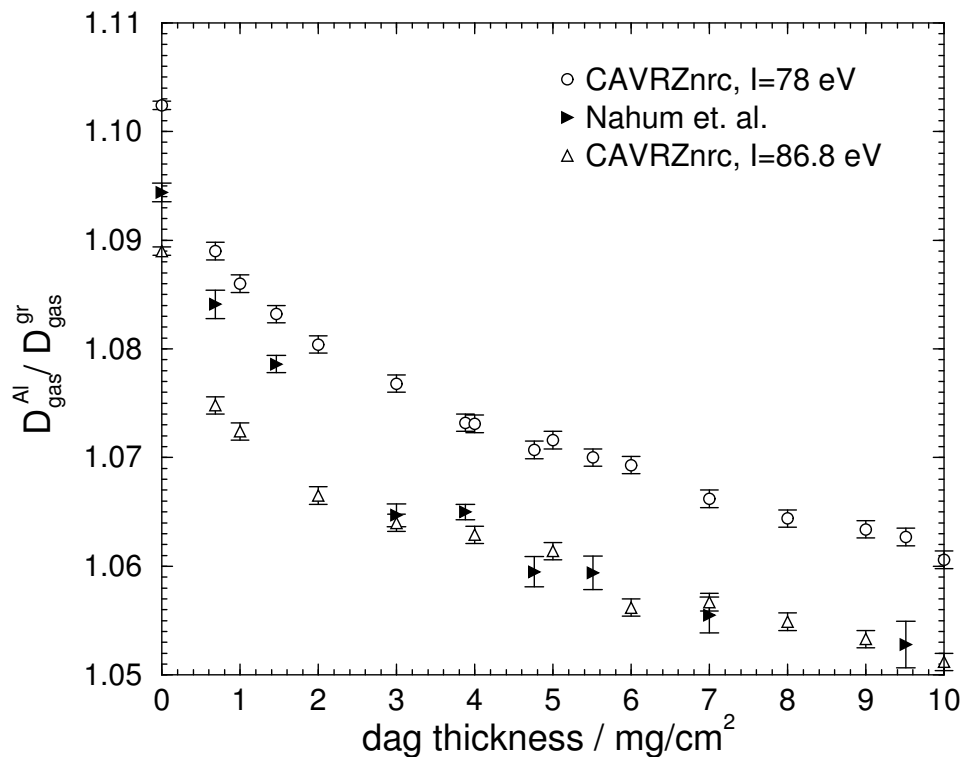


Figure 4.4: The effect of changing the mean excitation energy, I , of graphite, on the relative dose ratio for a chamber having a pure graphite wall to a chamber having an aluminum wall lined with a thin graphite dag layer. The experimental data from Nahum et. al.⁸⁴ are shown as the solid triangles. The CAVRZnrc results were computed using $AE = 512$ keV and used a density of 1.70 g/cm³ for the density-effect correction in the graphite wall.

uncertainty in P_{wall} .⁷³ They used a value of 4.5% for the uncertainty in I since this is the value inferred from the stated uncertainties in the ICRU Report 37.⁸² The change from an I value of 78 eV to a value of 86.8 eV is an 11% change, and therefore it is reasonable to expect that the effect on P_{wall} of this change in I value would be significantly higher than 0.24%.

4.2.2 Electron density effect

Stopping powers are also sensitive to the density-effect correction used in the calculation. As a charged particle moves within a medium it causes the polarization of atoms in the medium, which in turn decreases the electromagnetic field acting on the particle, thereby reducing the stopping power. This effect is more evident in dense materials and has a greater impact on the stopping power at high energies. For certain materials, there is some dispute as to the density that should be used when applying the density correction. In the case of graphite, which is a porous and highly inhomogeneous material, the bulk density of 1.7 g/cm³ used in ICRU Report 37 differs significantly from the grain density of 2.265 g/cm³. It is not obvious which value of the density correction should be used since the theory is intended for homogeneous media, however recent experimental evidence supports the use of the grain density (2.265 g/cm³) when computing the density effect.^{85,86} Also, Zeng et. al. got better agreement with experiment when calculating the ratio of the dose to alanine to that in water by using the grain density of the alanine rather than the bulk density.⁸⁷

Using the geometry of Nahum et. al.⁸⁴ used in the previous section for the pure aluminum and graphite-walled chambers, the effect of the density correction is investigated. Table 4.1 shows the dose ratios for the aluminum to the graphite

chamber for two values of the mean excitation energy and for density effect corrections using both the grain density and the bulk density of graphite. For both values of I , the effect of using one density effect in place of the other is less than 0.2% and is much less than the variation in the dose ratio due to changes in I .

4.2.3 Cutoff energy, Δ

Calculated values of the restricted stopping power are also dependent on the choice of cutoff energy, AE , used in the calculations. In these calculations, AE is total energy of a charged particle, including the rest mass and the kinetic energy. The kinetic energy corresponds to the parameter Δ in the Spencer-Attix theory, that is the lower energy used in obtaining the spectrum-averaged stopping powers. The value of Δ is related to the size of the cavity and is generally taken to be the kinetic energy of an electron that can just cross the cavity.

Table 4.2 shows the restricted stopping power ratios for graphite and aluminum, relative to air for three different values of Δ . The stopping power ratios are computed using the user-code SPRRZnrc with a user-specified value of the cutoff energy. Three values of Δ are chosen: 1 keV, 10 keV and 16 keV. Both 1 keV and 10 keV are commonly used values of AE in Monte Carlo calculations. Furthermore, dosimetry protocols traditionally use a value of $\Delta = 10$ keV.⁶ In primary standards labs, Δ is typically dictated by chamber size. In this case, Δ can be related to the lowest energy of electrons that can just cross the cavity. This is accomplished by computing the mean chord length given by $l = 4V/S$ where V is the volume of the air in the cavity and S is the surface area of the cavity. The value of Δ is then the electron energy for which the CSDA range is equal to the mean chord length. For a

typical thimble chamber, having an inner diameter of 6.30 mm and a cavity length of 2 cm, this method gives $\Delta = 16$ keV.

Table 4.2: EGSnrc calculated values of restricted stopping-power ratios, $\left(\frac{\bar{L}}{\rho}\right)_{air}^{med}$ ($\Delta = AE - 511$ keV), for three values of the electron energy cutoff. All quantities were computed using a ^{60}Co spectrum described elsewhere⁴⁵ and a photon energy cutoff, AP , of 1 keV. The statistical uncertainties in the stopping-power ratios are less than 0.009%.

medium	AE (keV)	$\left(\frac{\bar{L}}{\rho}\right)_{air}^{med}$
Al	512	0.8205
	521	0.8612
	527	0.8654
graphite	512	1.0069
	521	1.0018
	527	1.0012

Table 4.2 shows that there is a large effect on the stopping power ratio by using $\Delta = 1$ keV. However, $\Delta = 1$ keV is much lower than the cutoff energy applicable to the Spencer-Attix cavity theory and is therefore not a realistic value of the cutoff for the chambers being studied here. Such a low Δ value is only included for completeness since a cutoff energy of $AE = 512$ keV is often used in ion chamber calculations. The cutoff energy includes the rest mass of the electron and therefore a 512 keV cutoff corresponds to $\Delta = 1$ keV. This value of AE would not normally be used in the stopping power calculation. However, there is still a significant variation in the stopping power when considering only the commonly used values of 10 keV and 16 keV, where for aluminum there is a 0.5% difference. For consistency with the

dosimetry protocols, all stopping power ratios calculated in this work use $\Delta = 10$ keV. Since this is the commonly accepted value this will not be included in the overall uncertainty estimate on the results, but the results presented here indicate the need for further investigation into the correct value of Δ to be used.

Using the commonly used value of $\Delta = 10$ keV, it is possible to compare values of the stopping power ratio computed using EGSnrc to those used in the dosimetry protocols. Figure 4.5 shows the restricted stopping power ratios for three wall materials (polymethylmethacrylate(PMMA), graphite(gr) and C-552 air equivalent plastic) to air for EGSnrc calculations using the XCOM photon cross-section database. The stopping powers were computed using the SPRRZnrc user-code with an electron energy cutoff of 521 keV. The calculations compute the stopping power ratio of wall material to air for a 0.5 cm thick slab of material along the central axis (radius equals 0.2 cm) at a depth of 10 cm in water. The stopping power ratios in Fig. 4.5 are plotted as a function of $\%dd(10)_x$ in water, taken from Kalach and Rogers⁴⁹ for the photon beam spectra⁴⁷ described in Table 1.2. The EGSnrc values are shown in comparison to the values used by the TG-51 protocol. As with the mass energy absorption coefficients shown in the previous section, there are no significant differences between the EGSnrc values and those used by TG-51.

The choice of cutoff energy may also be expected to affect ion chamber calculations, particularly in electron beam simulations where small geometrical regions are being considered. Of the chambers studied here, the Markus chamber has the thinnest front wall and therefore the effect of the electron cutoff energy, AE , on the value of the wall correction was studied for this chamber. At the low electron energies, the maximum change in P_{wall} for the Markus chamber was 0.3% when changing from $AE = 521$ keV to $AE = 512$ keV and was typically smaller. As will be shown

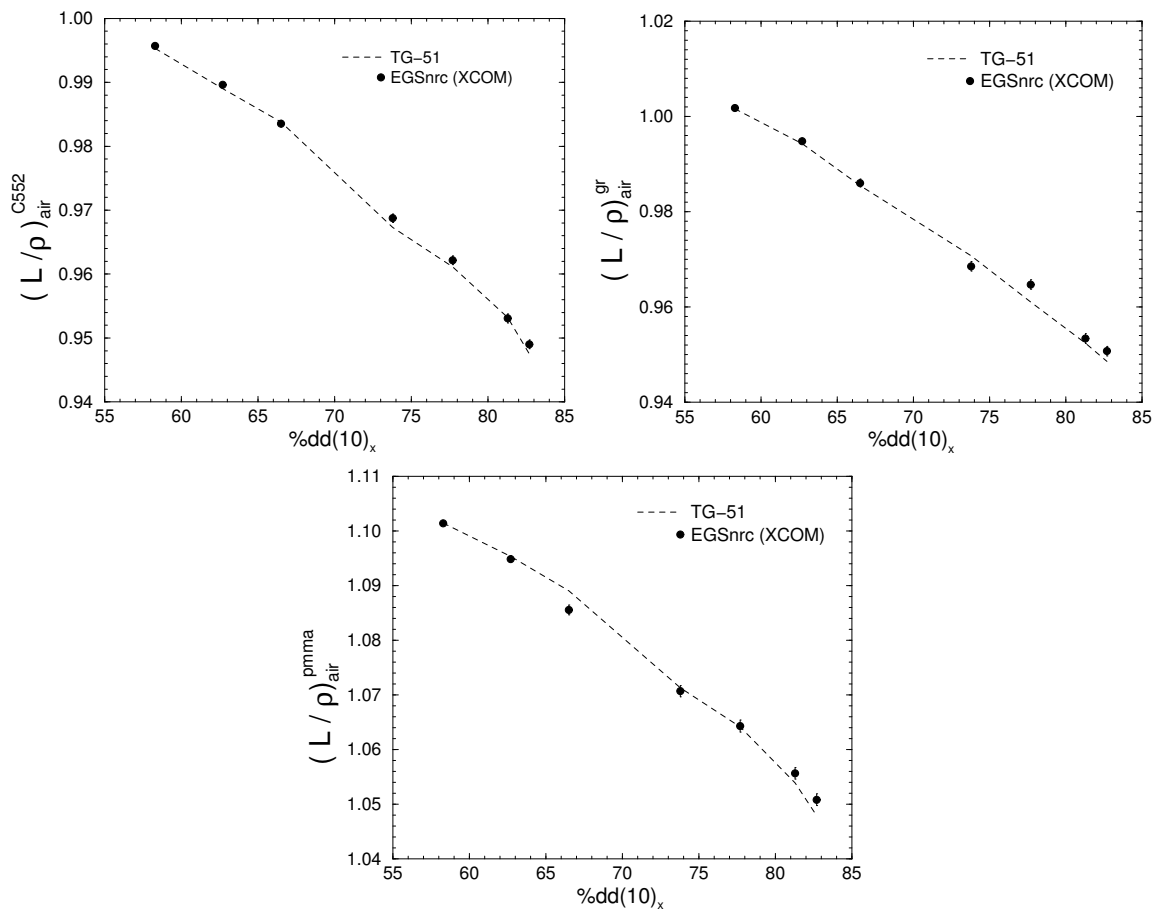


Figure 4.5: The restricted stopping power ratios for three chamber wall materials relative to air. The EGSnrc calculations are performed using the SPRRZnrc user-code with a cutoff energy $AE = 521$ keV and the XCOM cross-section database. These are compared to the stopping power ratios currently used by the TG-51 protocol.

in Chapter 7, these effects are much smaller than the wall correction factors for this chamber in electron beams.

4.3 Summary

Systematic uncertainties in the photon and electron cross-sections will affect the calculations of correction factors. These effects are expected to be larger for the wall correction factor than for the central electrode correction since in the latter case, only the material of the central electrode changes from one geometry to the other. Uncertainties in the cross-section data for the wall material would most likely cancel out in taking the dose ratios, and the contribution to the cavity dose from the electrode is smaller than that from the wall.

In the case of the wall correction factor, Section 4.1.1 describes the effects of a 1% uncertainty in the photon cross-sections on the value of P_{wall} . The current studies, along with those from Mainegra et. al.⁷³ suggest an uncertainty on P_{wall} between 0.14% and 0.4% depending on the material being considered. The other significant contributing factor to the uncertainty in P_{wall} comes from the uncertainty in the mean excitation energy, I , of graphite. Using the value from Mainegra et. al.⁷³ based on the stated uncertainty of the I value by the ICRU,⁸² this is estimated to lead to a 0.24% uncertainty in P_{wall} , although this may be higher if the value of I is changed from its present value of 78 eV. Summing these effects in quadrature, the systematic uncertainty on P_{wall} is between 0.28-0.46% due to uncertainties in the cross-sections.

Chapter 5

P_{cel} in high-energy photon and electron beams

The presence of a central electrode in a thimble chamber affects the measured ionization within the cavity. The central electrode correction factor P_{cel} is defined as the ratio of ionization in the chamber containing no electrode to that in the chamber containing the electrode. Since the design of ion chambers does not permit measurements without the central electrode, P_{cel} must be determined through Monte Carlo calculations, although experiments comparing the effects of different types of electrodes are possible. This chapter describes CSnrc investigations of the central electrode correction factor for graphite and aluminum electrodes.

CSnrc is ideal for calculating the central electrode correction since the only part of the simulation geometry that must be changed is the material of the central electrode. Since only the central electrode changes from one geometry to another, the geometries used in the calculation of P_{cel} maintain a high degree of correlation, leading to potentially large gains in efficiency from using CSnrc.

The CSnrc calculations of P_{cel} specify the electrode as the correlated sampling region. Three geometry options are used: no electrode (or an air electrode), an aluminum central electrode and a graphite electrode. The code outputs the ratio of the doses to the cavity for each of two electrode cases against the no electrode geometry, giving values of P_{cel} . Figure 5.1 shows the three geometries used in the CSnrc calculation. Only the material within the central electrode changes from one geometry to the next.

By the definition of P_{cel} given above, the dose to the cavity with either the graphite or aluminum electrode should be compared to the dose to a cavity that does not have an electrode. In that case, the cavity would be larger, since it would include the volume otherwise occupied by the central electrode. In the execution of the code, this implies that the geometrical regions comprising the electrode would have to be included as cavity regions for the geometry option with no electrode, but would not be a part of the cavity for the cases where an electrode is present. The CSnrc code does not currently handle situations where the number of cavity regions varies from one geometry option to the next. For this reason, instead of having no electrode in one case, the dose is computed for a geometry having an air electrode as shown in Fig. 5.1. In this case, the electrode regions are set to air as they would be if there were no electrode, but these regions are not included in the cavity for scoring purposes. Calculations using separate executions of the code, comparing the presence of an air electrode to no electrode show that the dose to the cavity agrees to within 0.15% and 0.05% for photon and electron beams, respectively, in the two cases. This agreement is within the statistics on the cavity doses of 0.05-0.14% and 0.06-0.07% for the photon and electron beams, respectively. The agreement between calculations using an electrode and no electrode is important since it allows the three geometries shown

in Fig. 5.1 to be used to calculate P_{cel} . In addition to permitting a single execution of the code, by computing all three geometries at once, correlations between the geometries are maintained and the correlated sampling variance reduction technique can be used. All subsequent P_{cel} calculations use an air electrode, although the strict definition of P_{cel} , comparing the dose to the case of no electrode being present, is understood.

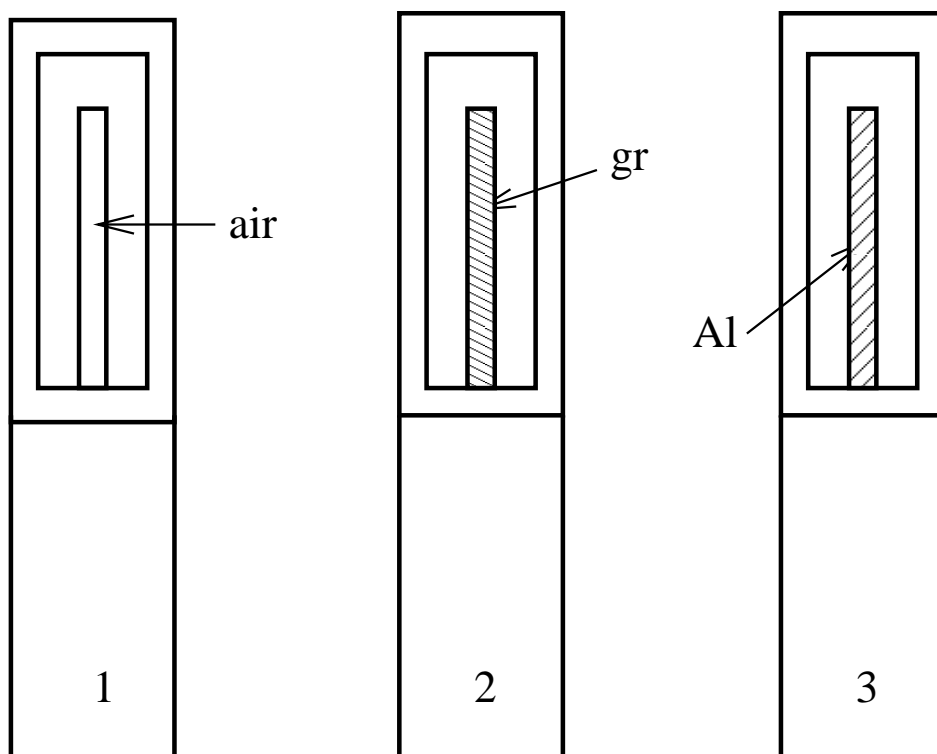


Figure 5.1: Schematic of the three geometry options used in the P_{cel} calculations. P_{cel} is computed as the ratio of either the second or third geometry to the first. The first geometry was modeled to have an air electrode and did not give significantly different cavity doses from the case with no electrode. The only regions to change from one geometry to the next are the regions comprising the electrode.

5.1 P_{cel} in photon beams

In an earlier work, Ma and Nahum⁷⁵ used the EGS4 system to calculate P_{cel} for an NE2571 ion chamber in a water phantom. They modeled the chamber to have an air cavity 6.30 mm in diameter and 24.1 mm in length. The thickness of the graphite walls was 510 mg/cm². They used a simplified NE2571 geometry, so the 1 mm diameter aluminum central electrode extended the entire length of the air cavity. The chamber was placed in a cylindrical water phantom, with a radius of 5 cm for all beams except for the 24 MV beam, for which the radius of the phantom was 7 cm. Their calculations used the ⁶⁰Co spectrum from Rogers et. al.⁸⁸ and the published spectra from Mohan et. al.⁴⁶ for all other photon beams. Their calculations are repeated in the present work using CSnrc. The current calculations are performed with an electron cutoff energy, $AE=521$ keV, with a photon splitting factor of 100 and using the ⁶⁰Co spectrum from Mora et. al.⁴⁵

Columns 2 and 3 of Table 5.1 show the results of the central electrode calculations for the simplified NE2571 geometry with an aluminum electrode. The present CSnrc results are shown alongside the results of Ma and Nahum⁷⁵ which tend to be 0.1% to 0.4% greater than the present calculations. Compared with CAVRZnrc for these calculations, CSnrc results in an efficiency gain that varies from a factor of 21 for a ⁶⁰Co beam to a factor of 33 for a 24 MV beams. The fractional increase in computation time, α , for the additional geometry was between 0.004 and 0.02 for these calculations.

Given the present availability of computing power and the gain from the correlated sampling variance reduction technique, it is feasible to repeat these in-phantom calculations of the electrode correction for a more realistic chamber geometry. The

Table 5.1: The central electrode correction factor, P_{cel} , for an NE2571 chamber having a 1 mm diameter aluminum electrode. The simplified geometry uses a cylindrical phantom and a variation on the electrode length as described in the text, and is shown here for comparison with previously published results from Ma and Nahum.⁷⁵ For the 24 MV beam, the chamber is at a depth of 7 cm in the phantom and is at 5 cm for all other energies. The real NE2571 geometry includes a chamber stem and uses a 30x30x30 cm² cubic water phantom. For the real geometry, the chamber is at a depth of 10 cm in the water phantom for all beams. All current calculations use $AE=521$ keV and a photon splitting factor of 100.

Beam descriptor	P_{cel} , simplified NE2571		P_{cel} , real NE2571
	Ma and Nahum ⁷⁵	CSnrc	CSnrc
⁶⁰ Co	0.9926(15)	0.9923(1)	0.9924(3)
4 MV	0.9935(7)	0.9920(1)	0.9927(3)
6 MV	0.9930(1)	0.9920(1)	0.9942(6)
10 MV	0.9945(9)	0.9915(1)	0.9945(5)
15 MV	0.9955(16)	0.9918(1)	0.9946(4)
24 MV	0.9957(9)	0.9919(1)	0.9948(3)

geometry in this case is the actual NE2571 geometry, wherein the electrode has a length of 20.6 mm and the chamber is placed in a 30x30x30 cm³ cubic water phantom, as is used in standard dosimetry practice. The chamber is placed at 10 cm depth within the phantom and a 10x10 cm² photon field is incident on the phantom surface. Using the same photon beams as above, the values of P_{cel} for the NE2571 chamber are shown in the last column of Table 5.1. The values change by up to 0.3% from the simplified geometry, but these changes nearly offset the differences with the original results of Ma and Nahum.

These calculations of P_{cel} for the detailed NE2571 geometry in a water phantom may be compared to the values of P_{cel} currently used in dosimetry protocols. Figure 5.2 shows P_{cel} as a function of $\%dd(10)_x$, for both graphite and aluminum electrodes, in comparison to the values currently used in the TG-51 protocol.⁷ The TG-51 values are based upon the calculations of Ma and Nahum described above.⁷⁵ The current calculations significantly reduce the uncertainty of the value of P_{cel} and agree with the values used by TG-51 to within 0.04%, with the exception of the $\%dd(10)_x = 85\%$ point, which shows a 0.1% difference. The IAEA protocol⁹ uses values of P_{cel} for photon beams based upon the same calculations from Ma and Nahum, and their values do not differ significantly from the TG-51 values. The tacit assumption in the protocols is that the values of P_{cel} for the NE2571 chamber can be applied to all thimble chambers.

5.1.1 Effect of electrode size

The central electrode correction is normally presented for a 1 mm diameter central electrode of a given material. This diameter is used since it is applicable to most

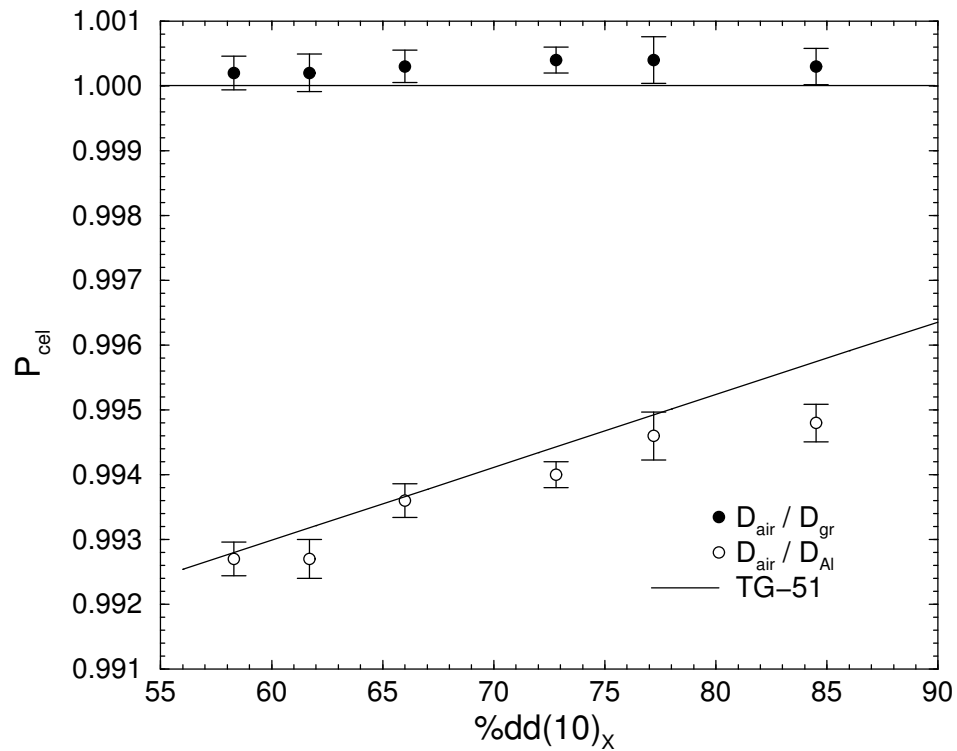


Figure 5.2: The central electrode correction factor, P_{cel} , for a realistic NE2571 ionization chamber in photon beams. The CSnrc values are computed with the chamber at a depth of 10 cm in a 30x30x30 cm³ water phantom. The calculations are for a 1 mm diameter central electrode. The Monte Carlo values are shown along with the curve used in the TG-51 dosimetry protocol.⁷ All CSnrc calculations use $AE=521$ keV and $AP=1$ keV.

commonly used ion chambers. For chambers that have larger or smaller electrodes, it is of interest to investigate the effect of the electrode diameter on the value of P_{cel} . Figure 5.3 shows P_{cel} as a function of central electrode diameter for an NE2571 chamber in a ^{60}Co beam and in a 24 MV beam for both an aluminum and a graphite electrode. For the graphite electrode, there is no statistically significant effect on P_{cel} from changing the size of the electrode for either beam quality. This is not surprising, as the central electrode correction itself is insignificant in this case. P_{cel} for the aluminum electrode decreases in value with increasing electrode diameter. The rate of decrease is dependent on the beam energy and is steeper for the ^{60}Co beam. For both beam qualities, the decrease in P_{cel} for the aluminum electrode is nearly linear out to a diameter of 2 mm. This is larger than any realistic electrode is likely to be and therefore for electrodes that are not 1 mm in diameter, Fig. 5.3 justifies estimating the wall correction using a linear approximation to the variation in P_{cel} as a function of electrode diameter for these and other beam qualities.

5.2 P_{cel} in electron beams

The value of P_{cel} for a chamber with a 1 mm diameter aluminum central electrode in electron beams differs somewhat depending on the dosimetry protocol being used. The IAEA's TRS-398 code of practice⁹ uses a value of $P_{cel}=0.998$ for all electron beam energies, with an estimated uncertainty of 0.1%. This value is based upon the calculations of Ma and Nahum⁷⁵ and upon the much less precise measurements of Palm and Mattsson.⁸⁹ Based upon the same calculations of Ma and Nahum, the AAPM's TG-51 protocol⁷ uses a value of $P_{cel}=1.000$ for nominal beam energies less than 13 MeV and a value of $P_{cel}=0.998$ for nominal beam energies greater than 13 MeV. Rather than

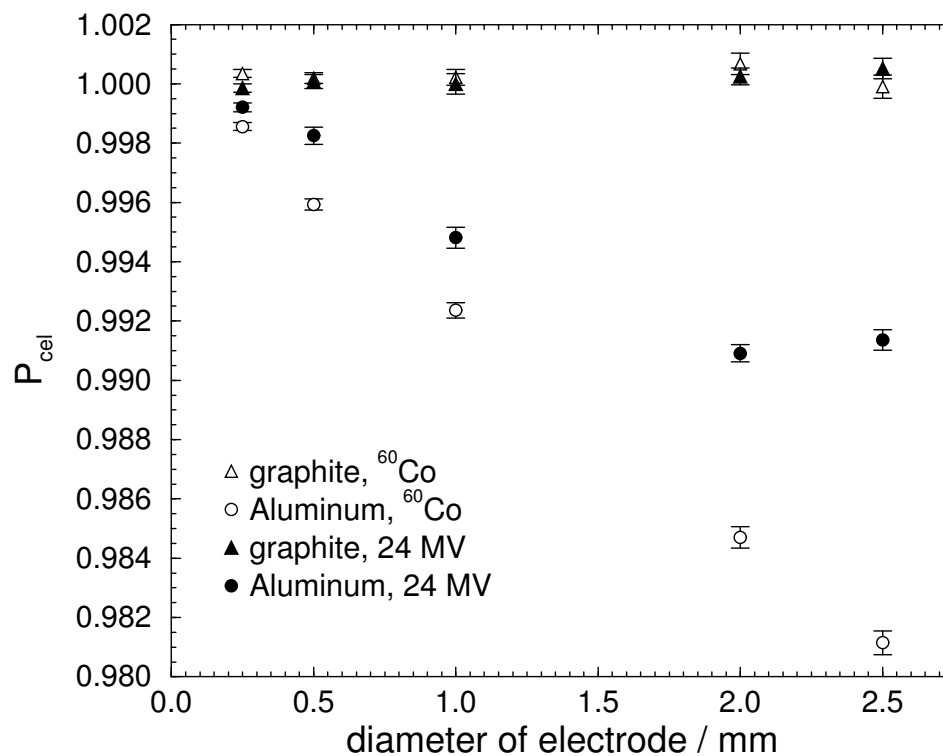


Figure 5.3: The central electrode correction P_{cel} in a ^{60}Co beam and in a 24 MV beam as function of the electrode diameter. The calculations using CSnrc modeled both a graphite and an aluminum central electrode of varying diameters using the NE2571 chamber geometry.

have a discontinuity at 13 MeV, TG-51 uses a smoothed interpolation between the two values of P_{cel} in order to use it in the calculation of the beam quality conversion factor k_Q .

Using CSnrc, it is now possible to calculate the central electrode correction factor P_{cel} for an NE2571 chamber in electron beams with a much lower uncertainty than previously achieved. It is also feasible to perform the calculations for several realistic electron beam spectra and at the new reference depth used in current protocols, whereas the values used in the dosimetry protocols are based upon the three beam energies and the several discrete depths considered in the EGS4 calculations. The present CSnrc calculations use the real NE2571 geometry described in the previous section in a cubic 30x30x30 cm³ water phantom. The incident beam spectra are taken from Ding and Rogers⁴⁸ for all beams, with nominal energy ranging from 5 to 25 MeV. For all beams, the chamber is placed at a depth of d_{ref} , as defined by TG-51, in the water phantom.

Figure 5.4 shows the CSnrc calculated values of P_{cel} as a function of the beam quality specifier R_{50} . The values of R_{50} for the realistic beams considered here are taken from Ding and Rogers.⁴⁸ The CSnrc values are computed to 0.02% statistical uncertainty. These values are shown along with the current values of P_{cel} , as used in TG-51 and in TRS-398. Both protocols use a correction factor of 1.000 for a graphite electrode. However, the current calculations show that for lower energies, the correction is as much as 0.2% for a graphite electrode. The calculations using the aluminum electrode show approximately a 0.1% difference from the value of $P_{cel}=0.998$ used by the TRS-398 code of practice. Similarly, there is on the order of a 0.1% difference between the current calculations and the values used in the AAPM's TG-51 protocol. As in the case of P_{cel} in photon beams, it is assumed that these values for the NE2571

chamber apply for all Farmer-like chambers.

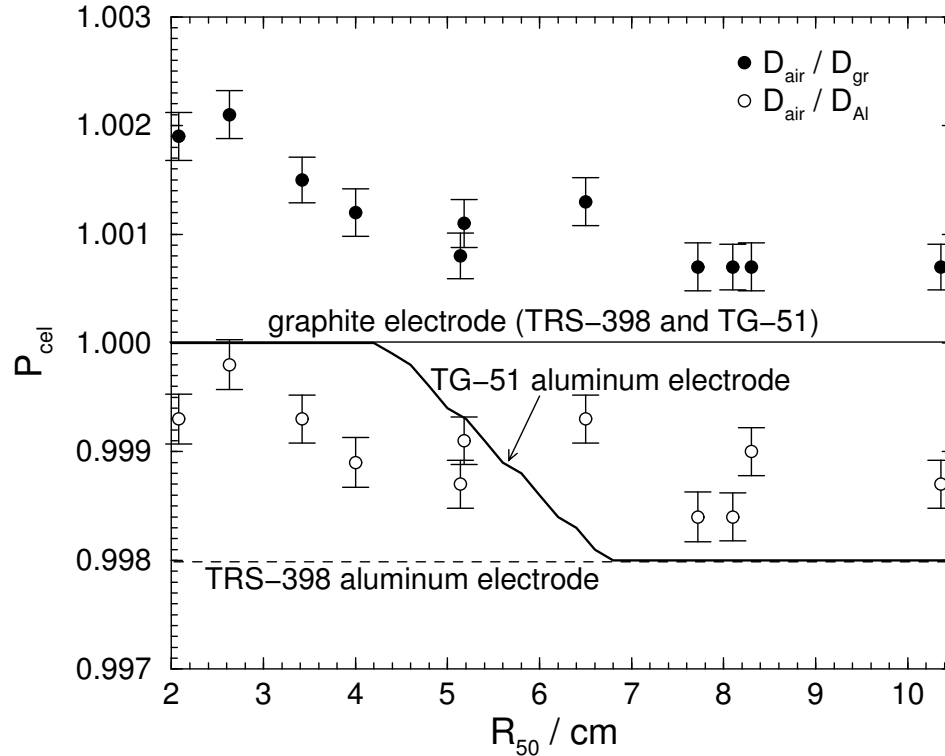


Figure 5.4: The central electrode correction factor, P_{cel} for a realistic NE2571 ionization chamber in electron beams. The CSnrc values are computed with the chamber placed at a depth of d_{ref} in a $30 \times 30 \times 30 \text{ cm}^3$ water phantom. The calculations are for a 1 mm diameter central electrode. The Monte Carlo calculations are shown along with the values of P_{cel} used in the AAPM's TG-51 protocol⁷ and in the IAEA's TRS-398 code of practice.⁹ All calculations use $AE=521 \text{ keV}$ and $AP=1 \text{ keV}$.

5.2.1 Effect of electrode size

As in the case of photon beams, the central electrode correction factor is normally presented for the case of a 1 mm diameter electrode. Figure 5.5 shows P_{cel} as a function of the electrode diameter for the NE2571 chamber in a 6 MeV electron beam. Unlike the photon case where there was no dependence on diameter for the graphite electrode, in electron beams, both the graphite and aluminum electrodes

show an increase in P_{cel} with increasing diameter. The graphite electrode shows a steeper increase in P_{cel} , varying by 0.3% in going from a 0.5 mm diameter electrode to a 2 mm diameter.

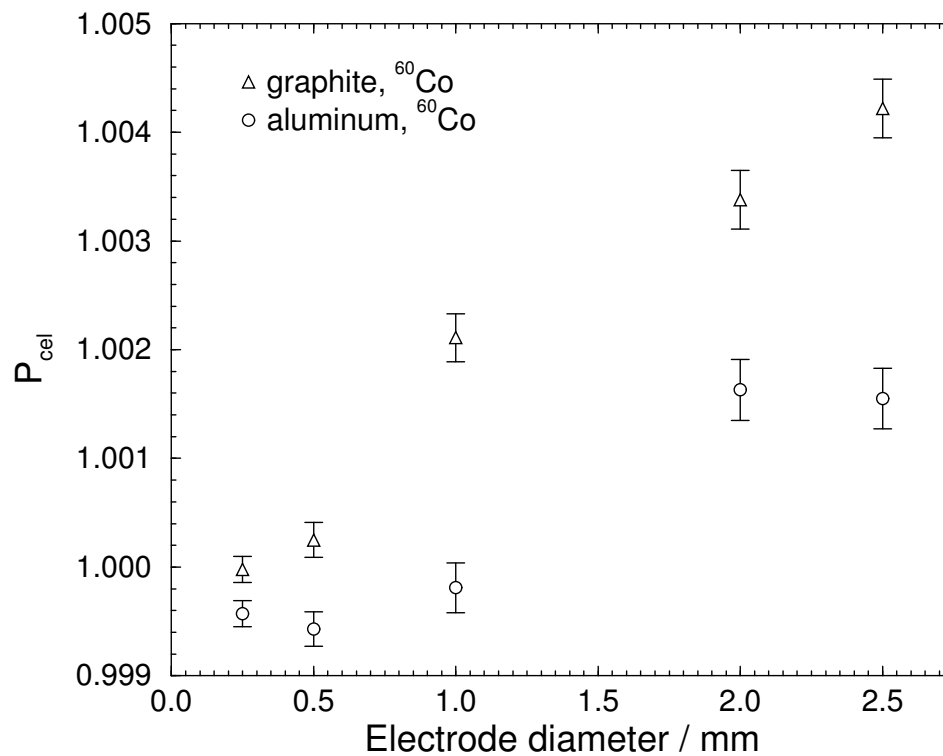


Figure 5.5: The central electrode correction factor, P_{cel} , as a function of the diameter of the electrode in a 6 MeV electron beam. Values were calculated using CSnrc and are shown for both a graphite and an aluminum central electrode in an NE2571 chamber.

Chapter 6

P_{wall} for cylindrical ion chambers: the Almond-Svensson formalism

Section 2.2.3 describes the wall correction factor, P_{wall} , used to account for the chamber wall being a different material than the phantom. P_{wall} is typically determined using the Almond-Svensson formalism given by Eq. 2.5. Experimental determinations of P_{wall} are very difficult since they require extremely precise measurements of the chamber geometry and its response. Furthermore, experimental P_{wall} values may only be determined through extrapolation to zero wall thickness, since the constraints of the physical chamber as the measuring device prevent measurements with a bare chamber. Many investigations of P_{wall} are performed using Monte Carlo simulations.^{73,90-93} These too have inherent difficulties due to the small magnitude of the correction itself. Since the calculations must be carried out in-phantom and require precision much better than 1% in order to gain statistically significant results, Monte Carlo calculations often require hundreds of millions of particle histories. Several studies have shown that there are problems with the current values of P_{wall} ^{18,55,56,94-96}

and therefore this chapter discusses new calculations of the P_{wall} correction factor.

Using CSnrc, P_{wall} is calculated as the ratio of the dose to the air cavity for a chamber wall composed entirely of water to that for real chamber wall. No stem or central electrode is included in the geometry for these calculations since they are properly accounted for by the factors P_{stem} and P_{cel} respectively (see Fig. 2.1). Figure 6.1 shows the geometry used for the CSnrc calculations of P_{wall} . The third geometry includes a 1 mm PMMA waterproofing sleeve, typical of the sleeves used clinically for non-waterproof chambers.

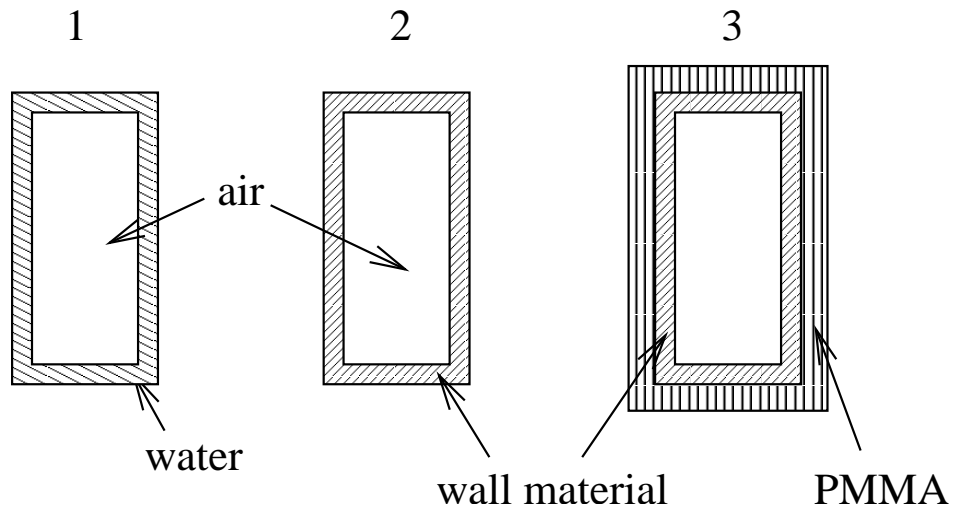


Figure 6.1: Schematic of the three geometry options considered in the P_{wall} calculations. P_{wall} is computed as the ratio of doses to the air cavity for either the second or third geometry to the first. The only regions to change from one geometry to the next are the regions comprising the chamber wall. The three geometries show a water wall, a wall having the correct wall material and a chamber with the real wall material surrounded by a 1 mm PMMA waterproofing sleeve.

6.1 Comparison to P_{wall} and K_{comp} values in photon beams

6.1.1 Corrections for build-up caps in ^{60}Co beams

An experimental study by Seuntjens et. al.¹⁸ showed problems with the P_{wall} and K_{comp} formalism. The concept of K_{comp} is described in Section 2.2.3 (Eq. 2.13, page 32). In their work, Seuntjens et. al. measured the air-kerma to absorbed-dose conversion factor:

$$C_{Co} = \frac{N_{D,w}^{Co}}{N_K}, \quad (6.1)$$

where $N_{D,w}^{Co}$ is the absorbed-dose-to-water calibration coefficient and N_K is the air-kerma calibration coefficient. The expression for C_{Co} is given by Eq. 2.12 on page 32. Seuntjens et. al. measured values of C_{Co} for a PR06C chamber with four different build-up caps and compared these values for different build-up caps to the predictions of the standard formalism given by Eq. 2.12. Their measured values differed from the Almond-Svensson values by as much as 0.90%. Their experimental uncertainty on the C_{Co} values is on the order of 0.6%.

A possible source of the discrepancies between their C_{Co} values and those from the formalism is the expression for K_{comp} . If two C_{Co} values are compared for the same chamber with different build-up caps, in taking the ratio of these C_{Co} values, many of the correction factors in Eq. 2.12 cancel out. Specifically, the mass-energy absorption coefficients and stopping-power ratios are chamber independent and are therefore the same in both cases so drop out in the ratio of C_{Co} values. Furthermore, the correction factors K_{an} , K_{el} , K_{wall} , P_{cel} and P_{repl} are chamber specific and are therefore the same in each case since the same chamber is being used. Only the

K_{comp} correction, which depends on the build-up cap, will not be the same in both cases, and therefore the ratio of the C_{Co} values becomes:

$$\frac{C_{Co}^A}{C_{Co}^B} = \frac{K_{comp}^B}{K_{comp}^A}. \quad (6.2)$$

When comparing the ratio of two C_{Co} values, only the statistical measurement uncertainty is involved, since the ratio does not depend on the systematic uncertainties due to the primary standards. Based upon the uncertainty analysis presented in Table IV of the Seuntjens et. al. paper, the statistical uncertainty on $N_{D,w}$ is 0.08%. The statistical uncertainty on N_K is 0.09%,⁹⁷ resulting in an overall uncertainty of 0.17% on the ratio of two measured C_{Co} values.

Using the CSnrc code, it is straightforward to compute K_{comp} for a PR06C chamber in a ^{60}Co beam. Table 6.1a shows Seuntjens et. al's measured C_{Co} values normalized to the C_{Co} value for the C-552 cap, for which $K_{comp} = 1$ and the calculated values using standard dosimetry theory described by Eq. 2.13. The measured values are shown in comparison to the predictions of Eq. 2.13 and to the CSnrc values. Table 6.1b shows the percent difference between the measured ratio and the ratios from CSnrc and Eq. 2.13 respectively. CSnrc shows much better agreement with the experimental results than do the values from the K_{comp} formalism. The largest percent difference between the CSnrc values and the measured values is 0.13%, whereas this difference is as large as 1.08% for the values computed using Eq. 2.13.

6.1.2 Discrepancies in k_Q values for cylindrical chambers

The formalism used by current dosimetry protocols relies on the beam quality conversion coefficient k_Q , described by Eq. 2.9, in order to convert from a calibration in a reference beam to measurements in the user's beam. The values of k_Q for clinical ion

Table 6.1: (a) The ratios of the air kerma to absorbed dose conversion factors, C_{Co} , as measured by Seuntjens et. al.¹⁸ and normalized to the value using the C-552 cap which is taken as unity. Also shown are the C_{Co} values computed using the K_{comp} formalism of Eq. 2.13 and the physical data as used in TG-51. The CSnrc column shows the ratios of calculated K_{comp} values for the different cap materials relative to a C-552 cap. The uncertainties on the last digits are shown in parentheses. (b) The percent differences between the CSnrc values and each of the measured and Eq. 2.13.

(a)			
Cap material	Measured	TG-51	CSnrc
C-552 (0.493 g/cm ²)	1.0	1.0	1.000
polystyrene (0.537 g/cm ²)	0.9906(17)	0.9799	0.9893(3)
PMMA (0.541 g/cm ²)	0.9913(17)	0.9861	0.9922(2)
delrin (0.551 g/cm ²)	0.9942(17)	0.9902	0.9934(2)
(b)			
Cap material	%diff. ($\frac{Measured}{CSnrc}$)	%diff. ($\frac{Measured}{TG-51}$)	
C-552	-	-	
polystyrene	0.13%	1.08%	
PMMA	-0.09%	0.52%	
delrin	0.08%	0.40%	

chambers are determined through experimental measurements or by using Eq. 2.9. In the latter case, the value of k_Q depends on the stopping power ratios and on the chamber-specific correction factors.

A study by Ross et. al.⁹⁶ of beam quality specifiers in high-energy photon beams showed that ratios of measured values of k_Q did not agree with the ratios calculated using the TG-51 formalism. Specifically, their measurements compared k_Q values for an NE2571 chamber and a PR06C chamber for $\%dd(10)_x$ values in the range 82-92%. Calculations using Eq. 2.9 indicate that k_Q for the NE2571 chamber should be 0.1% or 0.2% higher than that for the PR06C chamber. Ross et. al. showed the reverse effect, with their measured k_Q for the PR06C chamber being about 0.5% greater than that for NE2571 chamber. Their estimated standard uncertainty on the ratio of k_Q values was 0.2%. Since the two chambers share the same cavity dimensions, both the stopping power ratios and the values of P_{repl} are the same for the two chambers. This implies that the discrepancy between measured and calculated values of k_Q is caused by problems with the values of P_{cel} and P_{wall} used, since the other factors in the calculation of k_Q drop out in taking the ratio of values for these two chambers and the ratio of k_Q values is reduced to the ratio of P_{wall} and P_{cel} values:

$$\frac{k_Q^{NE2571}}{k_Q^{PR06C}} = \frac{P_{wall}^{NE2571}(Q)}{P_{wall}^{NE2571}(^{60}Co)} \frac{P_{wall}^{PR06C}(^{60}Co)}{P_{wall}^{PR06C}(Q)} \frac{P_{cel}^{NE2571}(Q)}{P_{cel}^{NE2571}(^{60}Co)} \frac{P_{cel}^{PR06C}(^{60}Co)}{P_{cel}^{PR06C}(Q)}. \quad (6.3)$$

Using values of P_{wall} and P_{cel} from TG-51, the calculated ratio k_Q^{NE2571}/k_Q^{PR06C} is 1.0039. As pointed out by Ross et. al., the inclusion of the P_{cel} factor in this analysis, which was not done in their paper, worsens the agreement between the predictions of TG-51 and their measured ratio of 0.9950. Using CSnrc, values of P_{wall} and P_{cel} can be calculated in order to compare the ratio of k_Q values to the experimental values of Ross et. al. These calculations were performed using the spectra from Sheikh-Bagheri

6.1. P_{WALL} AND K_{COMP} VALUES IN PHOTON BEAMS

and Rogers⁴⁷ and therefore needed to be slightly extrapolated in order to match the beam quality used by Ross et. al. having $\%dd(10)_x = 84.5\%$ ($TPR_{10}^{20} = 0.80$). As will be shown in Section 6.2, P_{wall} is fairly smooth in the range $\%dd(10)_x = 58.9 - 82.7\%$ and therefore is not varying rapidly at the point of extrapolation. Using the values of P_{wall} and P_{cel} calculated using CSnrc, the ratio of k_Q for the two chambers yields a ratio of $0.9984 \pm 0.12\%$. Therefore the CSnrc values of the correction factors significantly improve the agreement between the calculated and the measured k_Q values. Table 6.2 summarizes the values of P_{wall} and P_{cel} used in this analysis.

Table 6.2: Values of the wall and central electrode correction factors used in the calculation of k_Q for the NE2571 and PR06C chambers. The ratio of k_Q values for the two chambers is calculated using Eq. 6.3 and is compared to the experimental ratio from Ross et. al.⁹⁶ for a beam quality Q having $\%dd(10)_x = 84.5\%$. The uncertainties in the last digit are shown in parentheses.

	Correction Factor	NE2571	PR06C	k_Q^{NE2571}/k_Q^{PR06C}
CSnrc	$P_{wall}({}^{60}\text{Co})$	0.9989(7)	0.9886(7)	0.9984(12)
	$P_{wall}(Q)$	1.0004(3)	0.9940(3)	
	$P_{cel}({}^{60}\text{Co})$	0.9924(3)	1.0002(3)	
	$P_{cel}(Q)$	0.9948(3)	1.0003(3)	
TG-51	$P_{wall}({}^{60}\text{Co})$	0.9919	0.9888	1.0039
	$P_{wall}(Q)$	0.9992	0.9951	
	$P_{cel}({}^{60}\text{Co})$	0.9928	1.0000	
	$P_{cel}(Q)$	0.9957	1.0000	
Ross et. al.	-	-	-	0.9950(20)

6.1.3 Comparison of different waterproofing sleeves

The P_{wall} formalism may also be tested by investigating the effect of a waterproofing sleeve on the chamber response and comparing it to the effect predicted by Eq. 2.6. A study by Ross and Shortt⁹⁸ measured the effect of a waterproofing sleeve on chamber response by varying the thickness of the sleeve. They performed measurements using an NE2571 chamber and a PR06C chamber in both a ^{60}Co beam and in a 20 MV photon beam from the NRC linear accelerator. In all cases, the chamber response was measured as a function of the material and thickness of the waterproofing sleeve. Since neither of the two chambers could be used without a waterproofing sleeve, their results were extrapolated to a sleeve thickness of 0 g/cm² in order to determine the effect of the sleeve relative to the bare chamber. Their results showed problems with the P_{wall} formalism used in TG-51.

Current calculations, using CSnrc, revisit the experimental results of Ross and Shortt. The change in chamber response from a chamber with no waterproofing sleeve was calculated as a function of the material and thickness of the sleeve and was compared to their experimental results. These calculations were performed for both an NE2571 chamber in the NRC 20 MV beam and for a PR06C chamber in a ^{60}Co beam. Both chambers were modeled with PMMA and nylon sleeves of varying thicknesses.

Figure 6.2 shows the change in chamber response relative to a chamber with no sleeve as a function of the thickness of a PMMA waterproofing sleeve. The two plots shown are for a PR06C chamber in ^{60}Co and for an NE2571 chamber in the NRC 20 MV beam. They compare the calculated results from CSnrc to the measured results of Ross et. al. and to the values from the extended Almond-Svensson formalism

given by Eq. 2.6. The CSnrc and the measured results show very good agreement, while the predictions of the Almond-Svensson formalism differ from the CSnrc values by more than 0.3% for large sleeve thicknesses. This discrepancy is larger than the predicted effect of the sleeve and points to problems with the formalism.

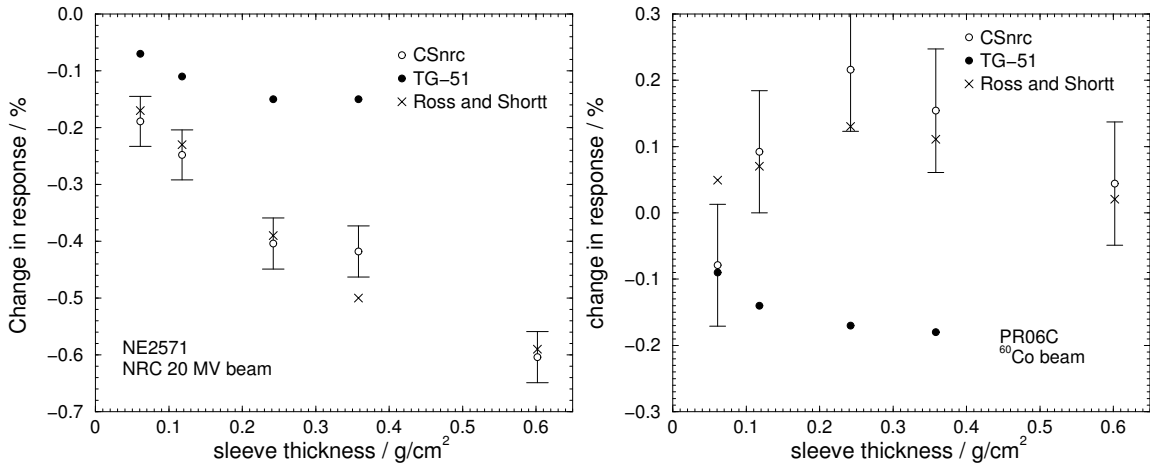


Figure 6.2: The change in chamber response due to the presence of a PMMA waterproofing sleeve compared to the response in a chamber with no sleeve. CSnrc calculations are compared with measured results from Ross et. al.⁹⁸ and the predictions of the formalism and physical data used by TG-51. The plot at left shows the effect for an NE2571 chamber in an NRC 20 MV beam. The plot at right is for a PR06C chamber in a ⁶⁰Co beam.

Figure 6.3 shows two analogous plots for a nylon waterproofing sleeve. As in Fig. 6.2, the plots show the effect of the waterproofing sleeve for an NE2571 chamber in the NRC 20 MV beam and for a PR06C chamber in a ⁶⁰Co beam. In both cases, the CSnrc curves and the measured data show the same shape as a function of sleeve thickness. Furthermore, this shape is vastly different from the Almond-Svensson curve. However, there remains a normalization problem between the CSnrc and experimental curves that is not understood. It is possible that the difference between the CSnrc calculations and the results from Ross et. al. is due to differences in the nylon composition used in the experiment and in the simulations. Nylon is very

sensitive to the manufacturing process and may differ from the accepted composition and density for a given type of nylon. Alternately, there may be problems with how the experimental data are normalized since the calculated values of P_{wall} do not extrapolate linearly to unity at zero sleeve thickness as the experimental values seem to indicate that they do. Despite absolute differences in the sleeve effect for the nylon sleeve, the CSnrc calculations support the experimental evidence from Ross et. al. that the extended Almond-Svensson formalism does not correctly predict the wall correction, at least as applied to the sleeves.

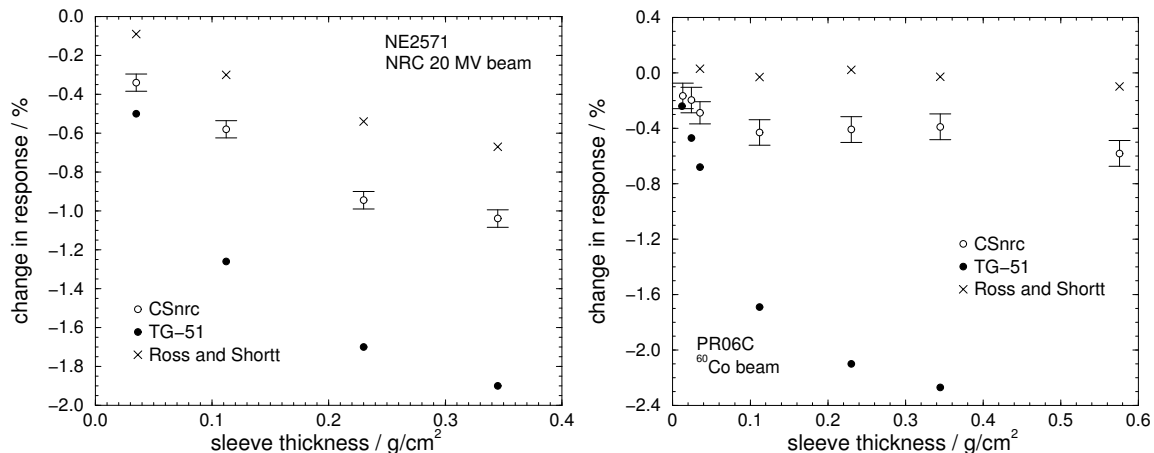


Figure 6.3: The change in chamber response due to the presence of a nylon waterproofing sleeve compared to the response in a chamber with no sleeve. CSnrc calculations are compared with measured results from Ross et. al.⁹⁸ and the predictions of the formalism and physical data used by TG-51. The plot at left shows the effect for an NE2571 chamber in an NRC 20 MV beam. The plot at right is for a PR06C chamber in a ⁶⁰Co beam.

6.2 P_{wall} values in photon beams

6.2.1 P_{wall} for several commonly used ion chambers

In the previous section, examples were shown in which the CSnrc calculations agree better with experiment than does the formalism used in TG-51. For this reason, CSnrc is used to calculate P_{wall} values for a number of commonly used ion chambers at a variety of photon beam energies. At the very least, this provides a complete set of P_{wall} values for many chambers of clinical interest, all calculated at the reference depth and to a very high precision. These values are independent of the TG-51 values which are based on the Almond-Svensson formalism. In addition to providing a set of P_{wall} values, the inclusion of a variety of chambers permits the search for trends in P_{wall} values as a function of energy, wall material and wall thickness. The details of the chamber geometries used are given in Table 1.4 on page 17.

Figure 6.4 shows P_{wall} values for several commonly used ion chambers in high-energy photon beams. The P_{wall} values are calculated using CSnrc with the geometry shown in Fig. 6.1 and with the chamber placed at 10 cm depth in a water phantom. The calculations are performed using the photon beam spectra described by Mora et. al.⁴⁵ and by Sheikh-Bagheri and Rogers⁴⁷ and detailed in Table 1.2. The P_{wall} values are shown for the situation with no waterproofing sleeve since the TG-51 dosimetry protocol ignores the effect of the water-proofing sleeve. The values of P_{wall} in Fig. 6.4 are not easily parametrized in terms of simple functions of the wall material or the wall thickness and therefore Fig. 6.4 serves as a straightforward way to look up P_{wall} for a given chamber.

Current calculations using CSnrc show that the presence of a 1 mm PMMA

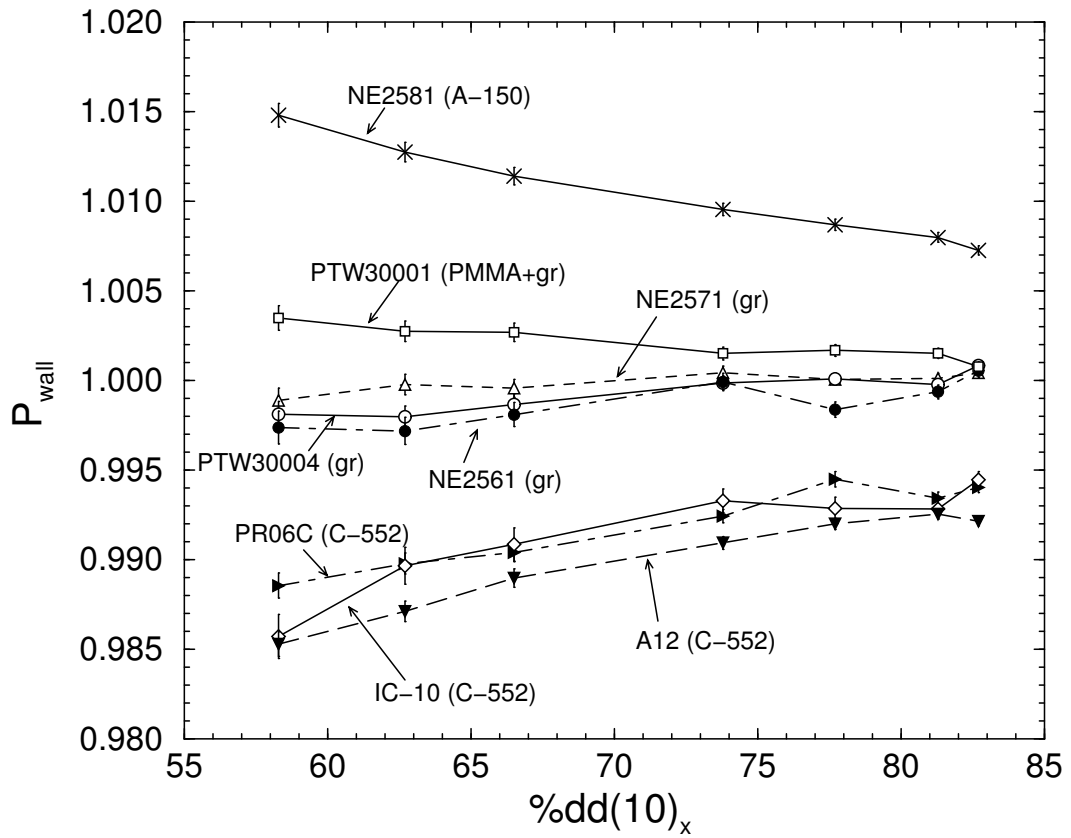


Figure 6.4: The wall correction factor, P_{wall} for several commonly used thimble ionization chambers. P_{wall} is plotted as a function of the beam quality specifier $\%dd(10)_x$ and is shown for a chamber with no waterproofing sleeve. The wall material is indicated in parentheses beside each chamber name. The calculations were performed using CSnrc.

waterproofing sleeve decreases the chamber response by up to 0.30% in photon beams for the chambers considered here. In some cases, this effect is larger than the P_{wall} correction itself and therefore should be included in the P_{wall} calculation. Figure 6.5 shows P_{sleeve} for a 1 mm PMMA waterproofing sleeve as a function of $\%dd(10)_x$, where P_{sleeve} is defined as the ratio of doses to the cavity for a chamber without any waterproofing sleeve to that of a chamber with a 1 mm PMMA sleeve. The sleeve effect is seen to increase with increasing $\%dd(10)_x$ for all of the chambers. While there is no physical basis for using the same sleeve effect for all chambers, based on Fig. 6.5, it is a reasonable approximation to fit a line to the values for all of the chambers. The solid line shows a linear fit to calculated sleeve effects for all of the chambers as a function of the incident beam quality. The value of P_{sleeve} increases from 0.9998 to 1.0027 for $\%dd(10)_x$ values ranging from 58.9% to 83.8%. Computed using the Almond-Svensson formalism, P_{sleeve} is of a similar magnitude, varying from 0.9996 to 1.0033 over the same range of photon beam qualities. These values are non-negligible when compared to the magnitude of P_{wall} for some of the chambers. Figure 6.5 provides a simple method by which the sleeve correction may be estimated for a chamber using a 1 mm PMMA sleeve, which is typical of the waterproofing sleeves normally used. The fit line may be used as a guide for estimating the sleeve correction for a given chamber and is described by:

$$P_{sleeve} = (0.00017)\%dd(10)_x + 0.993. \quad (6.4)$$

The one standard deviation uncertainty on the slope is 0.000012 and on the intercept is 0.0009. The χ^2 per degree of freedom for the calculated values of P_{sleeve} when compared to the fit line is 1.04.

One assumption inherent in the TG-51 formalism for P_{wall} is that the wall correction is independent of the cavity dimensions. Additional calculations using CSnrc

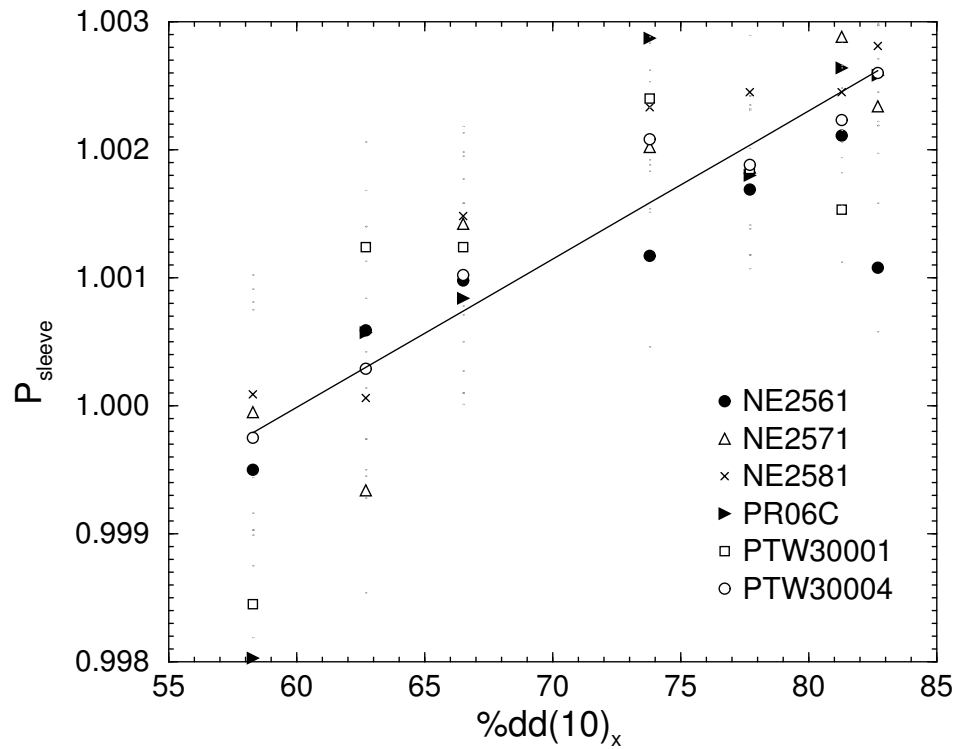


Figure 6.5: The effect of a 1 mm PMMA waterproofing sleeve on the value of P_{wall} for several thimble ionization chambers as a function of $\%dd(10)_x$. The straight line shows a fit to the points from all of the chambers (see Eq. 6.4). The correction P_{sleeve} is defined as the ratio of the dose to cavity for a chamber with no waterproofing sleeve to that for a chamber with a sleeve. All calculations were performed using CSnrc. The uncertainty on the individual points varied from 0.1% at the lowest energy to 0.04% at the highest energy.

are used to verify the validity of this assumption. These calculations are performed for the NE2571 chamber in both a ^{60}Co beam⁴⁵ and a Varian 10 MV beam,⁴⁷ as well as for the NE2581 chamber in a ^{60}Co beam since this chamber shows a much larger P_{wall} correction than does the NE2571. In each case, P_{wall} for the standard chamber dimensions is compared to P_{wall} values computed for four other cavity sizes, varying the length, L , or the radius, r of the cavity. The four other geometries use the following changes to the cavity dimensions: $2L$, $0.67L$, $1.4r$ and $0.6r$. Figure 6.6 shows the effect of the cavity dimensions on P_{wall} for the two chambers. In no case is there any discernable (at the sub-0.1% level) variation in P_{wall} as a function of cavity length. The NE2581 chamber shows on the order of a $\pm 0.2\%$ variation in P_{wall} as a function of the cavity radius.

6.2.2 Comparison to Almond-Svensson formalism

Differences from Almond-Svensson formalism

The previous section provides a set of P_{wall} values computed at 10 cm depth in a water phantom for several thimble ionization chambers and for a range of photon beam qualities. It is instructive to compare these calculated P_{wall} values to the values used in dosimetry protocols. Figure 6.7 shows P_{wall} as a function of beam quality for the NE2571 chamber. The CSnrc values are shown along with the values used by TG-51 and values computed using the Almond-Svensson formalism directly, using quantities calculated using the EGSnrc system. This provides a self-consistent comparison with the CSnrc calculations using a common set of cross-section information for all of the relevant quantities. For this purpose, the stopping power ratios, mass energy absorption coefficients and α values were all computed using the EGSnrc system

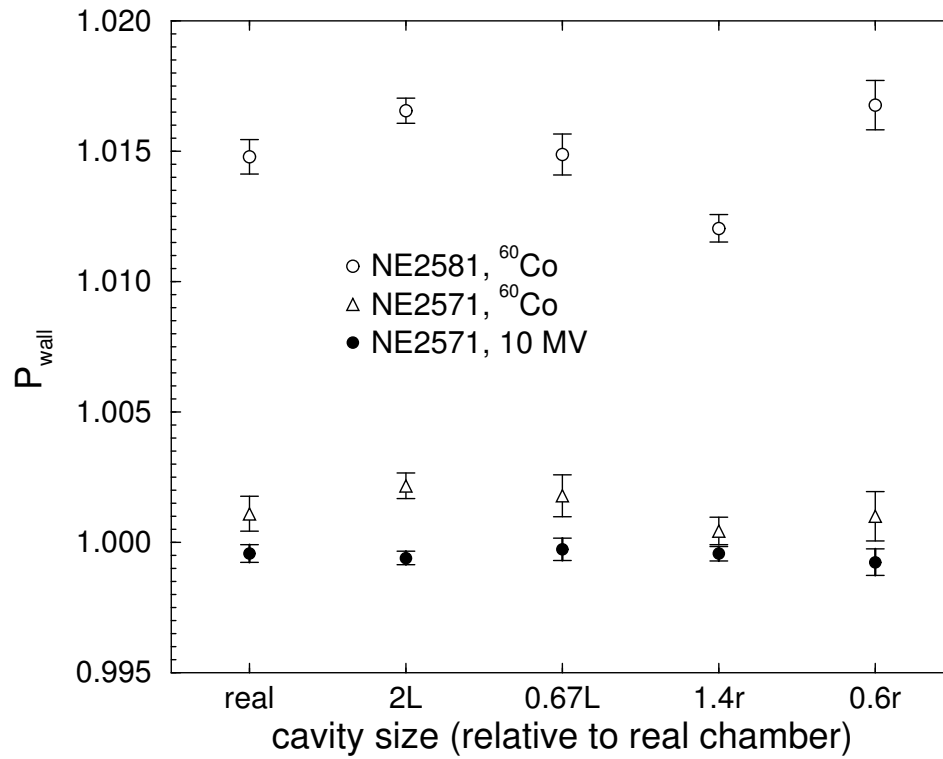


Figure 6.6: Comparison of P_{wall} values for NE2571 and NE2581 chambers to P_{wall} values for these chambers with altered cavity dimensions. The P_{wall} values are plotted against the cavity size, where “real” refers to the actual chamber geometry and the other points indicate changes to either the cavity length, L or radius, r . The calculations are performed using CSnrc.

and were subsequently used to calculate P_{wall} using the Almond-Svensson formula of Eq. 2.5. The stopping power ratios were computed using SPRRZnrc and the mass energy absorption coefficients were computed using the user-code g as described in Chapter 4. The calculation of α will be described in more detail in the next section.

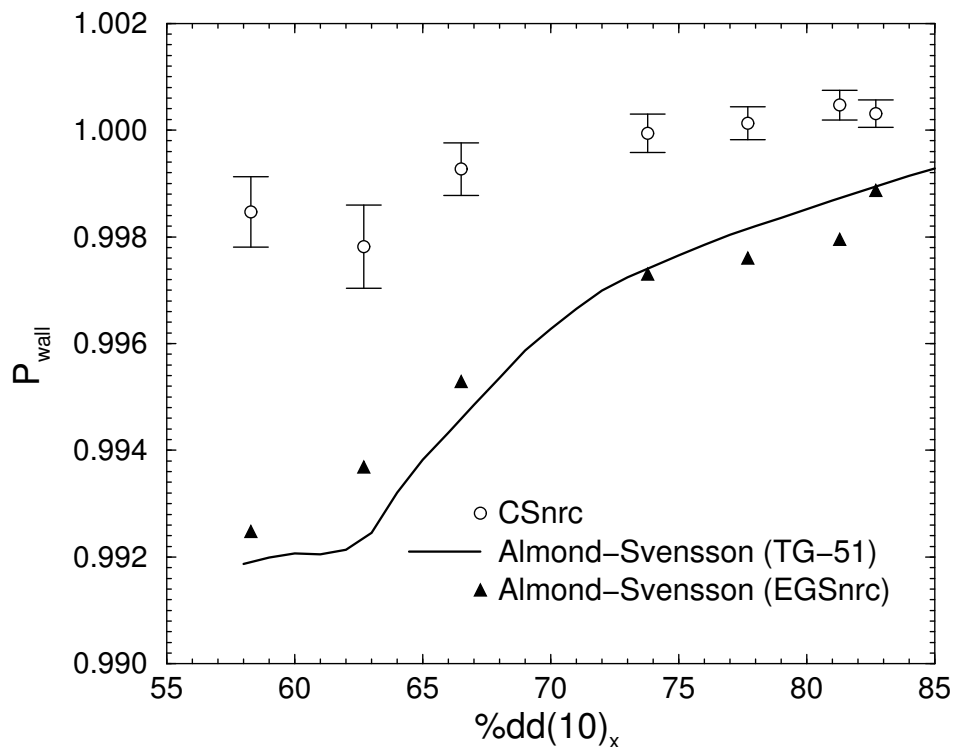


Figure 6.7: A comparison of P_{wall} for an NE2571 chamber calculated using CSnrc to the values of P_{wall} used by the TG-51 protocol. Also shown is P_{wall} computed directly from the Almond-Svensson formula using a self-consistent set of quantities calculated with the EGSnrc system.

Figure 6.7 shows that the CSnrc-calculated values of P_{wall} differ by up to 0.6% from both the values used by TG-51 and from the internally consistent set of P_{wall} values determined using the Almond-Svensson formula. There is little difference between the TG-51 values and the values calculated from the Almond-Svensson equation using EGSnrc-calculated quantities, which indicates a problem with the formalism itself, rather than with the parameters used in its implementation. This plot is typical

of the graphite-walled chambers studied, where CSnrc calculated P_{wall} values differ by up to 0.7% from the Almond-Svensson values for nominal energies below 6 MV. Figure 6.8 shows the ratio of CSnrc values of P_{wall} to the Almond-Svensson values as used in TG-51 for all of the chambers shown in Fig. 6.4. The NE2581 chamber shows differences of up to 0.9% from the Almond-Svensson values at the lower energies, whereas the C-552 chambers agree with the formalism to within 0.3% at all energies.

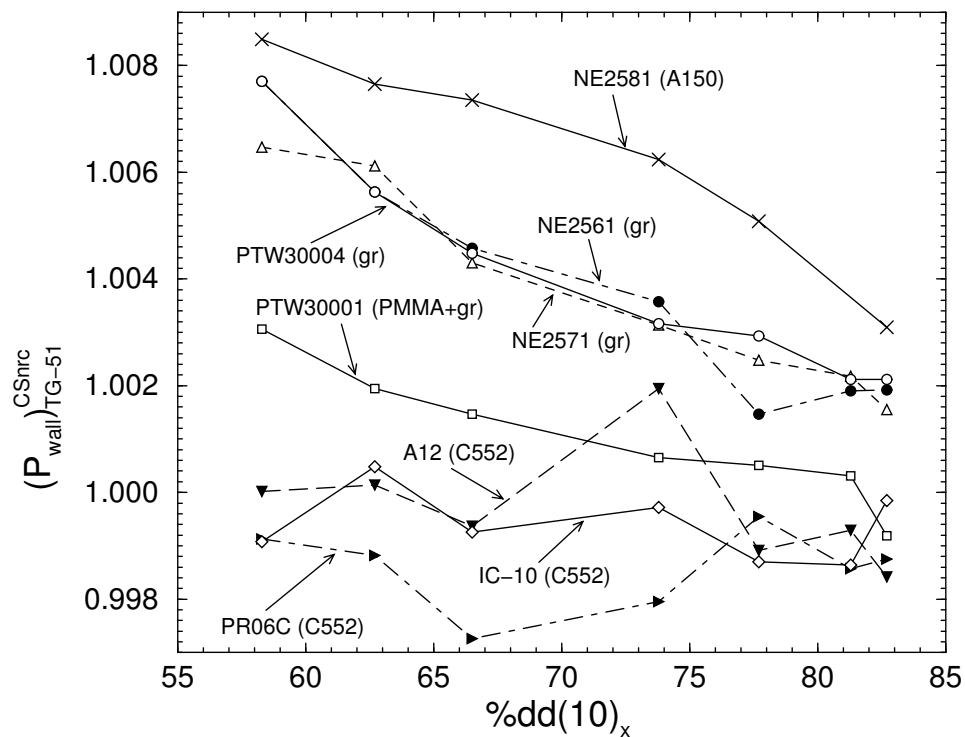


Figure 6.8: The ratio of P_{wall} values calculated using CSnrc to those from the Almond-Svensson formalism. The Almond-Svensson values are computed using Eq. 2.5 where all of the variables were calculated using the EGSnrc system. These values are similar to those used by TG-51 and by the IAEA's TRS-398.

Quantities in the Almond-Svensson formula

The logical place to begin an investigation into the difference between the calculated P_{wall} values and the values used in TG-51 is with the quantities used in the Almond-

Svensson formula. Chapter 4 described some EGSnrc investigations of the stopping power ratios and mass energy absorption coefficients. These quantities were shown to agree with the values used in TG-51 to within 0.1% and 0.4% respectively.

The only remaining variable in the Almond-Svensson formula is the parameter α , describing the fraction of ionizations originating from electrons generated in the chamber wall. Using the user-code CAVRZnrc, α can be computed and compared with the values used by TG-51. For an in-air chamber of wall thickness t , α is given by the ratio of the dose to the air in the chamber to the dose to the air in a chamber with full build-up. Figure 6.9 shows the values of α calculated using CAVRZnrc in comparison with the values given by the AAPM TG-21 protocol⁶ and by the IAEA TRS-277 code of practice,⁸ which are the same values used by the current protocols, TG-51⁷ and TRS-398.⁹ The points from the TG-21 and TRS-277 curves were obtained from Figures 1 and 15 in the respective reports, both of which base their data on the work of Lempert et. al.⁹⁹

Figure 6.9 shows significant discrepancies, for some wall thicknesses, between values of α from the different sources. For wall thicknesses between 50 mg/cm² and 150 mg/cm², there are differences between the CAVRZnrc values and the TG-21 and TRS-398 values of up to 18% and 10%, respectively. However, these result in much smaller discrepancies in P_{wall} when used in the Almond-Svensson formalism. If we consider a commonly used chamber, such as the NE2571 chamber used in water, P_{wall} values computed using the three sources of α values discussed here, agree to within 0.17% in all cases.

In dosimetry protocols, the value of α is treated as being independent of the chamber wall composition, provided the wall is made from low atomic number materials. Fig. 6.9 shows calculated values of α for both graphite and aluminum walls.

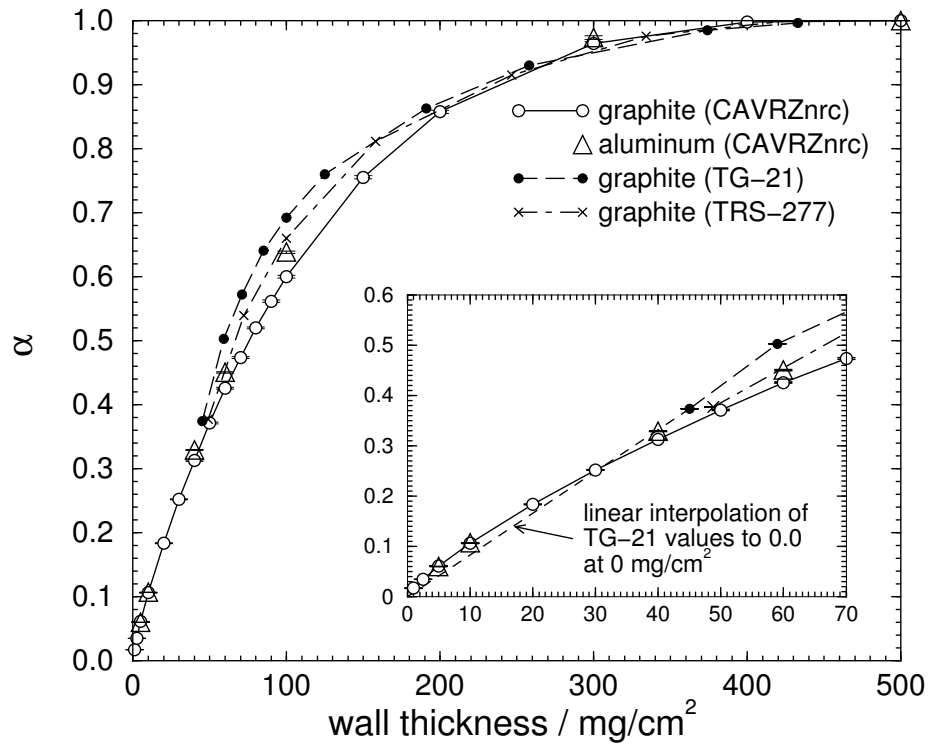


Figure 6.9: Values of α used in the Almond-Svensson formalism as a function of graphite wall thickness. The open circles show values calculated using CAVRZnrc as described in the text. These are compared to the values from the TG-21 protocol (solid circles) and the TRS-277 code of practice (crosses). Also shown are CAVRZnrc values for an aluminum wall.

Since aluminum is an extreme case and differs significantly from graphite in atomic number, the agreement between the graphite and aluminum values justifies the use of material-independent α values for low atomic number materials and therefore this will not affect the P_{wall} calculations for the non-graphite-walled chambers studied here.

Figure 6.9 also shows in greater detail the α values for very thin wall thicknesses. This region is relevant for chamber construction that uses a thin conducting layer on the inner surface of a non-conducting wall such as the PTW30001 studied here. Neither the TG-21 nor the TRS-277 protocol gives α values for chamber-wall thicknesses below 45 mg/cm². In the case of such thin layers, it is common for dosimetry calculations to assume a linear interpolation to $\alpha = 0$ at a wall thickness of 0 mg/cm².¹⁰⁰ The inset in Fig. 6.9 shows the region for wall thicknesses below 70 mg/cm² and indicates the linear interpolation of the AAPM values to $\alpha = 0$ at 0 mg/cm². In the region of the linear interpolation, interpolated values of α differ by as much as 22% from the calculated values, however the potential effect on P_{wall} when used in the Almond-Svensson formula is less than 0.08%.

Based upon the CSnrc calculations of the individual parameters in the Almond-Svensson equation, there are no discrepancies that account for the differences in P_{wall} observed between the CSnrc calculations and the formalism. This is to be expected from Fig. 6.7 since there is little difference between the values used by TG-51 and the values determined using the Almond-Svensson formula with the EGSnrc-calculated quantities. Since the differences in P_{wall} cannot be explained by differences in the parameters used in the formalism, this indicates a problem with the formalism itself.

6.3 P_{wall} values in electron beams

In electron beams, in both the TG-51 protocol and the IAEA code of practice, P_{wall} is assumed to be unity for all chambers. CSnrc is used to compute P_{wall} in high-energy electron beams, using the electron beam input spectra from Ding and Rogers⁴⁸ detailed in Table 1.3. For all calculations, the chamber is placed at the reference depth of $0.6R_{50} - 0.1$ cm in a water phantom. Figure 6.10 shows P_{wall} versus beam quality for an NE2571 both with and without a 1 mm PMMA waterproofing sleeve. The scatter of points seen in Fig. 6.10, as well as the overall behaviour of the values as a function of R_{50} is typical of the other chambers. That is, for all chambers studied here, P_{wall} decreases as a function of R_{50} . Furthermore, for all of the chambers, the P_{wall} values for the beams from the Therac machine are systematically lower than the neighbouring values. The Therac beams are swept beams and are therefore nearly monoenergetic compared to the beams from the other, scattering foil accelerators. Calculations of P_{wall} for monoenergetic electron beams show a smooth curve with P_{wall} decreasing monotonically with R_{50} and do not exhibit the scatter in P_{wall} values seen when using clinical electron beams. This suggests that R_{50} is not an adequate beam quality specifier for P_{wall} in electron beams, and that the value of P_{wall} depends on the specifics of the accelerator.

Due to the scatter present in Fig. 6.10 and common to all of the chambers used in the calculations, it is difficult to present all of the P_{wall} information in a single plot as was the case in Fig. 6.4 for the photon beams. For this reason, in order to present a complete set of P_{wall} values for the cylindrical chambers in electron beams, Fig. 6.11 presents linear fits to the calculated P_{wall} values as a function of R_{50} . The linear fit is performed for calculated values at 11 beam qualities, ranging in nominal energy

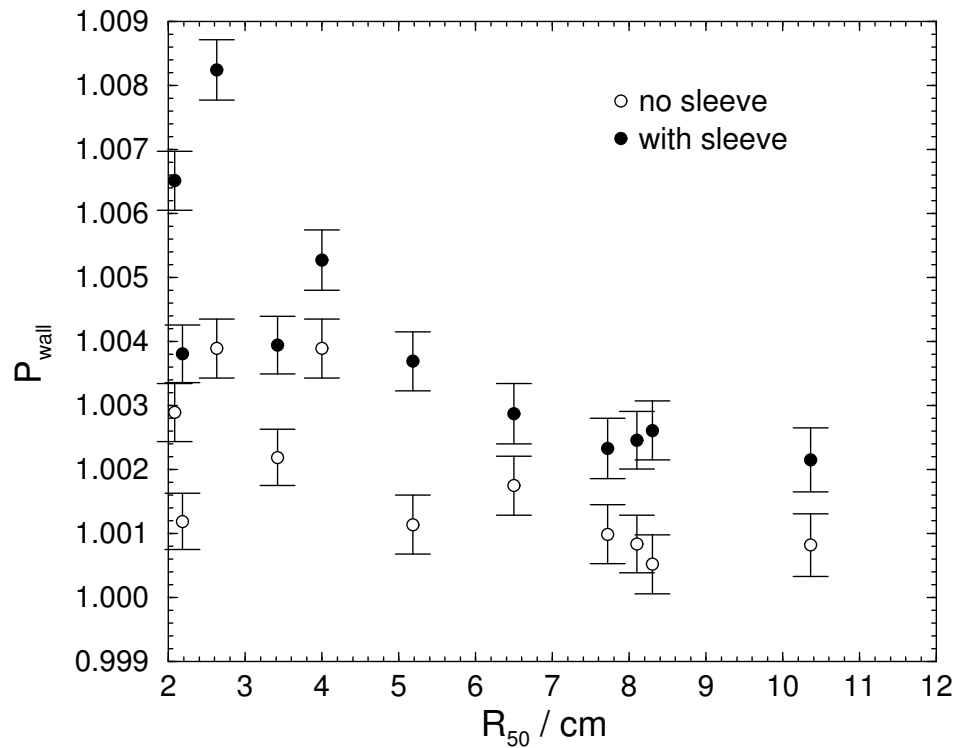


Figure 6.10: Calculated values of P_{wall} for an NE2571 chamber in high-energy electron beams. The values are calculated using CSnrc with the chamber placed at a depth of d_{ref} , as specified by the TG-51 protocol. P_{wall} is shown for a bare chamber in a water phantom and for a chamber with a 1 mm PMMA waterproofing sleeve.

from 5 MeV to 25 MeV. The scatter of points about the fit lines, was highest at the lower energies and was typically on the order of $\pm 0.15\%$. For completeness, P_{wall} is shown for beam qualities, R_{50} , between 2.18 cm and 10.36 cm, however TG-51 does not recommend the use of thimble chambers for $R_{50} < 4$ cm. For the chambers with a C-552 wall, P_{wall} is less than 0.2% for all electron energies. For the other chambers, P_{wall} is as high as 0.6% and is significant even for higher R_{50} .

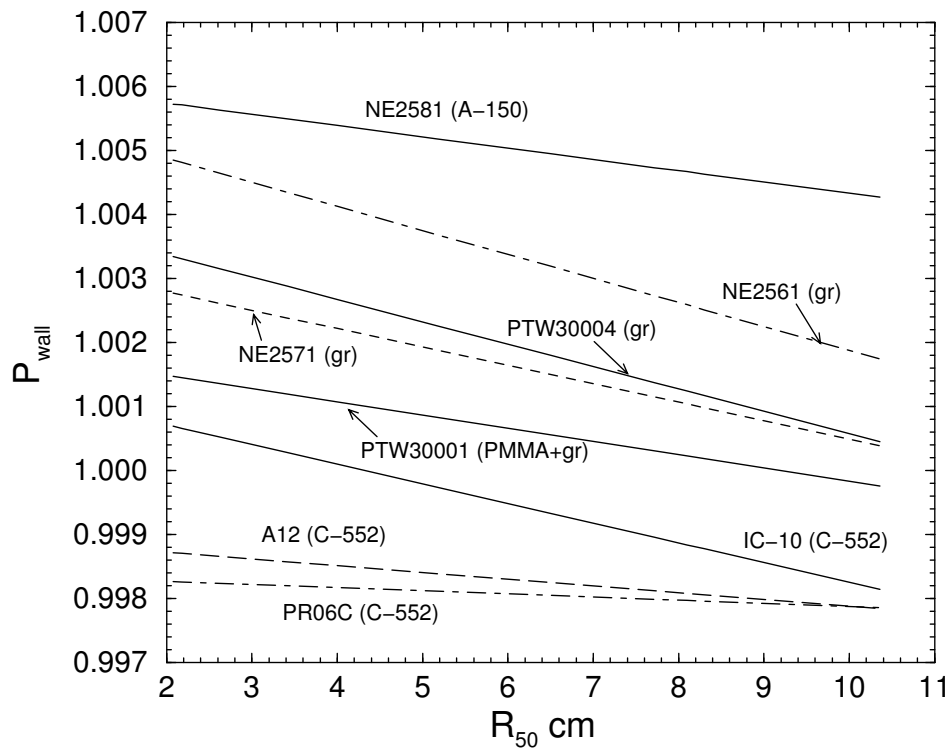


Figure 6.11: Straight line fits to calculated values of P_{wall} for cylindrical chambers in high-energy electron beams. Calculations are performed using CSnrc with the chamber placed at a depth of d_{ref} in water as specified by TG-51, with no waterproofing sleeve. The TG-51 protocol assumes a P_{wall} of unity at all electron energies.

As in the case of photons, P_{wall} in Fig. 6.11 is shown for the chambers without including the effect of a waterproofing sleeve. Figure 6.12 shows the sleeve correction, P_{sleeve} , for thimble chambers in electron beams. The sleeve correction was calculated using CSnrc for a 1 mm PMMA sleeve surrounding the chamber wall. The solid line

is a linear fit to the values for all of the chambers. The χ^2 per degree of freedom for the P_{sleeve} values compared to the fit line is 1.08. In electron beams, the sleeve effect varies from 0.3% at $R_{50} = 2.18$ cm to less than 0.1% for $R_{50} > 10$ cm. As in the photon case, this sleeve correction is in some cases greater than the P_{wall} correction itself and therefore should not be ignored for precise work. The linear fit in Figure 6.12 provides a simple equation for determining the sleeve effect as a function of electron beam quality for a 1 mm PMMA waterproofing sleeve:

$$P_{sleeve} = (-0.026)R_{50} + 0.35. \quad (6.5)$$

The one standard deviation uncertainty in the slope is 0.003 and on the intercept is 0.02.

In electron beams, ion chamber measurements are very sensitive to the depth of measurement. In the most recent set of protocols, a new reference depth was adopted, defined by Eq. 2.8. CSnrc is used to investigate the sensitivity of P_{wall} to the depth of measurement. All of the calculations described earlier in this section were carried out at the reference depth specified by the TG-51 protocol. Further calculations were performed by varying the depth of the chamber within the water phantom. Figure 6.13 shows P_{wall} as a function of the depth of measurement for an NE2571 chamber in both a 6 MeV ($R_{50} = 2.63$ cm) and a 20 MeV ($R_{50} = 8.10$ cm) beam. In the case of the 20 MeV beam, there is a 1% variation in P_{wall} when going from a depth of 2 cm to a depth of nearly R_{50} . Near $d_{ref} = 4.76$ cm, the variation with depth is not dramatic and therefore incorrect placement of the chamber would not result in a large error in P_{wall} . In the case of the 6 MeV beam, there is a 2.5% variation in P_{wall} going from a depth of 0.5 cm to R_{50} . Near the reference depth of 1.48 cm, the gradient is steep and therefore positioning is much more crucial for the lower-energy beam.

6.3. P_{WALL} VALUES IN ELECTRON BEAMS

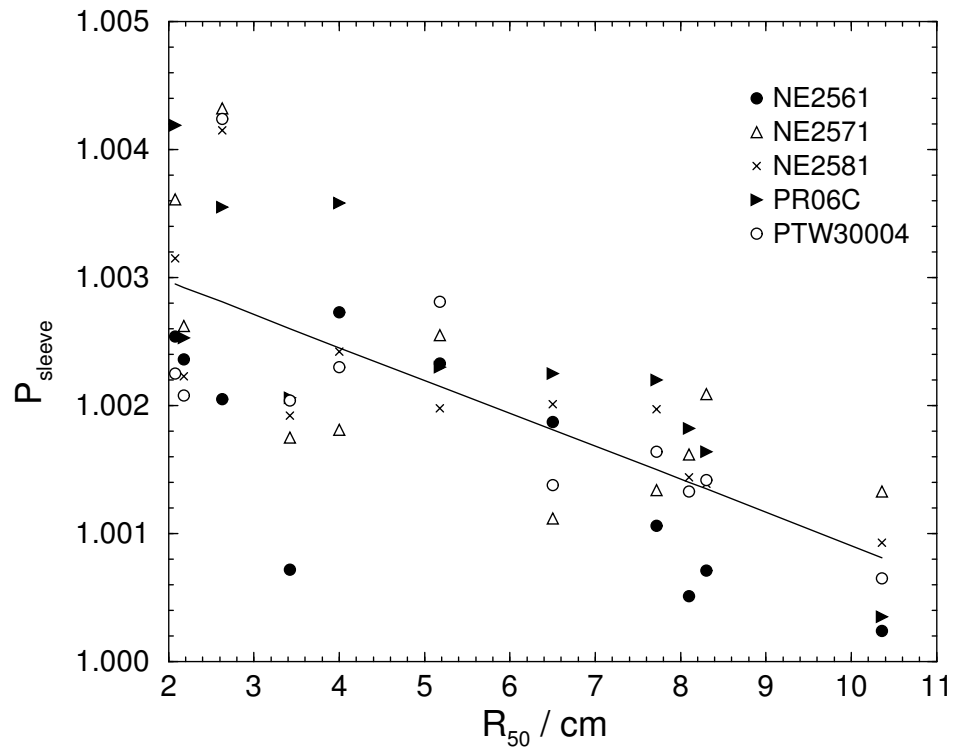


Figure 6.12: The sleeve correction factor P_{sleeve} for a 1 mm PMMA sleeve as a function of the beam quality specifier, R_{50} . The solid line shows a linear fit to the sleeve corrections for all of the cylindrical chambers discussed in the text (see Eq. 6.5). All points are calculated at a depth of d_{ref} in water, as specified by the TG-51 protocol.

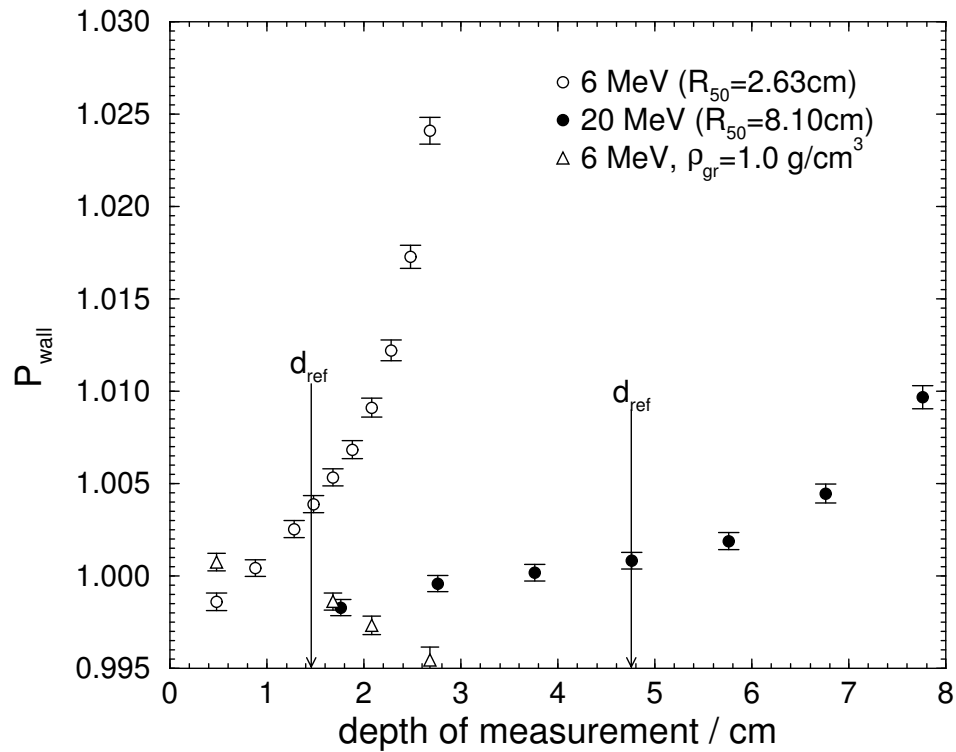


Figure 6.13: P_{wall} as a function of depth of measurement for an NE2571 chamber in a 6 MeV ($R_{50} = 2.63$ cm) and a 20 MeV ($R_{50} = 8.10$ cm) beam. The open triangles show P_{wall} in a 6 MeV for a chamber with the graphite wall density set to unity. The arrows indicate the reference depths for the two beams.

The variation in P_{wall} with depth can be explained in part by the difference in density between the graphite wall and the surrounding water. Using the PEGS4 code described in Chapter 1, it is possible to artificially change the density of a material when generating the material data for a simulation. If the P_{wall} calculations are repeated using a graphite wall, but forcing the density of the wall to be equal to that of water, the wall correction is much smaller than before and shows less variation with depth over the range of depths up to R_{50} . This is shown for the 6 MeV beam by the open triangles in Fig. 6.13. This suggests that the P_{wall} correction can be highly dependent on the material density. However, the material density alone cannot be used to determine P_{wall} . If the density were the only factor contributing to the wall correction, it would be possible to treat the graphite wall in the NE2571 chamber as shifting the effective depth of the chamber by 0.25 mm compared to a unit density wall. If this were the case, the ratio of doses at two points on the depth-dose curve separated by a depth of 0.25 mm should correspond to P_{wall} for the real chamber at that depth. Examination of this possibility using the depth-dose curve for the 6 MeV beam from Ding and Rogers⁴⁸ does not show this correspondence between points on the depth-dose curve and P_{wall} . Nor do we see a constant value of P_{wall} on the more or less linear part of the dose fall-off region of the depth-dose curve near R_{50} . This indicates that while the density contributes to the wall correction, P_{wall} is also material dependent.

Furthermore, while Fig. 6.13 shows that density has a significant effect on P_{wall} , the degree to which the density contributes to P_{wall} is also material dependent. For graphite, by correcting the density of graphite to that of water, one decreases the P_{wall} correction, and at the reference depth for unit density, there is nearly no wall correction. A similar investigation using a PR06C chamber shows that this is not

the case for a C-552 wall. Figure 6.14 shows P_{wall} as a function of material density for both the NE2571 chamber (graphite) and the PR06C chamber (C-552). The chambers were placed at the reference depth in a 6 MeV beam and the density of the wall material was varied. Figure 6.14 shows that in both cases, P_{wall} is affected by the density of the material. However, while a unit density for graphite nearly removes the entire wall correction, this is not the case for the C-552 wall. Figures 6.13 and 6.14 show that the density contributes to the overall wall correction and should therefore be included in any formalism aimed at determining P_{wall} . The dependence on density may indicate that the dense walls are simply stopping more electrons, an effect which increases dramatically when the average energy becomes low, thereby explaining the large variation in P_{wall} with depth.

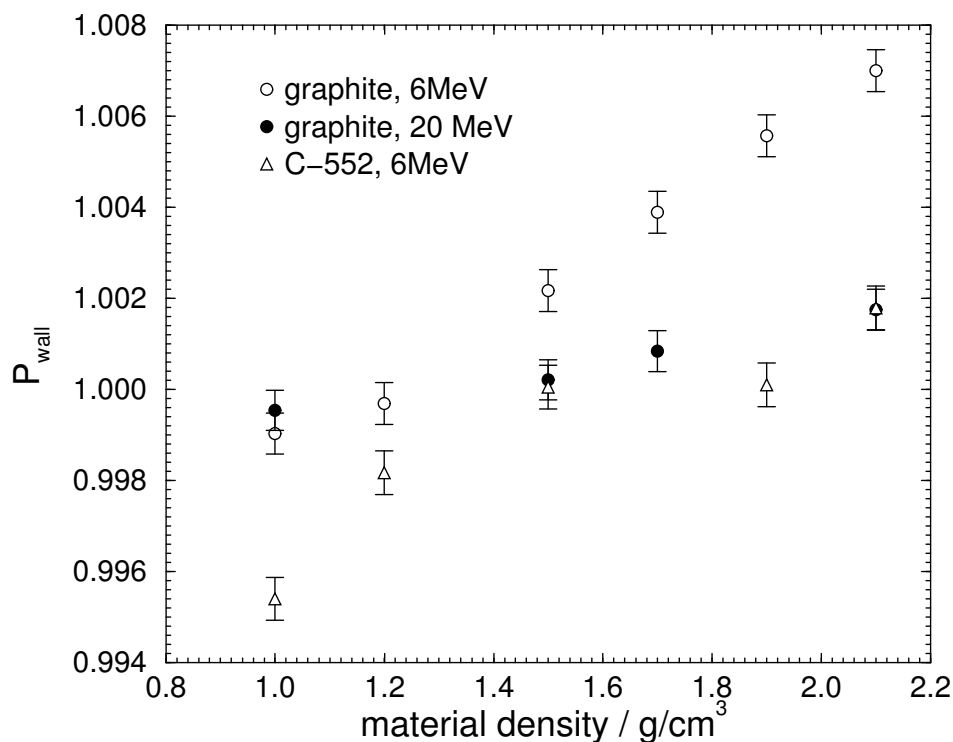


Figure 6.14: P_{wall} as a function of wall material density for an NE2571 chamber and a PR06C chamber in a 6 MeV electron beam. The chambers were placed at the reference depth in water and the density of the graphite or C-552 walls was varied.

6.4 Summary

This chapter presents a new set of P_{wall} values for thimble ionisation chambers in high-energy photon and electron beams. Examples are shown for which the CSnrc values of P_{wall} in photon beams agree much better with previously published experimental results than do the values used by the TG-51 protocol. A complete set of P_{wall} values for several ion chambers in photon beams is presented and is shown to differ from the TG-51 values by up to 0.8%. The sleeve correction, which is currently ignored by the TG-51 protocol, is also calculated using CSnrc and is shown to be as high as 0.3%. The CSnrc results point to problems with the standard P_{wall} formalism and for precise work, the new values should be used. In electron beams, the CSnrc values represent the first full set of published P_{wall} values for thimble chambers in electron beams. These show corrections of up to 0.6% and sleeve corrections of up to 0.3%. They also show a very strong dependence on the depth of measurement which can be in large part explained by the difference in density between the chamber wall and the surrounding phantom medium. The P_{wall} values presented here provide a set of P_{wall} values that can be used to explain discrepancies between experiments and the standard formalism and can be incorporated into future protocols. Many of these old experiments will need to be re-analyzed since they used incorrect P_{wall} values.

Chapter 7

P_{wall} for parallel-plate ion chambers

Chapter 6 describes problems with the current values of the wall correction factor P_{wall} for thimble ionization chambers. It discusses calculations of P_{wall} using the CSnrc code for the EGSnrc system. In the present chapter, similar investigations of the wall correction will be described for parallel-plate chambers.

As with the cylindrical chambers, experimental determinations of P_{wall} for parallel-plate chambers are difficult due to the high precision required for the measurements. Furthermore, unlike cylindrical chambers, where the wall is homogeneous or nearly homogeneous, parallel-plate chambers are typically constructed such that the chamber walls are composed of several materials, making any simple experimental extrapolation to zero wall thickness difficult. Monte Carlo calculations of P_{wall} are also difficult due to the small magnitude of the wall correction itself which requires very low statistical uncertainties in order to be significant. The calculations typically require hundreds of millions of particle histories in order to achieve the nec-

essary uncertainties, and the computation times can be very long. This is even more pronounced in the case of parallel-plate chambers than it is for cylindrical chambers since the parallel-plate chambers typically have many more geometrical regions and slow the calculations even further. There is little published data regarding the wall correction for parallel-plate chambers in photon beams,^{73,101} and the data for electron beams is inconclusive. Despite some evidence suggesting a non-unity wall correction in electron beams,^{92,94,95} current dosimetry protocols assign a value of unity to P_{wall} for parallel-plate chambers in electron beams.

7.1 Evidence for a non-unity wall correction

Interest in revisiting the correction factors for parallel plate chambers is based upon a number of experiments that have shown significant corrections in electron beams, caused primarily by the backscatter from the chamber body behind the air cavity. Hunt et. al.⁹⁴ measured the effect of electron backscatter from materials placed behind the air cavity volume. They measured the effect of electron backscattering as a function of effective atomic number, thickness of the material and diameter of the backscattering disc. They concluded that most parallel-plate chambers would show a 1-2% effect due to electron backscatter at low electron energies.

A later study by Klevenhagen⁹⁵ examined the variation of the electron backscatter as a function of an effective atomic number in electron beams and proposed an empirical formula to describe this variation. This formula was derived from a fit to measurements using high-Z materials and not the low-Z materials commonly used in chambers for electron beam dosimetry.

Nilsson et. al.⁹² performed a series of measurements aimed at determining the

wall correction factor due to electron backscatter in electron beams. They used a specially designed parallel-plate ion chamber that minimized any perturbation from in-scatter from the side walls, thereby isolating the effects due to the front and back walls only. This chamber allowed them to change the materials on the front and back as well as the cavity size and therefore they could mimic geometries of commonly used parallel-plate chambers. They also compared their experimental results to Monte Carlo calculations performed using the EGS4 system.²⁷ They found that in many chamber designs there was an energy dependent wall correction factor, on the order of 2% at low electron energies. It should be noted that there are known problems with EGS4 for the simulation of electron backscatter and that this is much improved in EGSnrc.

A Monte Carlo study by Ma and Rogers⁹¹ using the EGS4 system also showed non-unity values of P_{wall} for both the NACP and Markus chambers in electron beams. Their calculations showed corrections of over 2% for the Markus chamber and corrections of up to 1.5% for the NACP chamber. They used mono-energetic electron beams and the chambers were simulated at a depth of dose maximum in a water phantom. Their calculations also showed that P_{wall} increased slightly with increasing depth in water.

Williams et. al.¹⁰² used the EGS4 system to study perturbation factors for the NACP-02 parallel-plate chamber. They calculated an energy-dependent wall correction factor as high as 1.2% for a 4 MeV nominal energy electron beam. The uncertainty on their wall correction factors was between 0.21% and 0.47%.

More recently, Sempau et. al.¹⁰³ used the Monte Carlo code PENELOPE^{31,32} to study an overall perturbation factor for an NACP chamber in high-energy electron beams. Rather than determine the individual correction factors independently, they

used a Monte Carlo calculation to compute the total perturbation factor required to convert from dose to the cavity to dose to water at the point of interest. This was performed for an NACP chamber and compared to the equivalent values from the TRS-398 code of practice. They showed that as a function of beam quality, their calculated values show similar behaviour to the perturbation corrections predicted by the TRS-398 code of practice. Upon normalization to the TRS-398 values, their results showed only minor differences at the lower electron energies. However, their paper does not indicate the magnitude of the factor by which the Monte Carlo values were scaled in order to coincide with the TRS-398 values for one high-energy beam. Furthermore, while an overall perturbation factor is fundamentally equivalent to the combined effect of the correction factors used in dosimetry, it remains the case that major dosimetry protocols distinguish between the various correction factors for ion chambers.

In photon beams, Wittkämper et. al.¹⁰¹ measured P_{wall} values in high-energy photon beams for the NACP and Markus chambers. They used beams with nominal energies ranging from ^{60}Co to 24 MV. For the NACP chamber, they measured a P_{wall} correction of 1.013 in a ^{60}Co beam and for the Markus chamber found a P_{wall} value of 1.004 for the same beam. For both chambers, P_{wall} varied by up to 0.4% over the range of photon beams used in their experiment. The uncertainty on their measured P_{wall} values was on the order of $\pm 0.5\%$.

In a more recent study, Mainegra et. al.⁷³ used the EGSnrc code to calculate P_{wall} values for parallel-plate chambers in a ^{60}Co beam. They too showed non-unity P_{wall} values for these chambers. They calculated P_{wall} values of 1.0207, 1.0048 and 1.0090 for the NACP, Markus and Roos chambers respectively. Their results had statistical uncertainties of less than 0.06%. Their values agree well with other reported

7.1. EVIDENCE FOR A NON-UNITY WALL CORRECTION

P_{wall} values for these chambers in ^{60}Co beams.^{104, 105}

7.2 P_{wall} values in electron beams

7.2.1 P_{wall} for several commonly used ion chambers

CSnrc is used to investigate the wall correction factor for several parallel-plate chambers in high-energy electron beams. The chambers considered in this investigation are described in Table 1.5. The simulation geometry used to calculate P_{wall} is similar to the geometry described in Chapter 6, where only the chamber wall and cavity are included in the geometry. For parallel-plate chambers, where the wall is often composed of several regions and many different materials, the dose to the cavity for the real wall is compared to a chamber for which the entire wall is modeled as water. For all of the calculations, the front face of the air cavity is placed at the reference depth in water, as defined by Eq. 2.8. The definition of the reference depth used by the TG-51 protocol does not account for changes in the effective depth of the chamber due to higher density walls whereas the TRS-398 code of practice defines the reference depth in terms of g/cm^2 of water and therefore the thickness and material of the front wall must be used to determine an equivalent thickness of water for the front wall. For the chambers studied here, the largest deviation between the reference depth and the effective depth in water is on the order of 1 mm, which does not lead to a significant change in P_{wall} . The effective of shifting the effective depth of the chamber on the value of P_{wall} will depend on the depth of measurement and on the dose gradient at this point. All of the present calculations are performed using the TG-51 convention of defining the reference depth in terms of centimetres and do not shift the reference

depth to an equivalent depth in water.

Figure 7.1 shows P_{wall} as a function of R_{50} for the NACP chamber. The scatter in the values is typical of all of the chambers studied in the present work. As in the case of the cylindrical chambers in Chapter 6, the P_{wall} values from the Therac spectra are systematically lower than the neighbouring values, indicating that P_{wall} in electron beams is affected by the beam filtration and is not well-specified by R_{50} . The CSnrc results show that P_{wall} for the NACP chamber varies from 1.017 near $R_{50} = 2.1$ cm to 1.008 near $R_{50} = 8.3$ cm. This size of P_{wall} correction is similar to those determined by Hunt et. al.⁹⁴ and by Nilsson et. al.,⁹² and described in a previous section. The variation in P_{wall} over the range of R_{50} values considered is slightly greater than in a previous Monte Carlo study, which has considerably poorer statistics, conducted using the EGS4 system. In that case, Williams et. al.¹⁰² found that over a range of nominal energies from 4 MeV to 19 MeV, P_{wall} changed from $1.0127 \pm 0.21\%$ to $1.0065 \pm 0.47\%$. The present values of P_{wall} are about 0.5% larger at low energies. The nominal energies in Fig. 7.1 range from 5 MeV to 21 MeV and all values are calculated at the reference depth in water.

The other parallel-plate chambers studied here show similar trends in the P_{wall} values as a function of R_{50} in that they all show a decrease in P_{wall} with increasing R_{50} . Figure 7.2 shows P_{wall} values for each of the chambers included in this study. The straight lines are fit lines to the CSnrc-calculated P_{wall} values for each chamber. All chambers show a P_{wall} correction on the order or 1% or larger for the lower energy beams. In all cases, this correction decreases as a function of R_{50} and varies by 1% or more over a range of nominal energies from 5 MeV to 25 MeV.

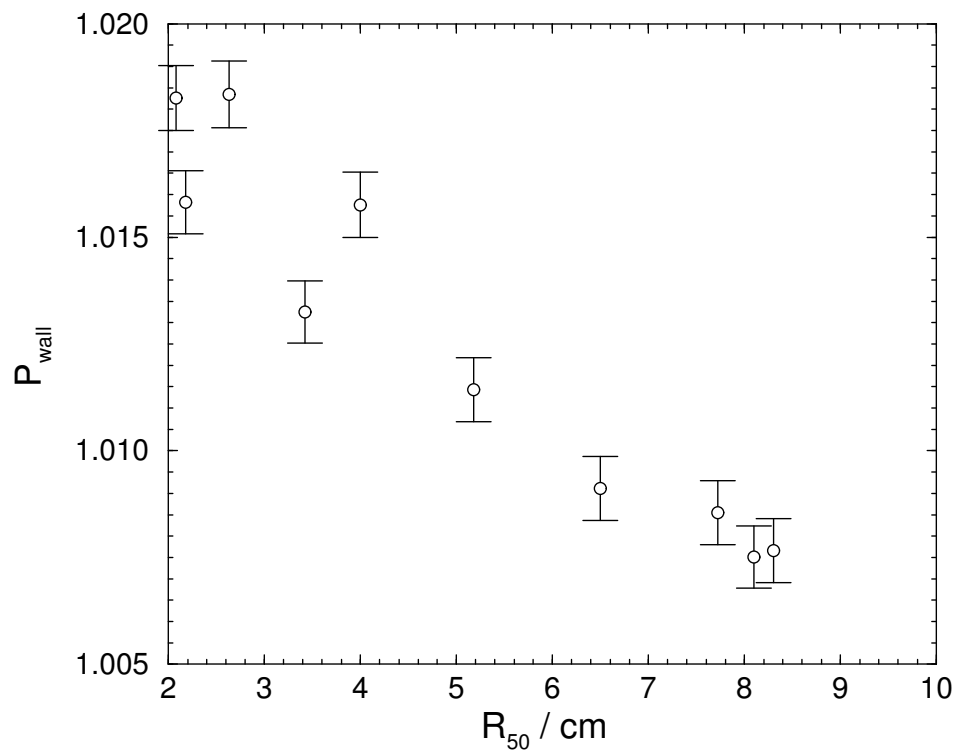


Figure 7.1: The wall correction factor P_{wall} as a function of R_{50} for an NACP chamber in high-energy electron beams. The values are calculated using CSnrc with the chamber placed at a depth of d_{ref} in a water phantom.

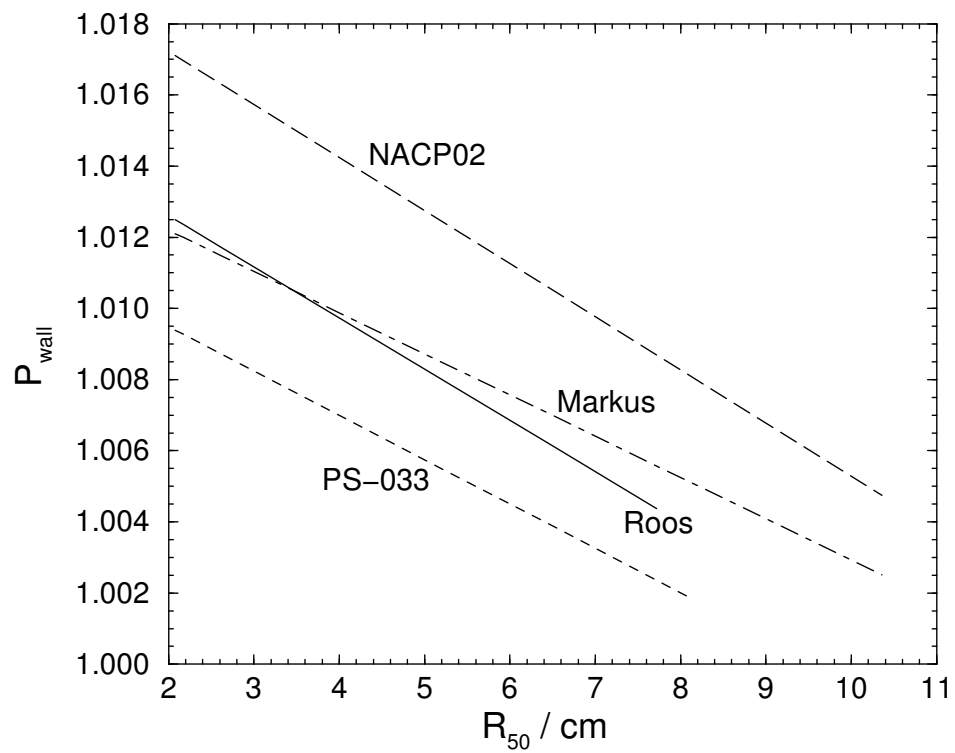


Figure 7.2: Linear fits to calculated P_{wall} values for several parallel-plate chambers in high-energy electron beams. The calculations are performed using CSnrc and by placing the chamber at a depth of d_{ref} in a water phantom.

7.2.2 P_{wall} as a function of depth of measurement

In electron beams, ion chamber measurements are very sensitive to the depth of measurement within the water phantom. CSnrc is used to investigate the sensitivity of P_{wall} to the depth of measurement. The calculations are performed for an NACP chamber in both a 6 MeV and a 20 MeV beam and the depths are varied from much less than d_{ref} to a depth of nearly R_{50} for each beam. Figure 7.3 shows that for the 6 MeV beam there is a striking variation of P_{wall} with depth. For this beam, there is a 5% variation in P_{wall} between d_{ref} and R_{50} . For the 20 MeV beam, this variation is less, at 2.3%. Although the values of P_{wall} in Fig. 7.3 are slightly higher than previously calculated values of P_{wall} by Ma and Rogers,⁹¹ they show the same trend of increasing with increasing depth. The calculations by Ma and Rogers used mono-energetic electron beams and did not cover the range of depths included here.

The magnitude of the variation in P_{wall} with depth is somewhat surprising given that such a drastic departure from standard dosimetry theory has not been seen in practice. If one compares the stopping power ratio at depth to the ratio of the dose to water to the dose to the air in the chamber cavity, standard dosimetry formalism suggests that these quantities have the same value since the correction factors in Eq. 2.4 (page 23) are taken to be unity for the NACP chamber. However, as shown in Figure 7.4 for a 6 MeV beam, when calculated using EGSnrc the stopping power curve and the ratio of doses diverge as the depth is increased. If the current P_{wall} values are used as a correction to the standard dosimetry theory, the product $\left(\frac{\bar{L}}{\rho}\right)_{air}^{water} P_{wall}$ shows better agreement with the dose ratios.

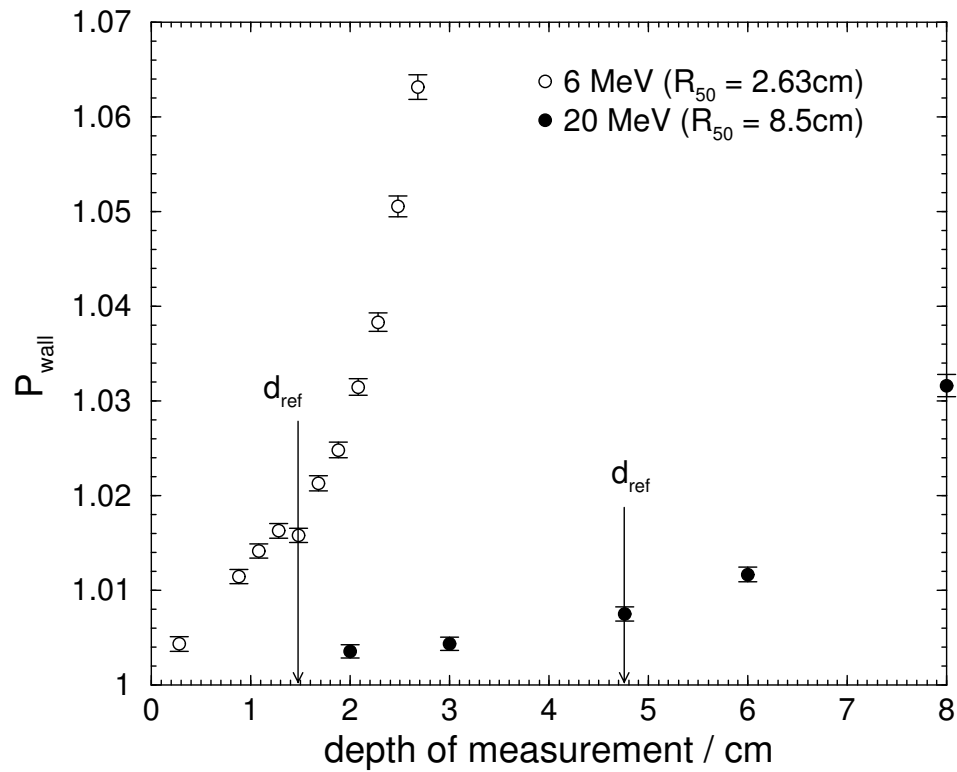


Figure 7.3: P_{wall} as a function of depth of measurement for an NACP chamber in a water phantom. The calculations were performed using the CSnrc user-code for nominal beam energies of 6 MeV and 20 MeV. The reference depths for each beam, d_{ref} , specified by the standard dosimetry protocols, are indicated by the arrows.

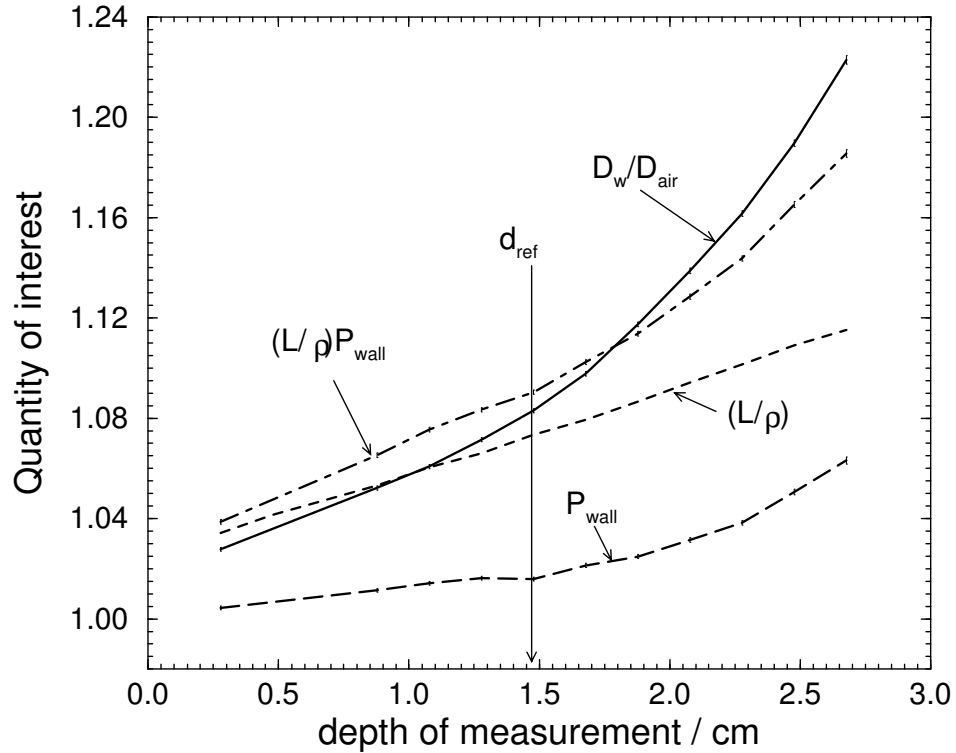


Figure 7.4: Several of the factors involved in the dosimetry formalism employed in TG-51 as a function of depth of measurement in a Varian 6 MeV electron beam. For an NACP chamber in electron beams, the formalism used by the protocol predicts that the ratio of doses, D_w/D_{air} should equal the stopping power ratio of water to air. Here, D_w is the dose to a small region at the point of measurement of the chamber in a homogeneous water geometry and D_{air} is the dose to the air in the chamber. Also shown is the variation in P_{wall} calculated using CSnrc. The product $\left(\frac{\bar{L}}{\rho}\right)_{air}^{water} P_{wall}$ shows better agreement with the dose ratios than the simple stopping power ratio, suggesting a non-unity correction factor for the NACP chamber.

7.2.3 Comparison to perturbation correction calculations

In the recent study by Sempau et. al.,¹⁰³ they calculated an overall correction factor for the NACP chamber. This overall correction is given in Eq. 2.4 (page 23) as the product of the correction factors P_{cel} , P_{wall} and P_{repl} and the restricted stopping power ratio. The product of the P_i corrections is taken to be unity for the NACP chamber in both TRS-398 and TG-51 and therefore each of these protocols predict that the dose ratio should be equal to the stopping-power ratio for the NACP chamber. In order to calculate an overall correction factor, Sempau et. al. computed the ratio of the dose to water at the point of measurement of an NACP chamber for a geometry composed entirely of water to the dose to air for a realistic NACP chamber at depth in a water phantom. Their results were presented as an overall chamber correction factor, as a function of beam quality. They concluded that there was no significant discrepancy between their calculations and the predictions of the TRS-398 code of practice, except for some small deviations at lower electron energies.

The present results from CSnrc for P_{wall} values in electron beams are seemingly in conflict with the results of Sempau et. al. since the present results show a non-unity P_{wall} factor for the NACP chamber. In some cases, the calculated P_{wall} value is as high as 2%. This magnitude of correction was not indicated in the study by Sempau et. al. The difficulty in comparing the two sets of calculations is that the results of Sempau et. al. were normalized by an unspecified amount in order to give agreement at $R_{50} = 8.75$ cm with the TRS-398 values. Furthermore, it is possible that the replacement correction, P_{repl} may offset the P_{wall} correction, leading to a smaller overall change compared to the standard theory than the individual P_{wall} values indicate.

In order to investigate the issue of the normalization of the Sempau et. al. results, CSnrc is used to repeat the calculations of the overall correction factor. For these calculations, the NACP chamber is placed at the reference depth in water for each electron beam used. In order to calculate the dose to water at the point of measurement of the chamber, a thin 0.1 mm thick slab was placed at the front face of the cavity region and the dose was scored to this thin slab. This was computed in a separate calculation from the P_{wall} calculations, since CSnrc cannot currently handle changes to the size of the cavity from one geometry option to the next. The ratio of the dose to water to the dose to air is calculated at each beam quality and is presented in Figure 7.5. The CSnrc results are shown alongside the TRS-398 predictions and the normalized results of Sempau et. al. In their paper, Sempau et. al. normalized the values to the TRS-398 value at $R_{50} = 8.75$ cm. For the present study, the CSnrc calculated values were normalized to the TRS-398 value at $R_{50} = 8.3$ cm, as this was the CSnrc point closest to the Sempau et. al. point of normalization. The normalized values from CSnrc are also presented in Fig. 7.5. The statistical uncertainty on the CSnrc values is on the order of 0.06% and the normalization factor is 0.9926.

Figure 7.5 shows that the current overall dose ratio results agree with the previously published results of Sempau et. al. As in the case of their results, if the CSnrc values are normalized to a TRS-398 point for large R_{50} , the calculated values show the same shape as, and coincide with, the TRS-398 line. Furthermore, since the study by Sempau et. al. was conducted entirely at a measurement depth of d_{ref} , the larger discrepancies between the calculations and the standard theory at deeper depths did not affect the comparison. While the normalized CSnrc curve and the TRS-398 curve show the same behaviour as a function of beam quality, the need for a normalization suggests an overall correction of 0.74%, not unity as predicted

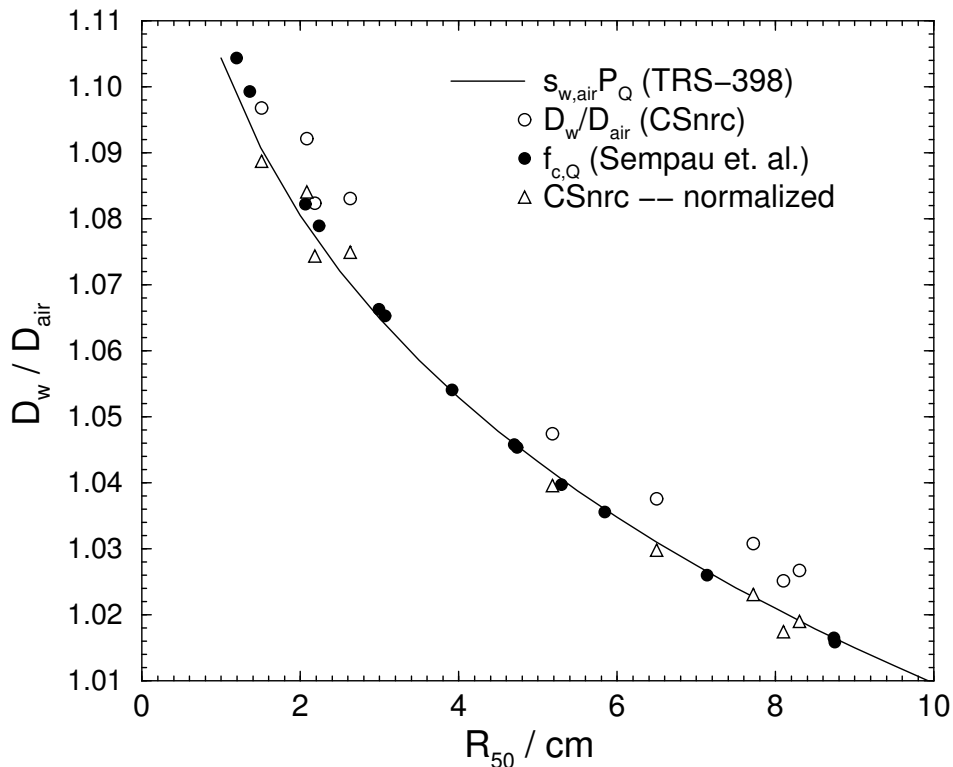


Figure 7.5: The overall correction factor for an NACP chamber in electron beams as a function of beam quality. The CSnrc values show the ratio of dose to water at the point of measurement to dose to air in the NACP chamber. The dose ratios are shown in comparison to the predicted values of the TRS-398 code of practice⁹ and the previously published calculations of Sempau et. al.¹⁰³ The values from Sempau et. al. are taken from digitization of Figure 2 of their paper. The CSnrc values are also shown, normalized to the TRS-398 point at $R_{50} = 8.3$ cm. The statistical uncertainties on the CSnrc values are on the order of 0.06%.

by TRS-398 and TG-51. This correction is smaller than the P_{wall} values presented earlier, suggesting that the replacement correction must behave in a way to cancel some of the wall effects.

7.3 P_{wall} values in photon beams

Parallel-plate chambers are less commonly used in high-energy photon beams than in electron beams, in part due to the lack of information regarding the correction factors for these chambers in photon beams. Figure 7.6 shows the wall correction, P_{wall} as a function of photon beam quality for two parallel-plate chambers: the NACP chamber at left and the Markus chamber at right. The CSnrc values are computed using the photon beam spectra from Sheikh-Bagheri and Rogers.⁴⁷ The CSnrc values are shown in comparison to previously calculated values from Mainegra et. al.⁷³ in a ^{60}Co beam and to the measured values from Wittkämper et. al.¹⁰¹ For purposes of comparison here, the Wittkämper et. al. values were digitized from Figure 1 of their paper and the beam quality specifier, for which they used TPR_{10}^{20} , was converted to $\%dd(10)_x$ using the relationship described by Kalach and Rogers.⁴⁹

The CSnrc values for the ^{60}Co beam agree very well with the values from Mainegra et. al. however, in comparison to the Wittkämper et. al. values, the CSnrc values are higher by up to 1%. It is possible that the discrepancy between the Monte Carlo results and the Wittkämper et. al. results is due to the added uncertainty in their values due to the measurement technique. In order to determine P_{wall} for the parallel-plate chambers, they compared measurements using the parallel-plate chambers to measurements made with a reference cylindrical chamber for which they assumed the correction factors were well-known. Their stated uncertainty of

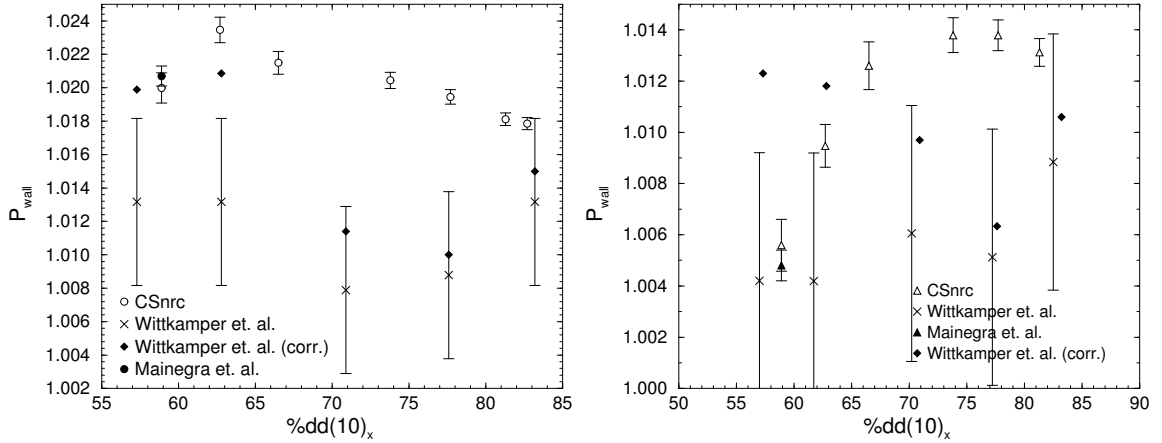


Figure 7.6: P_{wall} values for the NACP and Markus chambers in photon beams calculated using CSnrc. Also shown are the values from Mainegra et. al.⁷³ for a ^{60}Co beam and from Wittkämper et. al. for several photon beam energies. The solid diamonds show the values from Wittkämper et. al., adjusted to use the CSnrc values of P_{wall} for the cylindrical chamber used in their determination of the corrections for the parallel-plate chambers. The values of $\%dd(10)_x$ for the Wittkämper values are converted from TPR_{10}^{20} values plotted in Figure 1 of their paper using the relationship described by Kalach and Rogers.⁴⁹

0.6% does not include uncertainties in the P_{wall} , P_{cel} or P_{fl} values for the cylindrical chamber. Chapters 5 and 6 of this work show that there are potentially significant errors in the standard values for these correction factors. If the CSnrc values of P_{wall} for the reference cylindrical chamber are used, instead of the values from the Almond-Svensson formalism as was used in the Wittkämper et. al. paper, their P_{wall} values change for the Markus and NACP chambers. These corrected P_{wall} values are shown as the solid diamonds in Fig. 7.6. This illustrates the potential effect that the new P_{wall} values can have on previously published experimental results and shows the need for revisiting many of these earlier experiments.

Figure 7.7 presents the CSnrc-calculated values of P_{wall} for the NACP and Markus chambers, in addition to values for the Roos chamber. They are shown in comparison to the Mainegra et. al.⁷³ values for ^{60}Co beams which have been shown to be in reasonable agreement with experiment. The CSnrc values are calculated

7.3. P_{WALL} VALUES IN PHOTON BEAMS

with the chamber placed at a depth of 10 cm in a water phantom. As in the case of electron beams, these chambers show a significant, non-unity wall correction. The CSnrc results are in good agreement with the results from Mainegra et. al.

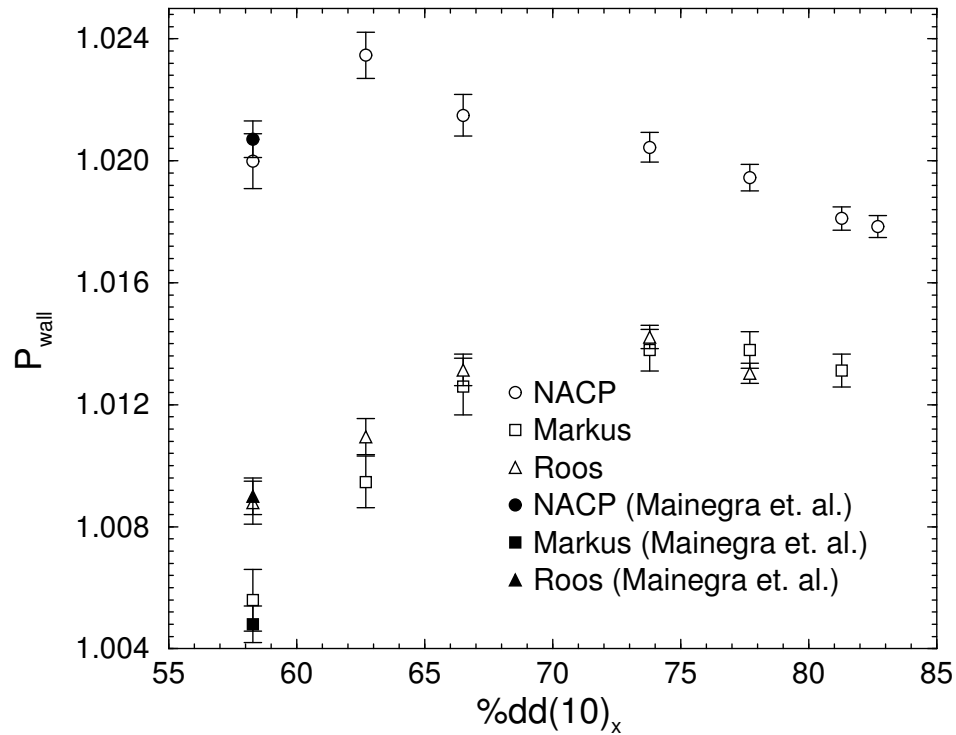


Figure 7.7: P_{wall} values for parallel-plate chambers in photon beams calculated using CSnrc. Also shown are the values from Mainegra et. al.⁷³ for the NACP and Roos chambers in ^{60}Co .

7.4 Summary

This chapter presents an investigation of the wall correction factor, P_{wall} , for parallel-plate ionisation chambers in high-energy photon and electron beams. A set of linear fits to CSnrc-calculated P_{wall} values in electron beams is presented and shows corrections of up to nearly 1.8% for some chambers at the lower energies. This is in sharp

contrast to the assumptions of the dosimetry protocols which use a P_{wall} value of unity in electron beams. This large discrepancy indicates the need for adopting new values of P_{wall} for these chambers in future protocols. The wall correction is also shown to depend on the depth of measurement for electron beams and is used to reconcile differences between dose ratio calculations and the values from standard dosimetry theory. The CSnrc calculations of the dose ratios are compared to a recent Monte Carlo study by Sempau et. al.¹⁰³ and show qualitative agreement with their results. Though they did not quantify their overall correction to standard dosimetry theory, from the CSnrc values, this correction is 0.74%. In photon beams, the CSnrc values of P_{wall} show good agreement with previous Monte Carlo results for ^{60}Co beams⁷³ and show corrections of between 0.5% and 2.3% for the range of energies and the chambers studied here. The CSnrc calculations presented in this chapter show very large P_{wall} correction factors for parallel-plate chambers, in agreement with some earlier experimental work and indicating the need for changes to the presently used values of P_{wall} in the dosimetry protocols.

Chapter 8

The replacement correction, P_{repl}

Chapters 6 and 7 describe calculations using the CSnrc code to determine the wall correction factor P_{wall} for both thimble and parallel-plate chambers. For both types of chambers, it was demonstrated that there are problems with the current values of P_{wall} used by the dosimetry protocols in both photon and electron beams. For thimble chambers, the central electrode correction was discussed in detail in Chapter 5. According to Eq. 2.4, the remaining correction factor to be investigated is the replacement correction, P_{repl} . This chapter presents preliminary investigations of the replacement correction using CSnrc and is included here to introduce preliminary results and to describe the methodology by which this correction may be determined

The replacement correction is not as straightforward to compute as the other corrections using Monte Carlo since there is no simple way to isolate the effects of the cavity from other effects. The schematic depiction of the correction factors shown in Fig. 2.1 indicates that the step going from the bare air cavity within the phantom to the small air cavity satisfying the Spencer-Attix conditions includes both the effects of the replacement correction and the stopping power ratios of water to air.

Using Monte Carlo techniques, it is however possible to infer the value of P_{repl} using the calculations described in preceding chapters. The CSnrc code has been used to calculate P_{cel} , P_{wall} and the dose ratio D_{water}/D_{air} . As described previously, the standard stopping-power ratios can be calculated using the SPRRZnrc code, leaving only P_{repl} to be determined in Eq. 2.4:

$$P_{repl} = \frac{D_w/D_{air}}{\left(\frac{\bar{L}}{\rho}\right)_{air}^{water} P_{wall}}. \quad (8.1)$$

Figure 7.4 from Chapter 7 is reproduced in Fig. 8.1 to illustrate how P_{repl} may be inferred from these calculations. The solid line in Fig. 8.1 shows the dose ratio D_{water}/D_{air} for an NACP chamber in a 6 MeV electron beam. By the Spencer-Attix equation, (Eq. 2.3) this dose ratio should equal the stopping-power ratio of water to air, shown as the dashed line in Fig. 8.1. As pointed out in Chapter 7, the two lines diverge as the depth of measurement is increased. Also shown in Fig. 8.1 are lines showing P_{wall} and the product $\left(\frac{\bar{L}}{\rho}\right)_{air}^{water} P_{wall}$ as a function of the depth of measurement. If the replacement correction in Eq. 2.4 were unity, the dose ratio should be equal to the product $\left(\frac{\bar{L}}{\rho}\right)_{air}^{water} P_{wall}$. In Fig. 8.1, any differences between these two curves may be inferred to be P_{repl} . Using this method to determine P_{repl} for the NACP chamber, the values of P_{repl} are shown as a function of the depth of measurement in Fig. 8.1. Dosimetry protocols assume that P_{repl} is unity for the NACP chamber. Figure 8.1 indicates that at the reference depth, P_{repl} is less than 1% for the NACP chamber in a 6 MeV beam. The behaviour of P_{repl} with depth seen in Fig. 8.1 agrees qualitatively with the calculations of Ma and Nahum¹⁰⁶ who showed that P_{repl} increased with increasing depth for an NACP chamber in monoenergetic electron beams.

For a given chamber, in order to determine P_{repl} at a certain depth, three other calculations are required: the stopping power ratio at depth, P_{wall} and the

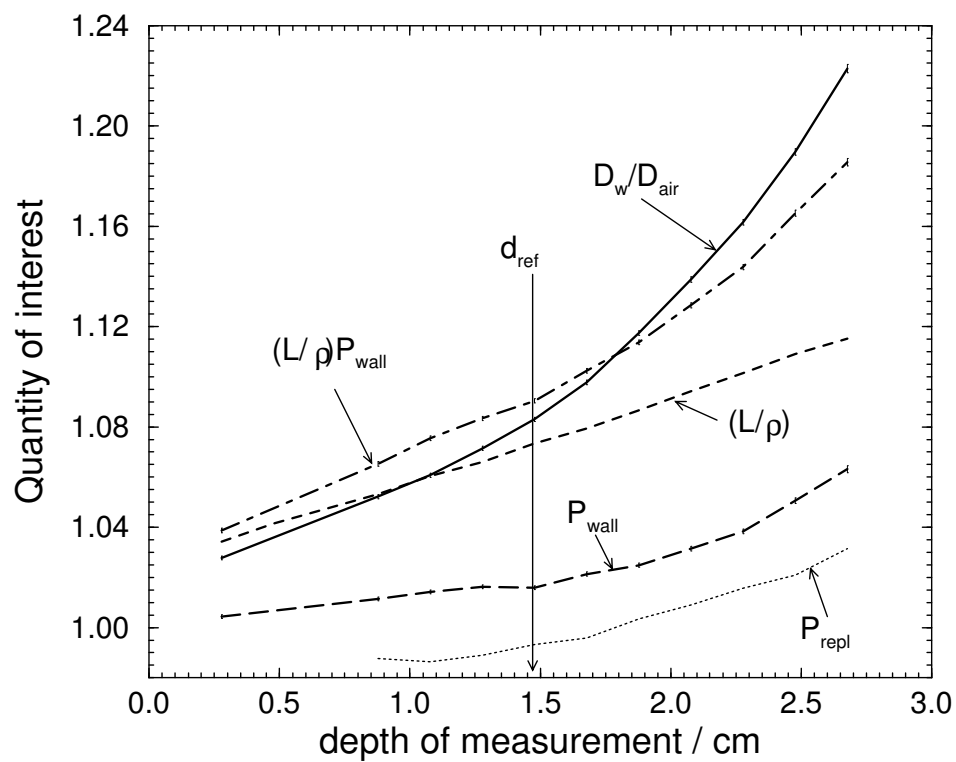


Figure 8.1: Same as Figure 7.4 but includes the replacement correction for the NACP chamber as derived from Eq. 8.1. The calculations are for an NACP chamber in a 6 MeV electron beam.

dose ratio. This is particularly of interest for thimble chambers, where there is more information available regarding the replacement correction and comparisons could be made between the method described above and previously published values.

Chapter 9

Conclusions

This thesis describes an investigation of ion chamber correction factors used in radiation dosimetry using the EGSnrc Monte Carlo code. Accurate knowledge of these correction factors is necessary for maintaining an acceptable degree of accuracy in the dosimetry measurements. Furthermore, these corrections must be known very precisely, as the overall uncertainty on the dosimetry is required to be on the 1-2% level. Current dosimetry protocols often use correction factors based on earlier, and much less precise, Monte Carlo calculations or on assumptions derived from the lack of information available regarding the correction factors.

Chapter 3 describes a new user-code developed for the EGSnrc system. This code, CSnrc, uses a correlated sampling variance reduction technique in order to improve the efficiency of calculations of dose ratios when comparing doses from two similar geometries. CSnrc was developed from the EGSnrc user-code CAVRZnrc and was based upon an earlier correlated sampling code for the EGS4 Monte Carlo system. CSnrc improves upon the correlated sampling algorithm used in the EGS4 version and incorporates the many improvements of the EGSnrc system over the

EGS4 code. CSnrc also includes a rectangular phantom geometry and an option to vary the photon cross-sections by a user-specified amount. CSnrc has been shown to accurately reproduce dose calculations performed using CAVRZnrc. For some highly correlated geometries, CSnrc provides an efficiency gain of over a factor of 60 compared to CAVRZnrc when calculating the dose ratio between geometries. For the central electrode correction factor calculations described in Chapter 5, this efficiency gain is on the order of a factor of 20-30 and for the wall correction factor calculations described in Chapters 6 and 7 the efficiency gain from CSnrc is a factor of 3-4.

Chapter 5 describes CSnrc calculations of the central electrode correction factor, P_{cel} , in high-energy photon and electron beams. This correction factor accounts for the change in chamber response due to the presence of the central electrode. Current protocols use P_{cel} values based upon a previous Monte Carlo study that had poorer statistics and for electron beams, only calculated P_{cel} at a few beam qualities and at several discrete depths in water. The present calculations compute P_{cel} for graphite and aluminum central electrodes for several photon and electron beam qualities and are all computed at the reference depth, as defined by the TG-51 protocol. The statistics on the CSnrc calculations are in the range 0.01-0.03%. For photon beams, the CSnrc results agree with the values currently used by the dosimetry protocols. These show no correction for a 1 mm diameter graphite electrode and P_{cel} varying with beam energy (^{60}Co to 25 MV) from 0.9925 to 0.9965 for a 1 mm aluminum electrode. The CSnrc values of P_{cel} in electron beams show up to a 0.2% deviation from the values used in the dosimetry protocols for the graphite electrode and a 0.1% deviation for the aluminum electrode. CSnrc calculations also show that in photon beams, the value of P_{cel} for a chamber with a graphite electrode is not influenced by the diameter of the electrode. This is not the case for a chamber having

an aluminum electrode, where P_{cel} varies significantly with the electrode diameter. This variation is greatest for a ^{60}Co beam, where P_{cel} changes by over 1% in going from a 0.5 mm diameter electrode to 2 mm. The diameter is also seen to affect P_{cel} in electron beams, where both a graphite and an aluminum electrodes show an increase in P_{cel} of up to 0.3% over the same range of diameters.

The wall correction factor, P_{wall} , for thimble ionization chambers is discussed in Chapter 6. The standard formalism used by the dosimetry protocols uses an empirical formula developed by Almond and Svensson.⁵² This chapter describes a number of experimental results that showed problems with this formalism and shows that the P_{wall} values calculated using CSnrc agree much better with experiment than do the values from the Almond-Svensson formalism. Chapter 6 also presents a set of P_{wall} values at a variety of photon beam energies for a number of thimble chambers and shows that these values differ from the Almond-Svensson values by as much as 0.8%. The wall correction is also presented for the same chambers in electron beams and shows corrections of up to 0.6%, whereas the protocols assume a correction of unity for these beams. CSnrc is also used to compute the sleeve correction factor, P_{sleeve} , which is currently ignored in the dosimetry protocols, and shows that in both photon and electron beams this correction can be as high as 0.3%. The sleeve correction can be generalized for all of the chambers studied here and Chapter 6 presents simple linear equations that can be used to estimate the sleeve correction as a function of beam energy. CSnrc is also used for electron beams to show that P_{wall} varies significantly with the depth of measurement and this effect is seen to be in large part explained by the difference in density between the wall material and the surrounding water phantom. Finally, CSnrc is used to validate the current assumption that the P_{wall} correction is independent of the cavity size although a small dependence on the cavity

radius is seen for chambers having a large P_{wall} correction.

Chapter 7 describes many of the same P_{wall} calculations as in Chapter 6, but for parallel-plate ionization chambers. Due to a lack of information available for these chambers, dosimetry protocols do not permit the use of these chambers in photon beams other than ^{60}Co and assume a value of unity for P_{wall} in electron beams, despite experimental evidence suggesting that this may not be the case. In Chapter 7, a set of P_{wall} values is presented for a variety of parallel-plate chambers in both photon and electron beams. In photon beams, the P_{wall} correction is shown to be between 0.5% and 2.3%, depending on the type of chamber and the beam quality. In electron beams, straight line fits to the CSnrc-calculated P_{wall} values as a function of beam quality show corrections of 1% or greater at the lowest energy studied ($R_{50} = 2.1$ cm). For all of the chambers considered, P_{wall} decreases as a function of R_{50} . The wall correction is also shown to depend on the depth of measurement in electron beams and for a 6 MeV beam shows nearly a 6% change in going from the reference depth, d_{ref} , to a depth of R_{50} . Chapter 7 also presents CSnrc calculations to determine an overall correction factor to the Spencer-Attix theory. The CSnrc results were shown to agree with another, recent Monte Carlo study¹⁰³ that presented this overall correction in a quantitative fashion.

Overall, the study of the correction factors presented in this work provide a complete set of values for use in radiation dosimetry. The changes from the existing dosimetry protocols vary from 0.2% to nearly 2% depending on the situation and the correction factor being considered. In many cases, the differences for a particular chamber at a specific energy would not be of great consequence for clinical measurements, however for precise work, these new values should be used. This is illustrated in several examples in this thesis where the present values of the correction factors

may be used to explain discrepancies between experimental results and the values from the dosimetry protocols. In certain cases, the discrepancies between the new CSnrc values and the values from the protocols may be large enough to influence clinical results, particularly if additive differences exist in multiple correction factors for a given situation. For this reason, future dosimetry protocols should use this new set of correction factors. Furthermore, many earlier experiments may be explained through a re-analysis of their data using the new values of the correction factors.

The logical future step in this investigation would be to investigate the replacement correction factor. This is very likely far more involved than the other corrections considered here and is beyond the scope of this work. Chapter 8 presents a brief introduction to how CSnrc might be used to investigate the replacement correction and presents some very preliminary results.

Bibliography

- [1] S. C. Ellis. The Dissemination of Absorbed Dose Standards by Chemical Dosimetry - Mechanism and Use of the Fricke Dosimeter. *NPL Report Rad Sci 30 (NPL, Teddington)*, 1974.
- [2] J. S. Pruitt, S. R. Domen, and R. Loevinger. The Graphite Calorimeter as a Standard of Absorbed Dose for ^{60}Co Gamma Radiation. *J of Res. of NBS*, 86:495 – 502, 1981.
- [3] C. K. Ross and N. V. Klassen. The development of a Standard Based on Water Calorimetry for the Absorbed Dose to Water. *Proc. of NPL Water Calorimetry Workshop*, 1994.
- [4] H. Palmans and J. Seuntjens. Construction, Correction Factors and Relative Heat Defect of a high purity, 4 °C Water Calorimeter for Absorbed Dose Determinations in High Energy Photon Beams. *Proc. of NPL Water Calorimetry Workshop*, 1994.
- [5] A. Olszanski, N. V. Klassen, C. K. Ross, and K. R. Shortt. The IRS Fricke dosimetry system. Technical Report PIRS–815, NRC, Ottawa, Canada, 2003.

- [6] AAPM TG-21. A protocol for the determination of absorbed dose from high-energy photon and electron beams. *Med. Phys.*, 10:741 – 771, 1983.
- [7] P. R. Almond, P. J. Biggs, B. M. Coursey, W. F. Hanson, M. S. Huq, R. Nath, and D. W. O. Rogers. AAPM's TG-51 Protocol for Clinical Reference Dosimetry of High-Energy Photon and Electron Beams. *Med. Phys.*, 26:1847 – 1870, 1999.
- [8] IAEA. *Absorbed Dose Determination in Photon and Electron Beams; An International Code of Practice*, volume 277 of *Technical Report Series*. IAEA, Vienna, 1987.
- [9] IAEA. *Absorbed Dose Determination in External Beam Radiotherapy: An International Code of Practice for Dosimetry Based on Standards of Absorbed Dose to Water*, volume 398 of *Technical Report Series*. IAEA, Vienna, 2001.
- [10] ICRU. Determination of Absorbed Dose in a Patient Irradiated by Beams of X or Gamma rays in Radiotherapy Procedures. ICRU Report 24, ICRU, Washington D.C., 1976.
- [11] A. Brahme, J. Chavaudra, T. Landberg, E. C. McCullough, F. Nüsslin, J. A. Rawlinson, G. Svensson, and H. Svensson. Accuracy Requirements and Quality Assurance of External Beam Therapy with Photons and Electrons. *Acta Oncologica, Suppl 1*, pages 1 – 76, 1988.
- [12] G. X. Ding, J. E. Cygler, G. G. Zhang, and M. K. Yu. Evaluation of a commercial three-dimensional electron beam treatment planning system. *Med. Phys.*, pages 2571 – 2580, 1999.

- [13] I. Kawrakow. VMC⁺⁺, electron and photon Monte Carlo calculations optimized for Radiation Treatment Planning. In A. Kling, F. Barao, M. Nakagawa, L. Távora, and P. Vaz, editors, *Advanced Monte Carlo for Radiation Physics, Particle Transport Simulation and Applications: Proceedings of the Monte Carlo 2000 Meeting Lisbon*, pages 229 – 236. Springer, Berlin, 2001.
- [14] J. E. Cygler, G. M. Daskalov, G. H. Chan, and G. X. Ding. Evaluation of the first commercial Monte Carlo dose calculation engine for electron beam treatment planning. *Med. Phys.*, 31:142 – 153, 2004.
- [15] SCRAD. Protocol for the Dosimetry of X- and Gamma-Ray Beams with Maximum Energies Between 0.6 and 50 MeV. *Phys. Med. Biol.*, 16:379 – 396, 1971.
- [16] ICRU. Radiation Dosimetry: X-Rays and Gamma-Rays with Maximum Photon Energies Between 0.6 and 50 MeV. ICRU Report 14, ICRU, Washington D.C., 1969.
- [17] S. R. Domen. A sealed water calorimeter for measuring absorbed dose. *J of Res of NIST*, 99:121 – 141, 1994.
- [18] J. P. Seuntjens, C. K. Ross, K. R. Shortt, and D. W. O. Rogers. Absorbed-dose beam quality conversion factors for cylindrical chambers in high-energy photon beams. *Med. Phys.*, 27:2763 – 2779, 2000.
- [19] J. Seuntjens, A. Van der Plaetsen, K. Van Laere, and H. Thierens. Study of correction factors and the relative heat defect of a water calorimetric determination of absorbed dose to water. *Proceedings of the Int. Symp. on Measurement Assurance in Dosimetry, 24-27 May, Vienna, Austria, IAEA SM 330/6*, pages 45 – 59, 1994.

- [20] C. K. Ross and N. V. Klassen. Water calorimetry for radiation dosimetry. *Phys. Med. Biol.*, 41:1 – 29, 1996.
- [21] C. K. Ross, N. V. Klassen, and G. D. Smith. The Effect of Various Dissolved Gases on the Heat Defect of Water. *Med. Phys.*, 11:653 – 658, 1984.
- [22] C. K. Ross, N. V. Klassen, K. R. Shortt, and G. D. Smith. A direct comparison of water calorimetry and Fricke dosimetry. *Phys. Med. Biol.*, 34:23 – 42, 1989.
- [23] M. Boutillon, B. M. Coursey, K. Hohlfeld, B. Owen, and D. W. O. Rogers. Comparison of primary water absorbed dose standards. *IAEA-SM-330/48*, in *Proceedings of Symposium on Measurement Assurance in Dosimetry*, (IAEA, Vienna), pages 95 – 111, 1994.
- [24] K. R. Shortt, C. K. Ross, M. Schneider, K. Hohlfeld, M. Roos, and A.-M. Perroche. A Comparison of Absorbed Dose Standards for High Energy X-rays. *Phys. Med. Biol.*, 38:1937 – 1955, 1993.
- [25] I. Kawrakow. Accurate condensed history Monte Carlo simulation of electron transport. I. EGSnrc, the new EGS4 version. *Med. Phys.*, 27:485 – 498, 2000.
- [26] I. Kawrakow and D. W. O. Rogers. The EGSnrc Code System: Monte Carlo simulation of electron and photon transport. *Technical Report PIRS-701*, National Research Council of Canada, Ottawa, Canada, page (2000).
, see <http://www.irs.inms.nrc.ca/inms/irs/EGSnrc/EGSnrc.html>.
- [27] W. R. Nelson, H. Hirayama, and D. W. O. Rogers. The EGS4 Code System. Report SLAC-265, Stanford Linear Accelerator Center, Stanford, California, 1985.

- [28] I. Kawrakow, E. Mainegra-Hing, and D. W. O. Rogers. EGSnrcMP: the multiplatform environment for EGSnrc. Technical Report PIRS-877, National Research Council of Canada, Ottawa, Canada, 2003.
- [29] M. J. Berger. Monte Carlo Calculation of the penetration and diffusion of fast charged particles. In B. Alder, S. Fernbach, and M. Rotenberg, editors, *Methods in Comput. Phys.*, volume 1, pages 135 – 215. Academic, New York, 1963.
- [30] I. Kawrakow and A. F. Bielajew. On the condensed history technique for electron transport. *Nuclear Instruments and Methods*, 142B:253 – 280, 1998.
- [31] J. Baro, J. Sempau, J. M. Fernandez-Varea, and F. Salvat. PENELOPE: an algorithm for Monte Carlo simulation of the penetration and energy loss of electrons and positrons in matter. *Nucl. Inst. Meth. B*, pages 31 – 46, 1995.
- [32] F. Salvat, J. M. Fernandez-Varea, and J. Sempau. PENELOPE – A Code System for Monte Carlo Simulation of Electron and Photon Transport. Technical report, OECD Nuclear Energy Agency, Issy-les-Moulineaux, France, 2003.
- [33] S. M. Seltzer. Electron-photon Monte Carlo calculations: the ETRAN code. *Int'l J of Appl. Radiation and Isotopes*, 42:917 – 941, 1991.
- [34] J. F. Briesmeister (Editor). MCNP—A general Monte Carlo N-particle transport code. *Los Alamos National Laboratory Report LA-12625-M (Los Alamos, NM)*, 1993.
- [35] S. Agostinelli *et al.* GEANT4 – a simulation toolkit. *Nucl. Inst. Meth. A*, 506:250 – 303, 2003.

- [36] I. Kawrakow. Accurate condensed history Monte Carlo simulation of electron transport. II. Application to ion chamber response simulations. *Med. Phys.*, 27:499 – 513, 2000.
- [37] J. P. Seuntjens, I. Kawrakow, J. Borg, F. Hobeila, and D. W. O. Rogers. Calculated and measured air-kerma response of ionization chambers in low and medium energy photon beams. In J. P. Seuntjens and P. Mobit, editors, *Recent developments in accurate radiation dosimetry, Proc. of an Int'l Workshop*, pages 69 – 84. Medical Physics Publishing, Madison WI, 2002.
- [38] D. W. O. Rogers, I. Kawrakow, J. P. Seuntjens, and B. R. B. Walters. NRC User Codes for EGSnrc. Technical Report PIRS-702, National Research Council of Canada, Ottawa, Canada, 2000.
- [39] G. Marsaglia, A. Zaman, and W. W. Tsang. Toward a universal random number generator. *Statistics and Probability Letters*, 8:35 – 39, 1990.
- [40] G. Marsaglia and A. Zaman. A new class of random number generators. *Annals of Applied Probability*, 1:462 – 480, 1991.
- [41] M. Lüscher. A portable high-quality random number generator for lattice field theory simulations. *Computer Phys. Commun.*, 79:100 – 110, 1994.
- [42] F. James. RANLUX: A Fortran implementation of the high-quality pseudo-random number generator of Lüscher. *Computer Phys. Commun.*, 79:111 – 114, 1994.
- [43] D. W. O. Rogers, B. A. Faddegon, G. X. Ding, C.-M. Ma, J. Wei, and T. R. Mackie. BEAM: A Monte Carlo code to simulate radiotherapy treatment units. *Med. Phys.*, 22:503 – 524, 1995.

- [44] D. W. O. Rogers, B. Walters, and I. Kawrakow. BEAMnrc Users Manual. *NRC Report PIRS 509(a)revI*, 2004.
- [45] G. Mora, A. Maio, and D. W. O. Rogers. Monte Carlo simulation of a typical ^{60}Co therapy source. *Med. Phys.*, 26:2494 – 2502, 1999.
- [46] R. Mohan, C. Chui, and L. Lidofsky. Energy and angular distributions of photons from medical linear accelerators. *Med. Phys.*, 12:592 – 597, 1985.
- [47] D. Sheikh-Bagheri and D. W. O. Rogers. Calculation of nine megavoltage photon beam spectra using the BEAM Monte Carlo code. *Med. Phys.*, 29:391 – 402, 2002.
- [48] G. X. Ding and D. W. O. Rogers. Energy spectra, angular spread, and dose distributions of electron beams from various accelerators used in radiotherapy. *National Research Council of Canada Report PIRS-0439*, page (see <http://www.irs.inms.nrc.ca/inms/irs/papers/PIRS439/pirs439.html>), 1995.
- [49] N. I. Kalach and D. W. O. Rogers. When is an accelerator photon beam “clinic-like” for reference dosimetry purposes. *Med. Phys.*, 30:1546 – 1555, 2003.
- [50] L. V. Spencer and F. H. Attix. A theory of cavity ionization. *Radiat. Res.*, 3:239 – 254, 1955.
- [51] A. E. Nahum. Extension of the Spencer-Attix Cavity Theory to the 3-Media Situation for Electron Beams. in “*Dosimetry in Radiotherapy*”, (IAEA, Vienna) *Vol 1*, pages 87 – 115, 1988.
- [52] P. R. Almond and H. Svensson. Ionization Chamber Dosimetry for Photon and Electron Beams. *Acta Radiol. Ther. Phys. Biol.*, 16:177 – 186, 1977.

- [53] A. Shiragai. A Proposal Concerning the Absorbed Dose Conversion Factor. *Phys. Med. Biol.*, 23:245 – 252, 1978.
- [54] A. Shiragai. Effective Mass Stopping Power Ratio in Photon Dosimetry. *Phys. Med. Biol.*, 24:452 – 454, 1979.
- [55] M. T. Gillin, R. W. Kline, A. Niroomand-Rad, and D. F. Grimm. The effect of thickness of the waterproofing sheath on the calibration of photon and electron beams. *Med. Phys.*, 12:234 – 236, 1985.
- [56] W. F. Hanson and J. A. D Tinoco. Effects of plastic protective caps on the calibration of therapy beams in water. *Med. Phys.*, 12:243 – 248, 1985.
- [57] U. Fano. Note on the Bragg-Gray cavity principle for measuring energy dissipation. *Radiat. Res.*, 1:237 – 240, 1954.
- [58] F. H. Attix. *Introduction to Radiological Physics and Radiation Dosimetry*. Wiley, New York, 1986.
- [59] A. Kosunen and D. W. O. Rogers. Beam Quality Specification for Photon Beam Dosimetry. *Med. Phys.*, 20:1181 – 1188, 1993.
- [60] P. D. LaRiviere. The quality of high-energy X-ray beams. *Br. J. of Radiology*, 62:473 – 481, 1989.
- [61] D. T. Burns, G. X. Ding, and D. W. O. Rogers. R_{50} as a beam quality specifier for selecting stopping-power ratios and reference depths for electron dosimetry. *Med. Phys.*, 23:383 – 388, 1996.
- [62] D. W. O. Rogers. Fundamentals of Dosimetry Based on Absorbed-Dose Standards. In J. R. Palta and T. R. Mackie, editors, *Teletherapy Physics, Present and Future*, pages 319 – 356. AAPM, Washington DC, 1996.

- [63] M. A. Holmes, T. R. Mackie, W. Sohn, P. J. Reckwerdt, T. J. Kinsella, A. F. Bielajew, and D. W. O. Rogers. The application of correlated sampling to the computation of electron beam dose distributions in heterogeneous phantoms using the Monte Carlo method. *Phys. Med. Biol.*, 38:675 – 688, 1993.
- [64] C.-M. Ma and A. E. Nahum. Calculation of absorbed dose ratios using correlated Monte Carlo sampling. *Med. Phys.*, 20:1189 – 1199, 1993.
- [65] A. F. Bielajew. Correction factors for thick-walled ionisation chambers in point-source photon beams. *Phys. Med. Biol.*, 35:501 – 516, 1990.
- [66] H. Hedtjärn, G.A. Carlsson, and J.F. Williamson. Accelerated Monte Carlo based dose calculations for brachytherapy planning using correlated sampling. *Phys. Med. Biol.*, 47:351–376, 2002.
- [67] I. Lux and L. Koblinger. *Monte Carlo particle transport methods: neutron and photon calculations*. CRC Press, New York, 1991.
- [68] L. A. Buckley, I. Kawrakow, and D. W. O. Rogers. CSnrc: Correlated sampling Monte Carlo calculations using EGSnrc. *Med. Phys.*, 31:3425 – 3435, 2004.
- [69] J. Sempau, S.J. Wilderman, and A. F. Bielajew. DPM, a fast, accurate Monte Carlo code optimized for photon and electron radiotherapy treatment planning dose calculations. *Phys. Med. Biol.*, 45:2263 – 2291, 2000.
- [70] J. Sempau, A. Sánchez-Reyes, F. Salvat, H. Oulad ben Tahar, S.B. Jiang, and J.M. Fernández-Varea. Monte Carlo simulation of electron beams from an accelerator head using PENELOPE. *Phys. Med. Biol.*, 46:1163 – 1186, 2001.

- [71] B. R. B. Walters, I. Kawrakow, and D. W. O. Rogers. History by history statistical estimators in the BEAM code system. *Med. Phys.*, 29:2745 – 2752, 2002.
- [72] D. W. O. Rogers and A. F. Bielajew. Wall attenuation and scatter corrections for ion chambers: measurements versus calculations. *Phys. Med. Biol.*, 35:1065 – 1078, 1990.
- [73] E. Mainegra-Hing, I. Kawrakow, and D. W. O. Rogers. Calculations for plane-parallel ion chambers in ^{60}Co beams using the EGSnrc Monte Carlo code. *Med. Phys.*, 30:179 – 189, 2003.
- [74] I. Kawrakow and M. Fippel. Investigation of variance reduction techniques for Monte Carlo photon dose calculation using XVMC. *Phys. Med. Biol.*, 45:2163 – 2184, 2000.
- [75] C. M. Ma and A. E. Nahum. Effect of size and composition of the central electrode on the response of cylindrical ionization chambers in high-energy photon and electron beams. *Phys. Med. Biol.*, 38:267 – 290, 1993.
- [76] A. F. Bielajew and D. W. O. Rogers. Effects of a Møller cross section error in the EGS4 code. *Med. Phys. (abstract)*, 23:1153, 1996.
- [77] J. H. Hubbell. Photon Mass Attenuation and Energy-absorption Coefficients from 1 keV to 20 MeV. *Int. J. Appl. Radiat. Isot.*, 33:1269 – 1290, 1982.
- [78] J. H. Hubbell and S. M. Seltzer. Tables of X-Ray Mass Attenuation Coefficients and Mass Energy-Absorption Coefficients 1 keV to 20 MeV for Elements $Z = 1$ to 92 and 48 Additional Substances of Dosimetric Interest. Technical Report NISTIR 5632, NIST, Gaithersburg, MD 20899, 1995.

- [79] E. Storm and H. I. Israel. Photon cross sections from 1 keV to 100 MeV for elements $Z=1$ to $Z=100$. *Atomic Data and Nuclear Data Tables*, 7:565 – 681, 1970.
- [80] M. J. Berger and J. H. Hubbell. XCOM: Photon Cross Sections on a Personal Computer. Report NBSIR87–3597, NIST, Gaithersburg, MD20899, 1987.
- [81] J. R. Cunningham, M. Woo, D. W. O. Rogers, and A. F. Bielajew. The Dependence of Mass Energy Absorption Coefficient Ratios on Beam Size and Depth in a Phantom. *Med. Phys.*, 13:496 – 502, 1986.
- [82] ICRU. Stopping powers for electrons and positrons. ICRU Report 37, ICRU, Washington D.C., 1984.
- [83] H. Bichsel and T. Hiraoka. Energy loss of 70 MeV protons in elements. *Nucl. Inst. Meth.*, B66:345 – 351, 1992.
- [84] A. E. Nahum, W. H. Henry, and C. K. Ross. Response of carbon and aluminium walled thimble chamber in ^{60}Co and 20 MeV electron beams. *Proc. of VII Int. Conf. on Med. Phys, in Med. and Biol. Engin. and Comp.*, 23:612 – 613, 1985.
- [85] M. S. MacPherson. PhD Thesis: Accurate Measurements of the Collision Stopping Powers for 5 to 30 MeV Electrons. *NRC Report PIRS 626*, 1998.
- [86] M. S. MacPherson, C. K. Ross, and D. W. O. Rogers. Measured electron stopping powers for elemental absorbers. *Med. Phys. (abs)*, 23:797, 1996.
- [87] G. G. Zeng and J. P. McCaffrey. The response of alanine to a 150 keV X-ray beam. *Radiat. Phys. Chem.*, 72:537 – 540, 2005.

- [88] D. W. O. Rogers, G. M Ewart, A. F. Bielajew, and G. van Dyk. Calculation of Electron Contamination in a ^{60}Co Therapy Beam. in *“Proceedings of the IAEA International Symposium on Dosimetry in Radiotherapy” (IAEA, Vienna), Vol 1*, pages 303 – 312, 1988.
- [89] A. Palm and O. Mattsson. Experimental study on the influence of the central electrode in Farmer-type ionization chambers. *Phys. Med. Biol.*, 44:1299 – 1308, 1999.
- [90] R. Nath and R. J. Schulz. Calculated response and wall correction factors for ionization chambers exposed to ^{60}Co gamma-rays. *Med. Phys.*, 8:85 – 93, 1981.
- [91] C.-M. Ma and D. W. O. Rogers. Monte Carlo calculated wall correction factors for plane-parallel chambers in high-energy electron beams. *Proceedings of the 1995 COMP Annual Meeting (Canadian Organization of Medical Physicists, Edmonton, Alberta)*, pages 117 – 118, 1995.
- [92] B. Nilsson, A. Montelius, and P. Andreo. Wall effects in plane-parallel ionization chambers. *Phys. Med. Biol.*, 41:609 – 623, 1996.
- [93] L. Büermann, H. M. Kramer, and I. Csete. Results supporting calculated wall correction factors for cavity chambers. *Phys. Med. Biol.*, 48:3581 – 3594, 2003.
- [94] M. A. Hunt, G. J. Kutcher, and A. Buffa. Electron backscatter correction for parallel-plate chambers. *Med. Phys.*, 15:96 – 103, 1988.
- [95] S. C. Klevenhagen. Implications of electron backscatter for electron dosimetry. *Phys. Med. Biol.*, 36:1013 – 1018, 1991.
- [96] C. K. Ross, K. R. Shortt, D. W. O. Rogers, and F. Delaunay. A Test of TPR_{10}^{20} as a Beam Quality Specifier for High-Energy Photon Beams. *IAEA-SM-330/10*,

- in Proceedings of Symposium on Measurement Assurance in Dosimetry, (IAEA, Vienna), pages 309 – 321, 1994.*
- [97] P. J. Allisy-Roberts, D. T. Burns, K. R. Shortt, and C. K. Ross. Comparison of the air kerma standards of the NRC and the BIPM for ^{60}Co γ rays. *Rapport BIPM-99/12*, 2000.
- [98] C. K. Ross and K. R. Shortt. The effect of waterproofing sleeves on ionization chamber response. *Phys. Med. Biol.*, 37:1403 – 1411, 1992.
- [99] G. D. Lempert, R. Nath, and R. J. Schulz. Fraction of ionization from electrons arising in the wall of an ionization chamber. *Med. Phys.*, 10:1 – 3, 1983.
- [100] D. W. O. Rogers and A. Booth. PROT: A General Purpose Utility for Calculating Quantities related to Dosimetry Protocols. Technical Report PIRS-529(rev, in preparation), NRC Canada, Ottawa, K1A 0R6.
- [101] F. W. Wittkämper, A. H. L. Aalbers, and B. J. Mijnheer. Experimental determination of wall correction factors. Part II: NACP and Markus plane-parallel ionization chambers. *Phys. Med. Biol.*, 37:995 – 1004, 1992.
- [102] A. J. Williams, M. R. McEwen, and A. R. DuSautoy. A calculation of the water to graphite perturbation factors for the NACP type02 ionisation chamber using Monte Carlo techniques. NPL Report CIRM 13, NPL, Teddington, UK, 1998.
- [103] J. Sempau, P. Andreo, J. Aldana, J. Mazurier, and F. Salvat. Electron beam quality correction factors for plane-parallel ionization chambers: Monte Carlo calculations using the PENELOPE system. *Phys. Med. Biol.*, 49:4427 – 4443, 2004.

- [104] G. X. Ding and J. Cygler. Measurement of P_{repl} P_{wall} factors in electron beams and in a ^{60}Co beam for plane-parallel chambers. *Med. Phys.*, 25:1453 – 1457, 1998.
- [105] K. J. Stewart and J. P. Seuntjens. Comparing calibration methods of electron beams using plane-parallel chambers with absorbed-dose to water based protocols. *Med. Phys.*, 29:284 – 289, 2002.
- [106] C.-M. Ma and A. E. Nahum. Plane-parallel chambers in electron beams: Monte Carlo findings on perturbation correction factor. In *“Proceedings of the IAEA International Symposium on measurement assurance in dosimetry” (Vienna: IAEA)*, pages 481 – 493, 1994.